Alma Mater Studiorum · Università di Bologna

Dottorato di ricerca in Geofisica
ciclo XXXIV

Settore Concorsuale: 04/A4 - geofisica

Settore Scientifico Disciplinare: GEO/12 - oceanografia e fisica dell'atmosfera

COASTAL MODELLING STUDIES FOR FORECASTING AND REMEDIATION SOLUTIONS

Presentata da:

Jacopo Alessandri

Supervisore:

Andrea Valentini

Coordinatore dottorato:

Nadia Pinardi

Co-supervisori:

Nadia Pinardi
Ivan Federico

Esame finale anno 2022

Cosa rende magico un luogo?

la visione mirabolante dei suoi colori?

L'intreccio di terra e aria?

Un dettaglio che portiamo nel cuore?

Le storie che ci racconta e quelle che raccontiamo?

Le vite si incrociano in un' armonia di storie, silenzi, viaggi, suoni

e la meraviglia che pervade quegli istanti.

Abstract

The coastal area along the Emilia-Romagna (ER), in the Italian side of the northern Adriatic Sea, is considered to implement an unstructured numerical ocean model with the aim to develop innovative tools for the coastal management and a forecasting system for the storm surge risk reduction.

The Adriatic Sea has been the focus of several studies because of its peculiar dynamics driven by many forcings acting at basin and local scales. The Adriatic circulation is governed by the balance between heat fluxes and freshwater input. At shorter time scales the wind driven circulation becomes a dominant forcing, especially during intense Scirocco and Bora events. Long gravity waves propagate in the Adriatic Sea in the form of tides and seiches. The ER coast is particularly exposed to storm surge events. In particular conditions, winds, tides and seicehs may combine and contribute to the flooding of the coastal area. The global sea level rise expected in the next decades will increase even more the hazard along the ER and Adriatic coast.

Reliable Adriatic and Mediterranean scale numerical ocean models are now available to allow the dynamical downscaling of very high-resolution models in limited coastal areas. In this work the numerical ocean model SHYFEM is implemented in the Goro lagoon (named GOLFEM) and along the ER coast (ShyfER) to test innovative solutions against sea related coastal hazards.

The shallow waters of the Goro lagoon, where large clam farms are located, are threatened by eutrophication in summer due to a strong stratification and to the high nutrient discharge from the Po River, with consequent hypoxic and anoxic conditions and high clam mortality. During late autumn and winter, strong wind events, especially from south-east direction (Scirocco), may cause the flooding of the towns surrounding the

lagoon. GOLFEM is used here to assess these sea related hazards. The dynamics of the Goro lagoon is analysed, highlighting its estuarine circulation due to the balance between the seaward fresher water at the surface and the onshore seawater at the bottom. Two "what-if scenarios" are analysed to assess the dynamical effects of human interventions in the lagoon and help local authorities with the clam farms and lagoon management. The results show that dredging operations in the lagoon can have positive effects in some areas and negative or no effects in different areas and a careful evaluation of the dredging works is necessary. GOLFEM can be a suitable tool for this kind of evaluations.

The assessment of storm surge hazard in the Goro lagoon is carried out through the development of an ensemble storm surge forecasting system with GOLFEM using forcing from different operational meteorological and ocean models. A weighted ensemble mean is made based on the performance of the members during a training period showing slightly improved results compared to the best deterministic forecast. The analysis of the ensemble spread shows that the open boundaries provide most of the uncertainty followed by meteorological and river forcing that have a spread amplitude respectively one and two order of magnitude lower.

The ShyfER domain is used to investigate innovative solutions against storm surge related hazard along the ER coast. The seagrass is assessed as a nature-based solution (NBS) for coastal protection under present and future climate conditions. The results show that the effects of seagrass on the sea level are negligible. However, the bottom currents can be sensibly reduced by the presence of seagrass with positive implications for coastal erosion. The analysis of the future scenario shows comparable results with slight differences due to the changes in the balance between Po River and atmospheric forcing.

Contents

Chapter 1

Introduction

The physical characteristics of the Adriatic Sea are described in order to provide a solid framework for the modelling results shown in the following chapters. Section 1.2 describes the unstructured grid model System of HydrdYnamic Finite Element Modules (SHYFEM) used in this work. Section 1.3 presents the objectives of the thesis.

1.1 The Adriatic Sea

The Adriatic Sea is a semi-enclosed elongated basin in the central Mediterranean Sea, extending for about 800 km in the NNW-SSE direction and is positioned between the Italian peninsula on the western side and the Balkans on the eastern side (Fig. 1.1). It has a heterogeneous coastal morphology, with sandy beaches on the western side and an irregular and rocky coastline on the eastern side. The Adriatic basin can be divided into three distinct regions (Artegiani et al., 1997a,b). The northern part is very shallow and flat with gentle slopes and a maximum depth of about 50 m. The middle Adriatic becomes deeper with an average depth of 140 m and the mid Adriatic pit where a depth of 260 m is reached. The southern part is the deepest with a large depression of over 1200 m. At the Strait of Otranto ($\sim$ 70 km wide) the water is exchanged with the Mediterranean Sea. The Adriatic Sea can be considered as a dilution basin (Raicich, 1996) due to the high freshwater input provided by the Italian and Balkan rivers. The Po River on the NE side and the Buja/Boiana River on the SE side, provide the 40%

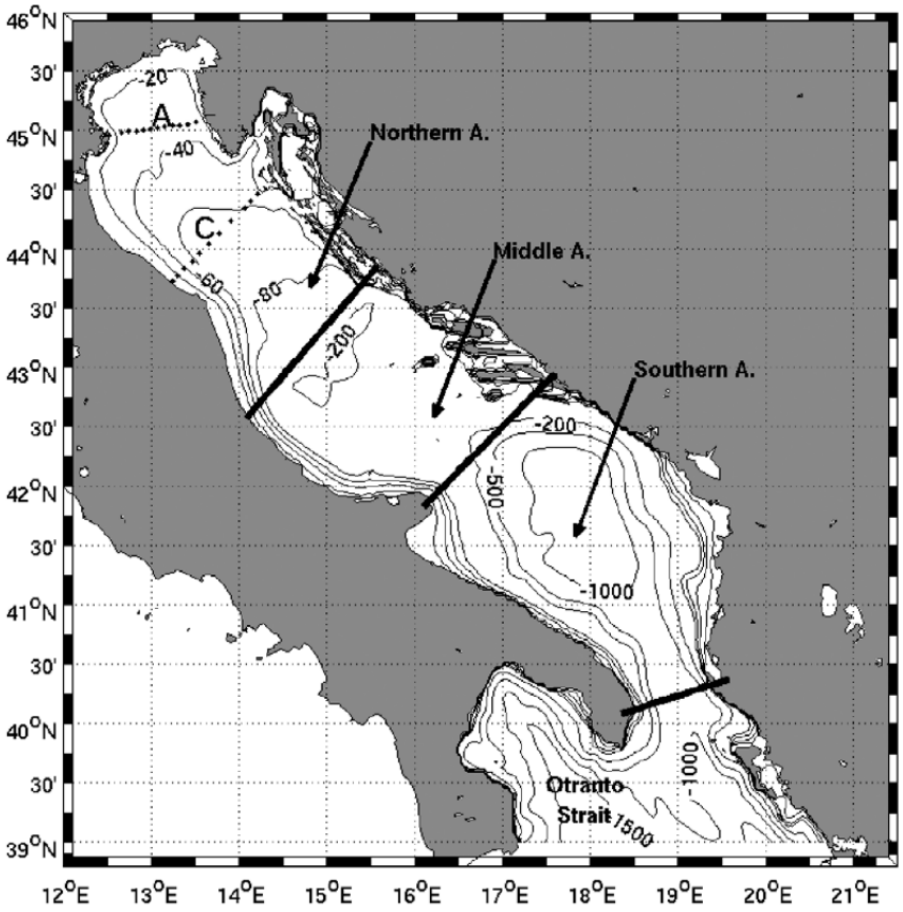

Figure 1.1: Bathymetry of the Adriatic Sea. Source: Oddo et al. (2005).

of the freshwater input of the Adriatic Sea, greatly influencing the general circulation and the salinity and nutrients budget of the basin.

1.1.1 The Heat Budget and Dense Water Formation

The Adriatic basin shows a mean negative value of the climatological heat fluxes budget, with slightly different results by several authors. Chiggiato et al. (2005) found a net heat flux of $-26\,W/m^2$. However, the interannual variability is large. Maggiore et al. (1998) found values from -30 to $5\,W/m^2$. Artegiani et al. (1997a) suggest a value between -19 to $-22\,W/m^2$. Oddo and Guarnieri (2011) found an overall slightly positive mean for the period 2000-2008, with annual mean values ranging from -9 to $19\,W/m^2$. The seasonal variability is large, during autumn and early winter the basin transfers heat to the atmosphere with values of up to 350-400 W/m^2, in particular dur-

ing Bora events, while it gains heat in the spring and summer. The buoyancy budget is determined by the sum of heat and water fluxes that for the Adriatic basin is nearly zero averaged (Pinardi et al., 2006) due to the contrasting contribution of heat loss and high freshwater input. The Adriatic Sea is forced by the heat fluxes to work as an anti-estuarine basin, with deep water formation, while the freshwater fluxes, mainly from Po and other rivers of the northern Adriatic, induce an estuarine circulation, as with a dilution basin.

The Adriatic Sea is known as a deep water formation basin (Pollak, 1951; Artegiani et al., 1997a) due to the strong winter heat loss, amplified also by intense Bora events, leading to the formation of the North Adriatic Dense Water (NAdDW) with σ_t in the range between $29.2 - 29.9\,kg/m^3$, temperature between 8 and $12.8°C$ and salinity in the range $38.1 - 38.5\,psu$ (Artegiani et al., 1997a; Oddo and Guarnieri, 2011). After formation, the NAdDW spreads into the middle and south Adriatic, mixing with adjacent waters, but its signature can also be found at the Otranto strait, contributing to dense water formation in the eastern Mediterranean (Vilibić and Supić, 2005; Malanotte-Rizzoli, 1991).

However, dense water is also locally formed in the southern Adriatic driven by open ocean deep convection that occurs up to a depth of $750\,m$ (Manca et al., 2002; Ovchinnikov et al., 1985). It is formed mainly by the mixing of surface water with Modified Levantine Intermediate Waters (MLIW) with the consequent formation of Southern Adriatic Deep Waters (SADW) with temperature and salinity that are generally in the range $12.7 - 13.5\,°C$ and $38.5 - 38.7\,psu$, respectively and σ_t between 29.25 and $29.29\,kg/m^3$ (Artegiani et al., 1997a; Manca et al., 2002). SADW is recognized as one of the major contribution to the ventilation of deep waters in the eastern Mediterranean (Steinfeldt, 2004; Vilibić and Supić, 2005). The formation of deep water can also occur in the middle Adriatic, when winter convective overturning processes mix cold and fresh NAdDW with warm and salty MLIW, generating the Middle Adriatic Dense Water (MADW) with temperatures between 11 and $12\,°C$ and salinity between 38.1 and $38.62\,psu$. The Adriatic Sea has been the main source of deep dense water in the eastern Mediterranean for many decades, until the Eastern Mediterranean Transient (EMT) in the early 1990s moved the formation of dense water in the Aegean

Sea, replacing almost 20% of the older Eastern Mediterranean Deep Water (EMDW) of Adriatic origin (Roether et al., 1996). However, although the Adriatic contribution to EMDW has been temporarily reduced, deep water formation has never stopped (Sellschopp, 2003).

1.1.2 The General Circulation

The circulation of the Adriatic Sea shows an overall cyclonic pattern (Fig. 1.2) with three distinct cyclonic gyres in the Northern (NAd gyre) Middle (MAd gyre) and Southern areas (SAd gyre) (Artegiani et al., 1997b; Poulain and Raicich, 2001; Zavatarelli, 2002). The three gyres are interconnected through two boundary currents running along the east and west coasts. On the eastern side, a northward current runs from the Otranto strait to the central Adriatic sub-basin, the Eastern Southern Adriatic (E-SAd) current. On the western side, the Western Adriatic Coastal Current (WACC) runs southward from the mouth of the Po River to the Otranto strait. The WACC can be divided into three sub-basin currents: the northern (NAd current), the western middle (W-MAd current) and the western southern (W-SAd current) component.

Both gyres and currents have a strong seasonal variability. The SAd gyre is well defined in all the seasons and in winter, its eastern and western boundaries are strictly connected to the E-SAd current and WACC respectively (Zavatarelli and Pinardi, 2003). Both the SAd and MAd gyres reach their maximum intensity in autumn (Artegiani et al., 1997b). The Nad gyre shows a strong seasonal variability. It intensifies during winter, while in summer it disappears or becomes very weak with occasional reversal of the coastal circulation along the Istrian peninsula, giving rise to the Istrian Coastal Countercurrent (ICC) (Supić et al., 2000; Oddo et al., 2005; Zavatarelli and Pinardi, 2003). In the northern Adriatic Sea the NAd current is predominant in winter extending southward for over 100 km. The intensity of the NAd depends in this area on the balance between heat loss, river discharge and wind stress. Cooler waters tend to weaken the current while the Po River run-off and the wind stress tend to enhance it (Oddo et al., 2005). In the middle Adriatic, the NAd and W-MAd current broaden

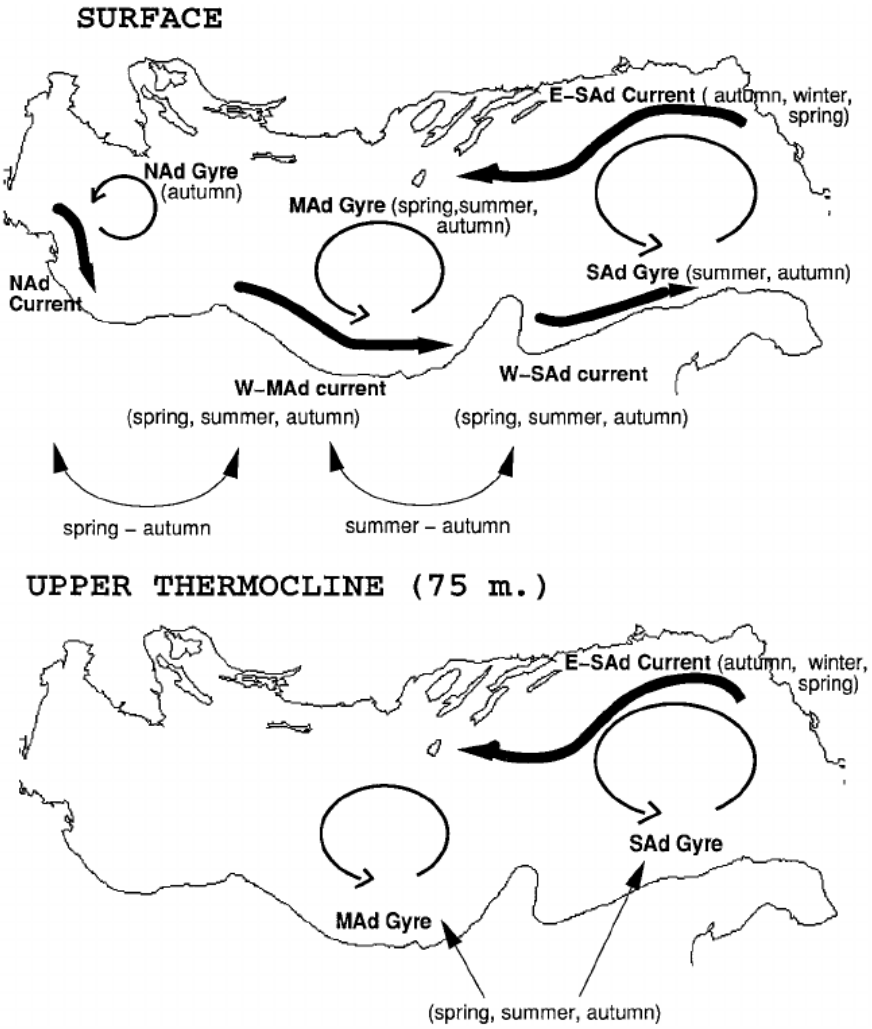

Figure 1.2: The Adriatic Sea baroclinic circulation. Source: Artegiani et al. (1997b).

and meander offshore while rejoin in autumn and winter. The W-MAd and W-SAd currents are well-defined in summer extending as far as the Otranto strait and persisting throughout the autumn, when the E-SAd current is also well-defined, contributing to the advection of MLIW in the basin.

The winter circulation is dominated by the northern (NAd) and southern (SAd) components of the WACC and the presence of a well defined NAd gyre. During spring and summer, the circulation is dominated by the presence of the MAd and SAd gyres and an intensification of W-MAd and W-SAd currents while the E-SAd current weakens. At a lower depth of $75\,m$ the circulation is characterized by the SAd and MAd gyres. However, the latter in winter is very weak and disconnected from the southern Adriatic

circulation (Zavatarelli and Pinardi, 2003).

1.1.3 Principal Wind Regimes

The Adriatic Sea is subjected to two main wind regimes. The Bora wind from the NNE and the Scirocco wind from the SE (Cavaleri et al., 1996). The Bora is a cold and dry katabatic wind that can exceed $20\,m/s$ and last several days. It occurs under different synoptic situations, but always when a cold and dry air mass is located windward of the Dinaric Alps. The Scirocco is a warm and humid wind that is usually less intense than the Bora ($\sim 10 - 15\,m/s$) and usually occurs when a low pressure system is centered in the Tyrrenian Sea. The response of the Adriatic Sea to wind forcing was the focus of several early studies (Rizzoli and Bergamasco, 1983; Orlić et al., 1994; Bergamasco and Gačić, 1996). In standard meteorological conditions, the wind-driven circulation is a secondary forcing compared to the thermohaline one. However, during intense transient events the winds can become dominant in driving the currents. The Bora is more common during the cold season, from November to March. The high spatial variability of the Bora, due to the orographic control (Smith, 1987), is likely responsible for the high frequency perturbations in the general circulation of the Adriatic Sea, especially in the northern sub-basin. The horizontal shear of the Bora represents a vorticity source for the Adriatic currents (Orlić et al., 1994; Bergamasco and Gačić, 1996), inducing a cyclonic circulation in the northernmost part of the basin and an anticyclonic gyres in the negative vorticity area in the lower part of the northern Adriatic. The sea level maxima/minima follow the positive/negative vorticity pattern with the maximum sea level in the western northern basin due to the wind set-up. Conversely, sea level minima are found on the eastern Adriatic coast.

If the Scirocco blows for several days, it generates a high wind set-up and is mainly responsible, with tides, for the frequent flooding events in the northern Adriatic (called "acqua alta" in Venice). The role of the inverse barometer effect may be also relevant. small and deep low pressure systems crossing the northern Adriatic basin may generate a local increase in the sea level along with the other forcings. Moreover, for particularly intense Scirocco events the WACC can be blocked or even reversed (Orlić et al., 1994).

However, the most impacting events occur when Bora in the northern Adriatic basin is associated with Scirocco in the Southern basin amplifying the effect of wind set-up. This condition may be connected to local pressure minimum and the inverse barometer effect can contributes to the sea level increase. The characteristic described above where found for the event of the 12 November 2019, when an exceptional flood event took place in Venice (Ferrarin et al., 2021). A more detailed description of storm surges and sea related hazards along Emilia-Romagna (ER) coast is reported in sections 3.1.1 and 4.1.

1.1.4 Tides in the Adriatic Sea

Tides are the consequences of the interactions between the ocean and celestial bodies (especially the Sun and the Moon) through the gravitational force. This interaction forces a periodic oscillation of the water body in the form of long gravity waves. Tides in the Mediterranean are ususally weak except in the Gulf of Gabes (along Tunisia), where the amplitude of M2 tide alone can reach 51 cm, and in the Adriatic Sea (Tsimplis et al., 1995).

In the Adriatic, the tides can have an amplitude of 1 m which is reached in the northernmost part of the basin (Cushman-Roisin et al., 2001). The significant contribution of tidal dynamics comes basically from seven principal components (Defant, 1961), four semi-diurnal (M2, S2, N2 and K2) and three diurnal (K1, O1, P1). In the Adriatic Sea the tides are of mixed type with the M2 and K1 components having comparable amplitudes that can reach maximum values of about 27 and 20 cm respectively (Polli, 1959; Cushman-Roisin et al., 2001). According to Taylor's theory (Taylor, 1922), tides in the Adriatic Sea behave as a combination of Kelvin and Poincaré waves which are superimposed in a way that the normal velocity vanishes along the sides and on the southern border. The theory allows for the possible existence of amphidromic points, *i.e.*, areas where the tides have zero amplitude, which are observed for M2 and the other semi-diurnal components at the border between northern and middle Adriatic (Fig. 1.3a). No amphidromic points exists for diurnal components that propagate across the basin as topographic waves with the shallow water on their right, *i.e.*, from

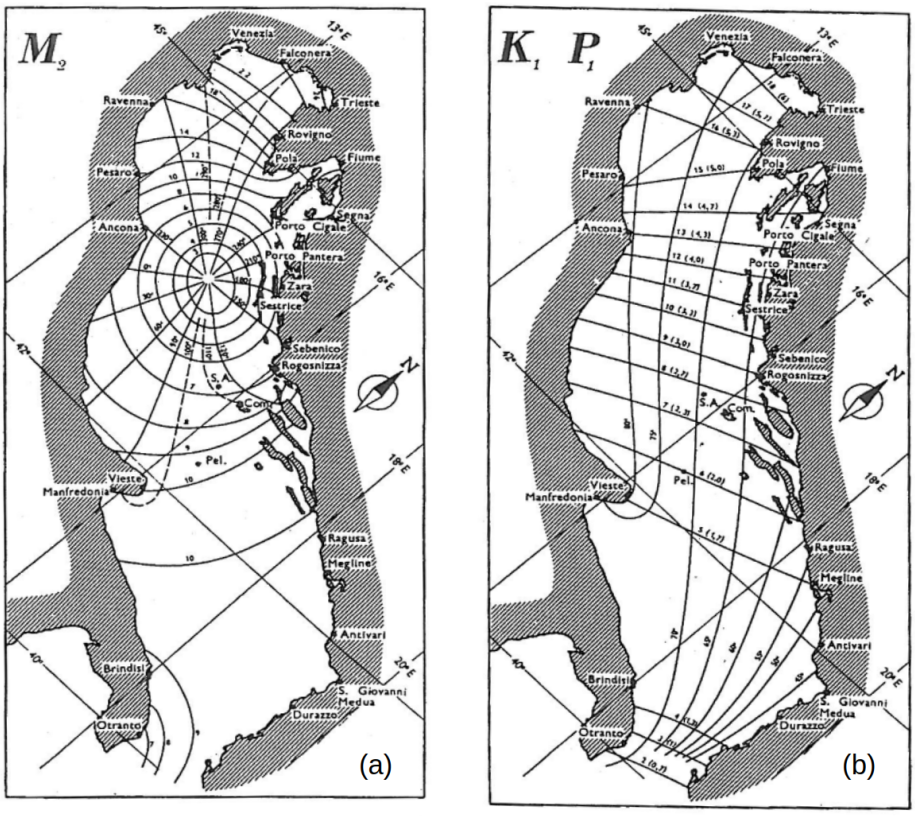

Figure 1.3: Lines of equal tidal amplitude (in cm) and phase for M2 tide (a) and K1 and P1 tides (b) in the Adriatic Sea. All the other semi-diurnal and diurnal tides have a similar distribution as in (a) and (b) respectively. Source: Polli (1959).

Croatian to Italian coast (Malačič et al., 2000).

The Adriatic Sea has two main modes of oscillation (seiches) which are usually triggered by wind forcing. The fundamental mode has a period of about 21.2 hr and can reach a maximum amplitude of 50 cm with a decay time of 3.2 days, while the first mode has a period of 10.7 hr and a much more smaller amplitude. Due to the proximity of the seiches and tides frequencies, resonant phenomenon may occur with an amplification of the tidal amplitude (Medvedev et al., 2020; Vilibić, 2006).

1.2 Shyfem Ocean Model

SHYFEM is a finite element 3D hydrodynamic model developed at Marine Science Institute - National Research Council (ISMAR-CNR) (Umgiesser et al., 2004; Bellafiore and Umgiesser, 2009). A parallel version of the code (Micaletto et al., 2021) is also

used in this work and was developed at the Euro-Mediterranean center for climate change (CMCC) foundation. The model is based on the solution of the primitive equations considering an incompressible fluid and applies hydrostatic and Boussinesq approximations. It runs on an unstructured grid with a staggered Arakawa B-grid type horizontal discretization. Scalar quantities are computed at nodes, while vectors are solved at the center of the element.

1.2.1 Governing Equations

The horizontal momentum equations integrated over a vertical layer l are:

$$\frac{\partial U_l}{\partial t} + u_l\frac{\partial U_l}{\partial x} + v_l\frac{\partial U_l}{\partial y} + \int_{z_l}^{z_{l-1}} w\frac{\partial u}{\partial z}dz - fV_l = -gh_l\frac{\partial \zeta}{\partial x} - \frac{gh_l}{\rho_0}\int_{H_l}^{0}\frac{\partial \rho'}{\partial x}dz - \frac{h_l}{\rho_0}\frac{\partial P_a}{\partial x} + \nabla_h\cdot(A_H\nabla_h U_l) + \int_{z_l}^{z_{l-1}}\frac{\partial \tau_{xz}}{\partial z}dz \quad (1.1)$$

$$\frac{\partial V_l}{\partial t} + u_l\frac{\partial V_l}{\partial x} + v_l\frac{\partial V_l}{\partial y} + \int_{z_l}^{z_{l-1}} w\frac{\partial v}{\partial z}dz + fU_l = -gh_l\frac{\partial \zeta}{\partial y} - \frac{gh_l}{\rho_0}\int_{H_l}^{0}\frac{\partial \rho'}{\partial y}dz - \frac{h_l}{\rho_0}\frac{\partial P_a}{\partial y} + \nabla_h\cdot(A_H\nabla_h V_l) + \int_{z_l}^{z_{l-1}}\frac{\partial \tau_{yz}}{\partial z}dz \quad (1.2)$$

where $\zeta = \zeta(x, y, t)$ is the free surface, $l = 1 \dots N$ is the vertical layer index, starting with $l = 1$ for the surface layer and increasing with depth with $l = N$ being the bottom layer, $z_l = 0 \dots N$ are the layer interfaces with $z_0 = 0$ being the surface and $z_N = N$ for the bottom interface. u_l and v_l are the horizontal velocity, U_l and V_l are the horizontal velocity integrated over the layer l (transport) defined by

$$U_l = \int_{z_l}^{z_{l-1}} u_l\,dz, \quad \text{and} \quad V_l = \int_{z_l}^{z_{l-1}} v_l\,dz \quad (1.3)$$

where h_l is the layer thickness, Pa is the atmospheric pressure at the sea surface, g is the gravitational acceleration, ρ_0 is the reference density of sea water, $\rho = \rho_0 + \rho'$ is the water density with ρ' representing the perturbation of the density from the reference value ρ_0, H_l is the depth of the bottom of layer l, A_H is the horizontal eddy viscosity computed following the Smagorinsky formulation (Smagorinsky, 1963; Blumberg and Mellor, 1987), and w is the layer vertical velocity.

τ_{xz}, τ_{yz} are the turbulent Reynolds stresses at the top and bottom of each layer defined as:

$$\int_{z_l}^{z_{l-1}} \frac{\partial \tau_{xz}}{\partial z} dz = \tau_{xz}^{z_{l-1}} - \tau_{xz}^{z_l} = Av \frac{\partial u_l}{\partial z}, \qquad \int_{z_l}^{z_{l-1}} \frac{\partial \tau_{yz}}{\partial z} dz = \tau_{yz}^{z_{l-1}} - \tau_{yz}^{z_l} = Av \frac{\partial v_l}{\partial z} \quad (1.4)$$

for the first layer, $l = 1$ the stress terms $\tau_{xz}^{z_0}$, $\tau_{yz}^{z_0}$ are defined by the momentum surface boundary condition(Eq. 1.17), while for the last layer $l = N$ the terms $\tau_{xz}^{z_N}$, $\tau_{yz}^{z_N}$ are defined by the bottom boundary condition (Eq. 1.18).

The continuity equation integrated over a vertical layer l is written as:

$$\frac{\partial U_l}{\partial x} + \frac{\partial V_l}{\partial y} = w_{z_l} - w_{z_{l-1}} \quad (1.5)$$

The layer integrated salinity and temperature equations read respectively:

$$\frac{\partial (h_l S_l)}{\partial t} + U_l \frac{\partial S_l}{\partial x} + V_l \frac{\partial S_l}{\partial y} + \int_{z_l}^{z_{l-1}} w \frac{\partial S}{\partial z} dz = \nabla_h \cdot (K_H \nabla_h h_l S_l) + \int_{z_l}^{z_{l-1}} \frac{\partial}{\partial z} \left(K_V \frac{\partial S}{\partial z} \right) dz \quad (1.6)$$

$$\frac{\partial (h_l \theta_l)}{\partial t} + U_l \frac{\partial \theta_l}{\partial x} + V_l \frac{\partial \theta_l}{\partial y} + \int_{z_l}^{z_{l-1}} w \frac{\partial \theta}{\partial z} dz = \nabla_h \cdot (K_H \nabla_h h_l \theta_l) + \int_{z_l}^{z_{l-1}} \frac{\partial}{\partial z} \left(K_V \frac{\partial \theta}{\partial z} \right) dz + \int_{z_l}^{z_{l-1}} \frac{I}{\rho_0 C_p} dz \quad (1.7)$$

where K_H and K_V are the horizontal and vertical turbulent diffusion coefficient, respectively. S_l and θ_l are the salinity and temperature in the layer l. For both Eq. 1.6 and 1.7 in the first layer, $l = 1$ and the last layer, $l = N$ respectively the surface and bottom boundary conditions are defined for the last term on the LHS with vertical velocity boundary condition (Eq. 1.15) and for the second term on the RHS with flux boundary conditions (Eq. 1.21 and 1.20).

The last term in Eq. 1.7, I, is the solar irradiance at depth z, parametrized with a double exponential according to Paulson and Simpson (1977), defined as:

$$\frac{I}{I_0} = R\, e^{-z/\xi_1} + (1 - R)\, e^{-z/\xi_2} \quad (1.8)$$

where I_0 is the irradiance at the surface (W/m^2), ξ_1 and ξ_2 are attenuation lengths for the portion of the surface radiation in the visible spectrum. In this work, I_0 is parametrized with Reed's formula (Reed, 1977).

To complete the set of equations the in-situ density ρ is computed from the salinity, temperature and pressure according to the United Nations Educational, Scientific and Cultural Organization (UNESCO) equation of state (Fofonoff and R.C., 1983):

$$\rho_l(x, y, l, t) = \rho_l(s_l, \theta_l, p_l) \tag{1.9}$$

1.2.2 Turbulence Model

The vertical eddy viscosity, A_V, and diffusivity, K_V are computed trough the definition of a two-equation model using a $k - \varepsilon$ scheme for the closure of the turbulence that is implemented in the General Ocean Turbulence Model (GOTM) (Burchard et al., 1999) and is part of the SHYFEM code.

The eddy viscosity and diffusivity are found by applying the relations of Kolmogorov (1941) and Prandtl (1945) which relate the turbulent coefficients to a velocity and a turbulent length scale:

$$A_V = c_\mu \sqrt{k} l + \nu_v \,, \qquad K_V = c'_\mu \sqrt{k} l + \gamma_v \tag{1.10}$$

where k is the turbulent kinetic energy, l is a turbulent length scale, ν_v and γ_v are respectively the molecular viscosity and diffusivity while c_μ and c'_μ are dimensionless stability functions. In order to find the value for the vertical turbulent coefficients, the GOTM model solves an equation for the turbulent kinetic energy, k and an equation for the turbulence dissipation, ε defined as:

$$\frac{\partial k}{\partial t} + \overrightarrow{U} \cdot \nabla k = \frac{\partial}{\partial z}\left(\frac{A_v}{\sigma_k}\frac{\partial k}{\partial z}\right) + P_s + B - \varepsilon \tag{1.11}$$

$$\frac{\partial \varepsilon}{\partial t} + \overrightarrow{U} \cdot \nabla \varepsilon = \frac{\partial}{\partial z}\left(\frac{A_v}{\sigma_\varepsilon}\frac{\partial \varepsilon}{\partial z}\right) + \frac{\varepsilon}{k}\left(c_{\varepsilon 1} P_s + c_{\varepsilon 3} B - c_{\varepsilon 2}\varepsilon\right) \tag{1.12}$$

where σ_k and σ_ε are the turbulent Schmidt number for k and ε, respectively. P_s is the turbulent production by shear, B is the buoyancy production/destruction term while $c_{\varepsilon 1}$, $c_{\varepsilon 2}$ and $c_{\varepsilon 3}$ are empirical constants.

The classical energy cascade model lead to a relation between k, ε and l expressed by the following:

$$l = \left(c_\mu^0\right)^3 \frac{k^{3/2}}{\varepsilon} \tag{1.13}$$

where c_μ^0 is an empirical constant. Once Eq. 1.11 and 1.12 are numerically solved we can retrieve the turbulence length scale from Eq. 1.13 and compute the vertical eddy viscosity and diffusivity from Eq. 1.10.

1.2.3 Boundary Conditions

Integrating the continuity equation over the water column gives:

$$\frac{\partial \widehat{U}}{\partial x} + \frac{\partial \widehat{V}}{\partial y} = w_B - w_0 \tag{1.14}$$

where $\widehat{U}$ and $\widehat{V}$ are the barotropic velocity components, w_B and w_0 are the vertical velocity at the bottom and at the surface, respectively. These velocities are given by the kinematic initial conditions, which are:

$$w_0 = \frac{Dz}{Dt}\Big|_\zeta + E - P \qquad w_B = 0 \tag{1.15}$$

where E is the evaporation, and P is the precipitation. The free surface equation can now be written as:

$$\frac{\partial \zeta}{\partial t} + \frac{\partial \widehat{U}}{\partial x} + \frac{\partial \widehat{V}}{\partial y} = P - E \tag{1.16}$$

Note that the river run off is not included in the surface boundary condition, but is treated as a lateral open boundary condition.

At the closed boundaries a full slip condition is set. The velocity component normal to the boundary is set to zero, while the tangential velocity is a free parameter. At the open boundary, Dirichlet boundary conditions are set if the flux is entering the domain, otherwise a zero-gradient condition (Neumann boundary condition) is set. A nudging procedure is used for the velocity open boundary condition, with a nudging time of 30 minutes.

The wind stress, applied at the first layer interface, is treated following the MFS bulk formulae approach (Pettenuzzo et al., 2010):

$$\tau_{xz}^{z(0)} = A_V \frac{\partial u}{\partial z}\Big|_{z(0)} = \frac{\rho_a}{\rho_0} C_D |\overrightarrow{\mathbf{u}_\mathbf{w}}| u_w \qquad \tau_{yz}^{z(0)} = A_V \frac{\partial v}{\partial z}\Big|_{z(0)} = \frac{\rho_a}{\rho_0} C_D |\overrightarrow{\mathbf{u}_\mathbf{w}}| v_w \tag{1.17}$$

where ρ_a is the air density, u_w and v_w the wind velocity components at $10\,m$, and C_D is the wind drag coefficient computed with Hellerman and Rosenstein (1983) formulation.

At the bottom, the stress terms are computed following a quadratic formulation as follows:

$$\tau_{xz}^{z(N)} = A_V \frac{\partial u}{\partial z}\Big|_{z(N)} = \frac{C_B}{H_N^2}|\overrightarrow{\mathbf{U_N}}|U_N \qquad \tau_{yz}^{z(N)} = A_V \frac{\partial v}{\partial z}\Big|_{z(N)} = \frac{C_B}{H_N^2}|\overrightarrow{\mathbf{U_N}}|V_N \tag{1.18}$$

where C_B is a bottom drag coefficient defined as:

$$C_B = \left(\frac{0.4}{\log\left(\frac{\lambda_B + 0.5(H+\zeta)}{\lambda_B}\right)} \right)^2 \tag{1.19}$$

where H is the total depth and λ_B is a bottom roughness length expressed in m.
The diffusive flux of temperature at the air-sea interface reads (Pettenuzzo et al., 2010):

$$K_V \frac{\partial \theta}{\partial z}\Big|_{z(0)} = \theta_{l=1}\,(E - P) + \frac{Q_{net}}{\rho_0 C_p} \tag{1.20}$$

where $Q_{net} = Q_S - Q_L - Q_H - Q_E$ is the net downward heat flux with the shortwave radiation flux Q_S , the longwave radiation flux Q_L , the latent heat flux Q_E and the sensible heat flux Q_H . The C_P coefficient is the specific heat of the sea water.
The diffusive flux of salinity at the surface is:

$$K_V \frac{\partial S}{\partial z}\Big|_{z(0)} = S_{l=1}(E - P) \tag{1.21}$$

At the bottom for the tracers the adiabatic boundary conditions (no flux) is applied:

$$K_V \frac{\partial \theta}{\partial z}\Big|_{z(N)} = 0 \qquad K_V \frac{\partial S}{\partial z}\Big|_{z(N)} = 0 \tag{1.22}$$

1.3 Thesis Objectives

More than 600 million people (around 10% of the world's population) live in coastal areas that are less than $10\,m$ above the sea level. The coastal zone, especially in sensible areas of the world, is frequently subjected to events that can threaten human lives and infrastructures in several ways. Areas affected by eutrophication can experience anoxic conditions with consequent economical losses for human activities and degradation of the natural environment. Exceptional storm surge events can lead to the flooding of coastal areas and can intensify coastal erosion processes. Moreover, the sea level rise expected in the next decades will amplify the hazard in coastal areas.

Eutrophication is a common condition during summer in northern Adriatic Sea and along the ER coast, due to the strong column water stability and to the high river run-off that transport high amount of nutrients leading to an uncontrolled algal bloom. Consequent hypoxic and anoxic conditions threaten the coastal areas, especially in lagoons (*e.g.*, The Goro Lagoon) where peculiar ecosystems and important economic activities are located. Regional effects of climate change, such increased salinity, increased temperature and acidification will affect the Adriatic ecosystems in the next decades.

The low-lying area of the northern Adriatic Sea going from Trieste to Rimini is particularly exposed to flooding events due to both natural and human induced subsidence and to a large portion of reclaimed land under the sea level in the Po Valley. When strong NE (Bora) or SE (Scirocco) wind blows, flooding events are like to occur. The expected sea level rise of the next decades will increase even more the risk associated to floods. The sandy beaches of the ER coast are also very exposed to coastal erosion, which occurs when storm surge events are triggered by strong winds. During a storm surge, large waves resuspend sediment in the water column, and the along-shore current transports it along the coast. The decrease of sediment input from the Po River indirectly also contributes to coastal erosion. The sea level rise together with a decreased Po flux expected in the future will increase the risk associated to coastal erosion.

In the last year, the United Nations (UN) proposed the ocean science decade for sustainable development (2021-2030; The Ocean Decade) posing the foundation for promising results in the next years, with a programme, "CoastPredict", co-designed with the Global Ocean Observing System (GOOS) that is completely dedicated to the development of the global coastal area.

The need to find solutions to the increasing coastal hazard joint to the technological progress of the last decades, lead to the development of advanced tools that may be implemented in coastal areas to prevent or reduce the risk for population and human activities due to hazardous events.

Through the implementation of a high resolution numerical unstructured ocean model (SHYFEM), the aim of this thesis is to develop and test innovative solutions for the

management and the protection of the coastal environment, with the focus on the ER coast and lagoons.

The thesis is structured as follows:

1. Chapter 2 is dedicated to the development and implementation of SHYFEM in the Goro Lagoon (named GOLFEM). The dynamic of the lagoon is analysed and the effects of human interventions on the lagoon is studied through the implementation of "what-if" scenarios to help the lagoon management.

2. In Chapter 3 the GOLFEM model is used to develop an ensemble prediction system to forecast the sea level during extreme storm surge events and to analyse the uncertainty relative to each forcing.

3. Chapter 4 presents an implementation of SHYFEM along the ER coast to evaluate the efficiency of seagrass as Nature-Based Solution (NBS) to protect the coastal area from storm surge and coastal erosion in the present and future climate.

4. In Chapter 5 the conclusions are presented with a brief perspectives of future development.

Chapter 2

Dynamics and What-if Scenarios of the Goro Lagoon

This chapter is an overview of a published paper: Maicu, Alessandri, Pinardi, Verri, Umgiesser, Lovo, Turolla, Paccagnella, and Valentini (2021). It provides a detailed description of the Goro Lagoon's dynamics at a previously unattainable resolution. It also demonstrates for the first time the use of a numerical model to conduct what-if scenarios to evaluate the potential effects on clam farming of two proposed human intervention scenarios on the morphology of the connections to the sea.

2.1 The Goro Lagoon

The Po Delta system on the western side of the northern Adriatic Sea is formed by an interconnected system of river branches and lagoons. The Goro Lagoon is the largest of them all, covering an area of $35\,km^2$ and a volume of $51 \times 10^6\,m^3$. It is roughly triangular in shape, with one of its vertex points pointing E-SE. It is bounded by the Po of Goro River branch on the north-eastern side, with which it is also connected at two points. The southern part is separated from the sea by two spits, the Scanno of Goro and the Scanno of Volano.

The exchange with the sea occurs through a $3\,km$ wide and very shallow inlet, where most of the sea water enters from two $5\,m$ deep channels on the western and eastern sides of the inlet, respectively. They were dredged for navigation purposes and both

channels exhibit an accentuated tendency to become occluded, as can be seen from the seaward lower depth on the bathymetry map (Fig. 2.1a), especially the eastern one, due to sediment deposition from the Po River and transported by coastal currents. The shallow central part of the inlet is all that remains of an old spit that occluded the lagoon and was dredged in mid 1991. At the same time a new spit (named Scanno of Goro) grew which, together with the former spit (Fig. 2.1a) occluded a valuable area once dedicated to a clam nursery. It is interesting how the Landsat imagery slideshow

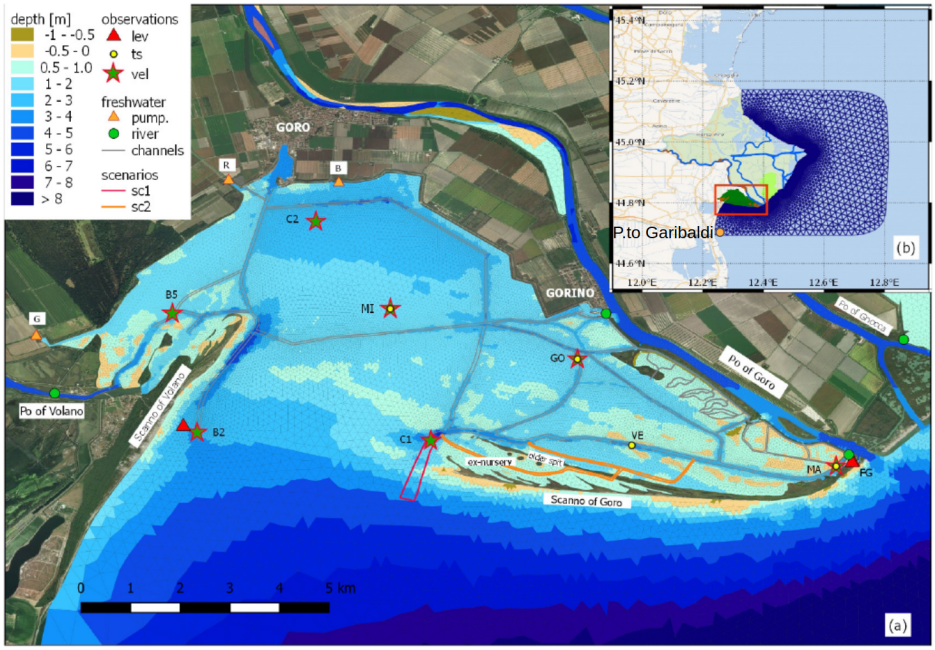

Figure 2.1: (A) Bathymetry of the triangular grid of the Goro Lagoon. In the upper panel (B), the grid extension of the model surrounding the Po River Delta in the Northern Adriatic Sea, where the position of Porto Garibaldi is indicated (orange dot). The pumping stations are: Giralda (G), Romanina (R), and Bonello (B). Station names are: Manufatto (MA), also a river connection (green point), Faro di Goro (FG), Venus (VE), Gorino (GO), nearby the Gorino lock (green point), Mitili (MI), Spiaggina di Goro (C2), western inlet channel (B2), and eastern inlet channel (C1). The Scanno of Goro is the most recent seaward spit that began to grow after 1991. The older spit is still present, but internal to the lagoon. The stars represent the points where the current meters were installed alone, CTDs are indicated with the yellow dots. The background cartography comes from the Bing Aerial dataset for (A) and the Wikimedia dataset for (B). Source: Maicu et al. (2021).

retrievable via Google Earth reliably depicts the spit's overall evolution. The new spit's overall accretion tendency is reported on the EMODnet Geology website[1] and in Simeoni et al. (2007) and Bezzi et al. (2019).

The tidal flats account for most of the lagoon's volume (86.8 %; Table 2.1) with a mean depth of 1.5 m while salt marshes and intertidal flats account for only the 6 % of the total area, which will continue to shrink due to the combined effect of subsidence ($-8\,mm/year$, Tosi et al. (2016)) and sea level rise ($\approx +6\,mm/year$, IPCC AR5 estimation for the Representative Concentration Pathway (RCP) 4.5, IPCC (2013)).

The Goro Lagoon has a large freshwater input on both its eastern and western sides.

morphological zones	Area (km^2)	Perc. total area	Volume (mil. m^3)	depth (m)
Shallow Areas	30.3	86.8 %	44.4	1.47
Channels	2.4	6.8 %	6.0	2.46
Salt Marshes	2.2	6.4 %	0.6	0.28
Goro Lagoon	**34.9**	**100 %**	**51.0**	**1.46**

Table 2.1: Morphological characteristics of the Goro Lagoon.

Along its eastern border, the Po of Goro is connected to the lagoon through the Gorino lock, close to the Gorino harbour. Moving in a south-east direction there is another connection close to the mouth of the Po of Goro, which it is referred to as "Manufatto". These connections are manually opened and closed by local authorities to ensure the most favourable conditions for the lagoon's productivity, but unfortunately, without maintaining any records. These gates are opened during the summer to enhance water renewal and are closed during river floods to maintain acceptable salinity levels in the lagoon and to prevent sediment deposition.

The Goro Lagoon is an important ecological and economic area. It is a protected

[1] https://www.emodnet-geology.eu/data-products/coastal-behavior/

environment (RAMSAR[2], SCI[3] and ZPS[4]), with a high level of biodiversity and part of the spit is designated as a national nature reserve.

The lagoon is well-known throughout the international community for its large clam production, with a total annual output of 14-15 thousand tons, representing 54 % of Italian production and 40 % of European production, involving about 1400 operators and annual sales of 50-70 million euros.

2.1.1 Main Issues, Former Studies and Objectives

Similar to many other transitional environments, the Goro Lagoon is threatened by ecological issues since it receives a high amount of nutrients in the form of nitrates and phosphates from the Po River each year. This leads to dystrophic crisis, particularly in summer, and consequent anoxic conditions in the Goro Lagoon and a high percentage of clam death, resulting in considerable economic losses. The first biogeochemical model study was initially developed by Zaldivar et al. (2003) following the significant dystrophic crisis in 1992. Marinov et al. (2006) carried out another hydrodynamic characterization of the lagoon using a structured grid three dimensional model with a resolution of 150 m coupled with a fate model to investigate the spatial distribution of several pesticides coming from the mainland (Carafa et al., 2006). Finally, Marinov et al. (2008) combined the model with a biogeochemical module.

The lagoon's ecology and dynamics are inextricably linked and interconnected. Human interventions constantly alter the lagoon's morphology which, in turn, alters the lagoon's dynamics and ultimately has an impact on the ecological system. The first study on the dynamical effects of human intervention in the Goro Lagoon was conducted by O'Kane et al. (1992) using a 3D finite difference baroclinic model implemented on a 150 m resolution grid.

The purpose of this high-resolution model is to first study the lagoon's dynamics at a previously unavailable resolution (up to 10 m), capable of resolving the lagoon's nar-

[2] https://www.ramsar.org/

[3] Site of Community Importance

[4] Zona di Protezione Speciale

row connections to the river, and then to evaluate the effects of human interventions through the analysis of "what-if scenarios" using data from oceanographic and meteorological models running operationally at Agency for Prevention, Environment and Energy of Emilia-Romagna (Arpae).

2.2 The Observational Dataset

A large number of measurements collected by the Arpae are available for the Goro Lagoon. These data are useful to design, calibrate and validate the numerical model.

2.2.1 Bathymetry

A well-detailed bathymetry is fundamental for accurately reproducing the circulation, since the bottom boundary layer significantly affects water column dynamics in such a shallow lagoon. Fortunately, the lagoon and the open sea area in front of the spit are frequently subjected to single beam measurements to monitor the lagoon's depth in all the different morphological areas, including the navigable channels and the narrow connections with the Po of Goro River. A very high resolution grid needs a very high resolution bathymetry dataset to achieve the best performance.
Outside the lagoon, data from a coastal multibeam survey conducted by the Arpae in 2012 were used and merged with EMODnet[5] 2018 bathymetry available at 250 m of horizontal resolution. Since the domain also includes rivers, data from cross-section depth observations and from the numerical grid of Maicu et al. (2018) were merged. CNR multibeam data were available for the final section of the Po main branch and were added and merged to the final dataset. All datasets were harmonized and georeferenced to the IGM 1942 altimetric reference.

2.2.2 CTDs, Tide Gauge and Current Meter Data

The permanent observational network within the Goro Lagoon is composed of 4 CTD stations (yellow points in Fig. 2.1) which are installed at a depth 1 m from the bottom

[5] https://www.emodnet-bathymetry.eu/

and measure temperature, salinity and oxygen. Additionally, two tide gauge stations (red triangle in Fig. 2.1) are located in the lagoon, one in front of the Volano spit and one at Manufatto. Regrettably, only tide gauge data for the Manufatto station were available for the 2018 (year of the simulation). Data from Porto Garibaldi station were also used to validate the model.

An *ad-hoc* current meter field campaign was conducted for this project. The instruments (the stars in Fig. 2.1), deployed at a depth of $1\,m$ from the bottom, were positioned at different points of the lagoon. One was permanently installed at Manufatto, while the others were temporary placed in different locations.

2.2.3 Freshwater Input

The transitional environment of the Goro Lagoon is characterized by a strong influence of fresh water inflow on the system's dynamics and thermodynamics. Indeed the Goro Lagoon receives a substantial amount of freshwater, which was not easy to calculate. The connections with the Po of Goro River are on the eastern side. The discharge of the Po of Goro was computed starting from volume flux data available at Pontelagoscuro, $50\,km$ upstream on the main Po branch (Fig. 2.2). This was computed using the discharge rate relationship from Arpae (Arpae, 2018). Using the relationship between the observed discharge for the main branch and the Po of Goro branch (Arpa-Veneto, 2012), a cubic polynomial function was fitted to relate the flow rate at Pontelagoscuro to the flow rate at Po of Goro (Fig. 2.3). This function is valid for main branch flow rates up to $7000\,m^3/s$ and is written as:

$$\%QGoro = 6.46 \times 10^{-11} Q^3 - 1.19 \times 10^{-6} Q^2 + 6.83 \times 10^{-3} Q + 1.21 \tag{2.1}$$

where Q is the flux at Pontelagoscuro and $\%QGoro$ is the percentage of Q forming the flux of the Po of Goro.

On the western side, the freshwater input is supplied primarily by the Po of Volano, an old branch of the Po River whose discharge now consists predominantly of irrigation plants. Indeed, the Po of Volano discharge in Figure 2.2 shows that it does not follow a standard seasonality, as the Po does, but depends on the periods of irrigation that occur mainly during summer, showing a mean flow of $12\,m^3/s$ for 2018, in agreement

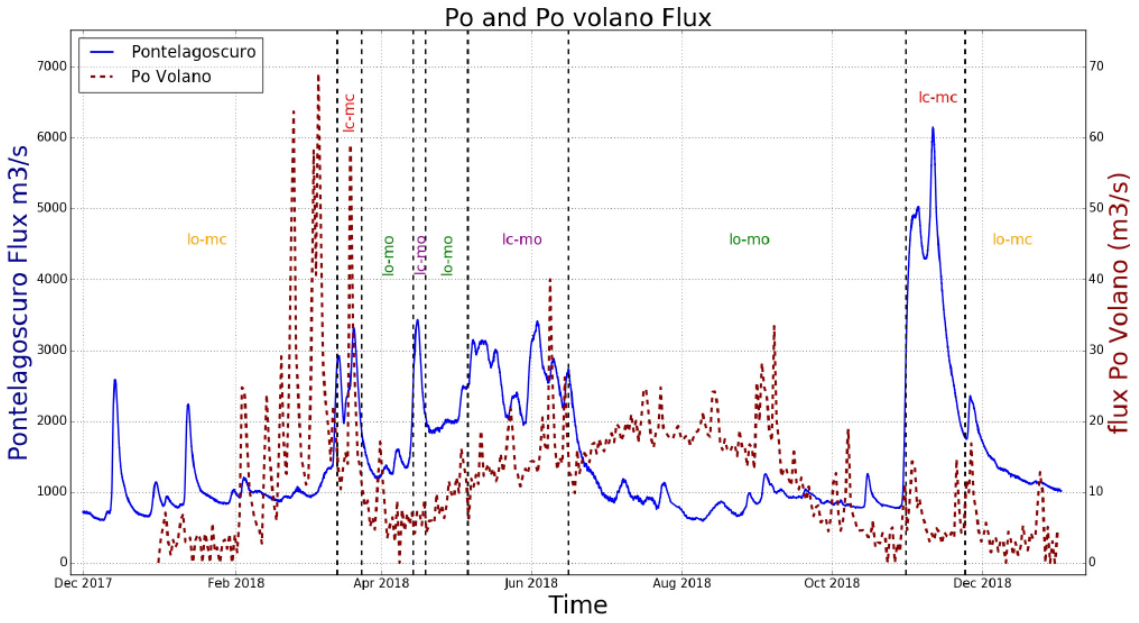

Figure 2.2: The blue line indicates the Po river discharge observed at Pontelagoscuro, 50 km upstream of the river mouth. The dark red dashed line is the Po of Volano discharge composed of several pumping plants. The vertical dashed lines represent the different configurations of the lagoon's connections with the Po of Goro: *lc-mc* Gorino lock and Manufatto closed and vice versa, *lo-mo* both open; *lo-mc* Gorino lock open and Manufatto closed and vice versa for *lc-mo*. Source: Maicu et al. (2021).

with previous studies (Marinov et al., 2008). In addition to the Po of Volano, there are more freshwater inputs on the western side via three pumping plants (the orange triangles in Figure 2.1): Giralda, Romanina and Bonello with a mean flow of 1.6, 5.9 and 0.5 m^3/s respectively, in 2018. Discharge data from these pumping stations and irrigation plants in the Po of Volano were provided by the Consorzio di Bonifica Pianura di Ferrara. These raw data were converted into daily values and used as inputs to the model. The temperature of the Po River and other freshwater inputs were determined using the Arpae report for water quality, where monthly data have been available since 2006. Due to the lack of data for 2018, monthly means were computed from accessible data and used as inputs to the model. Temperature measurements recorded in the Romanina channel were also used for the Giralda and Bonello pumping plants.

Since it is necessary to regulate the flow of freshwater within the lagoon, the Gorino lock is closed during high floods, while the Manufatto, which is more difficult to move,

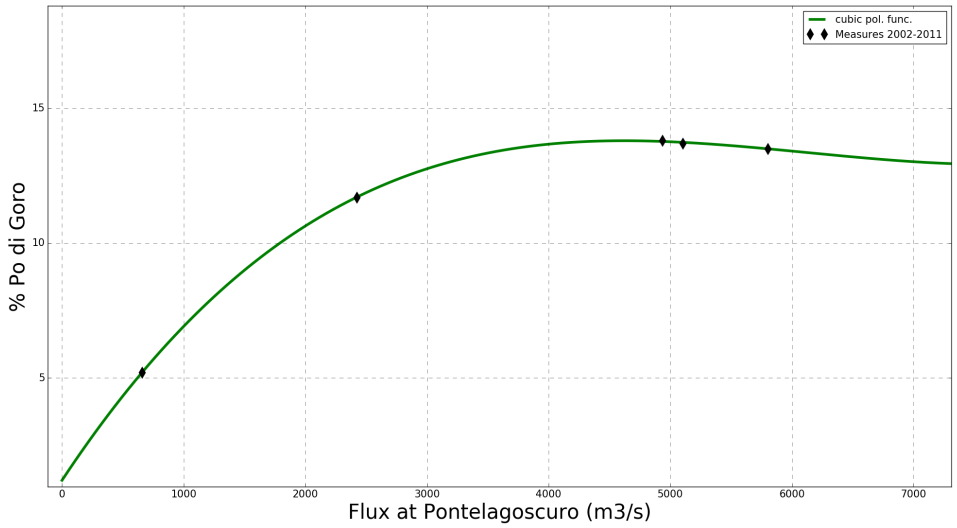

Figure 2.3: Po of Goro's percentage repartition dependence on total flux at Pontelagoscuro. The black diamonds indicate measurements taken from 2002 to 2011. The green line represents the cubic polynomial function fit to the data (Eq. 2.1).

is only partially closed during fixed periods, typically between November and March. There is no automated system in place to regulate these closures. The local authorities directly control these operations and, unfortunately, these are not recorded in a register. This was challenging from a modelling point of view, since these maneuvers deeply influence the lagoon's salinity and dynamics and cannot be simply modeled while the simulation is running. Without any other data available, we defined a threshold water level of $+2.0\,m$ m.s.l. measured in Ariano Polesine on the Po of Goro branch in order to detect river floods and the Gorino lock and Manufatto closure periods (Fig. 2.2).

2.3 Model Design and Implementation

The Goro Lagoon Finite Element Model (GOLFEM) implementation is based on the SHYFEM model, which was discussed in detail in section 1.2. The domain was designed to take advantage of the strengths and flexibility of the unstructured grid approach to describe even the most complex geometries. Due to the lack of a detailed coastline for the Goro Lagoon, it was created using QGIS[6], an open source GIS soft-

[6]https://www.qgis.org/

ware, by using a recent orthophoto (taken in 2017) and creating a new shapefile of the coastline.

The unstructured triangular mesh (Fig. 2.1) was then generated with the GMSH[7] software. The numerical grid's variable resolution reaches its finest size at the coastline and especially within the lagoon with a resolution of $10\,m$ at the Gorino lock connecting the Po of Goro with the lagoon. The requirement for such a high resolution is also explained by all the lagoon's small and narrow channels dredged for navigation purposes. They play a key role in the circulation and must be modeled adequately. The offshore resolution is $2.2\,km$, which corresponds to the resolution of the structured parent model providing lateral open boundary conditions. The whole domain also encompasses most of the Po River branches. The direct modelling of the Po was necessary due to the Po's significant influence on the area's salt and mass balance (Ludwig et al., 2009). The Po River representation made it possible to directly model the saltwater intrusion, an important feature of estuarine dynamics and a potential threat to freshwater resources in a future climate (Bellafiore et al., 2021).

The vertical grid is composed of 17 layers in zeta coordinates, with a partial step approach to better describe the bathymetry. The layers are $1\,m$ thick up to a depth of $10\,m$ and the thickness progressively increases with a depth of up to about $7\,m$ in the last layer. Horizontal diffusion is treated by means of the Smagorinsky formulation (Smagorinsky, 1963). A $k-\varepsilon$ model is used for the treatment of the vertical turbulence (see section 1.2 for more details).

Four different grid settings were arranged due to the human operations of opening and closing the connection with the Po of Goro. We define *lo-mo*, when both Gorino lock and Manufatto are open; *lc-mo*, when the Gorino lock is closed and the Manufatto is open; *lo-mc*, when Gorino lock is open and the Manufatto is closed; and *lc-mc* when both are closed. The different configuration periods are indicated in Figure 2.2.

[7] https://gmsh.info/

2.3.1 Surface and Lateral Boundary Conditions

Physical processes in the ocean occur at various time and spatial scales. The unstructured grid approach makes it possible to simultaneously resolve large and small scale features of the circulation, while accounting for feedback and mutual exchanged effects. GOLFEM reaches a very high resolution at the coast and within the lagoon, while the resolution decreases offshore. The model grid reaches an offshore extension of about $20\,km$, so boundary conditions have fundamental importance for the domain and lagoon's internal dynamics as well as for surface meteorological forcing.

2.3.1.1 Boundary Conditions

Open Boundary Conditions (OBC) must be specified at the domain's border. These are determined by means of the AdriaROMS model analysis (Chiggiato and Oddo, 2008; Russo et al., 2013). AdriaROMS is the Adriatic Sea model, which has been operational at the Hydro Meteo Climate Service of Arpae (Arpae-SIMC) since 2005 (it will be substituted by Adriac). The model has a curvilinear horizontal grid with a resolution ranging from $2\,km$ in the north Adriatic to $10\,km$ in the south Adriatic and a vertical structure of 20 terrain-following levels. It is forced by the COSMO-5M meteorological model (COSMO-newsletter, 2004) at the surface, whereas at the open boundary, at the strait of Otranto, it takes values of the sea level, temperature, salinity and velocity field from the Copernicus Mediterranean model MED-MFS (Clementi et al., 2017). The downscaling approach is schematically represented in Figure 2.4.

Tides, a fundamental forcing in the northern Adriatic Sea, are added to the MED-MFS sea level at the strait of Otranto border and used as boundary conditions for AdriaROMS. Unfortunately, only four tidal components are used (S2, M2, O1, and K1)in the operational chain of AdriaROMS, leading to errors and an underestimation of the sea level. Even if the principal tidal components in the Adriatic Sea are the lunar semi-diurnal M2 and the solar diurnal K1 (Polli, 1959), the best way to represent the tidal signal is by using seven or eight components (M2, S2, K2, N2, K1, O1, P1, and Q1). Moreover, during our analysis, AdriaROMS showed perceptible discrepancies between modeled and observed sea levels on different occasions due to a wrong

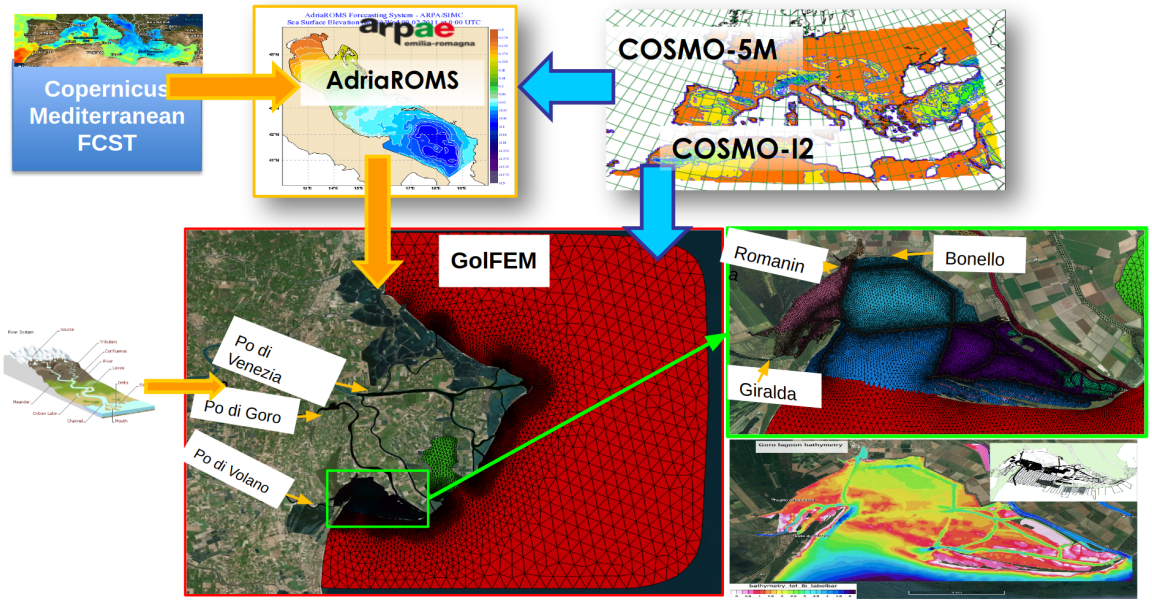

Figure 2.4: A schematic representation of the downscaling modelling chain for GOLFEM simulations. Details of the lagoon grid and bathymetry are also shown at the bottom right of the figure.

tidal signal, probably caused by problems in the transmission of the tides along the domain. The interaction of tides with the bathymetry may generate internal waves that dissipate some of the tidal energy. The difficulties in the representation of the complex Croatian coastline and bathymetry in the AdriaROMS model may lead to a bad representation of tide-bathymetry interaction and eventually to a wrong tidal signal. In order to provide GOLFEM with a better tidal signal, we removed tides from the AdriaROMS' sea level in the location of open boundary nodes using a "detiding" procedure, the Doodson filter (Doodson, 1928), consisting of a 39 hourly window filter obtained by applying a low-pass filter. The Doodson "$X0$" filter reads:

$$y(t) = \frac{1}{30}\left\{w_0 \cdot x(0) + \sum_{m=1}^{m=19} w_m \cdot [x(t+m) + x(t-m)]\right\} \tag{2.2}$$

where $x(t)$ is the input hourly sea level at time t, m is the time index needed to make the time window, $y(t)$ is the filtered output and w_m are the weights defined as:

$$w_m = \begin{cases} 0 & for\ m = 0, 5, 8, 10, 13, 15, 16, 18 \\ 1 & for\ m = 2, 3, 6, 7, 11, 12, 14, 17, 19 \\ 2 & for\ m = 1, 4, 9 \end{cases} \tag{2.3}$$

Astronomical tides are then computed in the position of each node of the open boundary using eight tidal components from the Oregon State University (OSU) barotropic TPXO model with a resolution of 1/30° (Egbert and Erofeeva, 2002) and then added to the detided AdriaRoms sea level.

The improved hourly sea level, temperature and salinity are then provided to GOLFEM. The velocity field is also provided as a boundary condition every hour from the AdriaROMS model with a nudging time of 30 min. The river discharge is treated as an open boundary condition where transport and temperature are given by measurements (Section 2.2.3) and salinity is assumed to be zero. Po River discharge data are collected every 30 min whereas the Po of Volano and the pumping plants have daily values computed and provided to GOLFEM.

2.3.1.2 Surface Forcing

Surface meteorological forcing is provided by the COSMO-I2 model (Steppeler et al., 2003), the operational model at ARPAE with a horizontal resolution of 2.8 km. The fields that are provided to GOLFEM are wind components at 10 m, air temperature at 2 m, dewpoint temperature at 2 m, mean sea level pressure, total cloud cover and precipitation. These variables are necessary to compute the fluxes at the air-sea interface using the MED-MFS Bulk formulae (Pettenuzzo et al., 2010, see Section 1.2.3).

Due to the presence of very turbid water the description of solar radiation absorption is done according to type 9 water from Jerlov (1976). Since no values for the parameters were given in Paulson and Simpson (1977) a double exponential function was fitted to the irradiance value ratios observed by Jerlov (1976) for water type 9. In this case the parameters ξ_1, ξ_2 and R (see Eq. 1.8 in Section 1.2) have the values of 0.325 m, 1.505 m and 0.72, respectively.

2.3.2 Model Calibration and Validation

In order to have a reliable model, GOLFEM was calibrated and tuned comparing the output with the observations that were collected in 2018 and then validated for the entire year.

2.3.2.1 Calibration

We first chose a calibration period of 3 months, from 1 February 2018 to 1 May 2018. The circulation of a shallow basin, such as the Goro Lagoon, is strongly affected by the interaction with the bathymetry through the friction that the bottom exerts on the flow. Hence, the first sensitivity experiments were focused on estimating the best value of the roughness length λ_B, a free parameter affecting the bottom friction term of the equations of motion (see Eq. 1.18 and 1.19). Different values of λ_B with values ranging from 0.005 to $0.08\,m$, were assigned to each of the domain's morphological areas and rivers. Eight different simulations (numbered S1 to S8) were carried out using different λ_B values.

The Pearson correlation coefficient R was computed for each simulation. This is defined as:

$$R = \frac{\frac{1}{N}\sum_{i=1}^{N}\left(\phi_m^i - \overline{\phi_m^i}\right)\left(\phi_o^i - \overline{\phi_o^i}\right)}{\phi_{\sigma m}\phi_{\sigma o}} \tag{2.4}$$

where ϕ_m^i and ϕ_o^i are the model's output and observations respectively, $i = 1, 2, 3 \ldots N$ is the number of observations and $\phi_{\sigma m}$ and $\phi_{\sigma o}$ are the standard deviations of the model's output and observations. The other statistical indices used are BIAS, Root Mean Square Error (RMSE) and Mean Absolute Error (MAE) defined as:

$$BIAS = \frac{1}{N}\sum_{i=1}^{N}\left(\phi_m^i - \phi_o^i\right) \tag{2.5}$$

$$RMSE = \sqrt{\frac{1}{N}\sum_{i=1}^{N}\left(\phi_m^i - \phi_o^i\right)^2} \tag{2.6}$$

$$MAE = \frac{1}{N}\sum_{i=1}^{N}\left|\phi_m^i - \phi_o^i\right| \tag{2.7}$$

The MAE index was used solely in validation phase. The S7 simulation showed equilibrated indices and had the best behaviour at the Manufatto. Therefore, this setting's

roughness length parameters were chosen for the final model setting.

The second set of sensitivity simulations were based on the tracer diffusion coeffi-

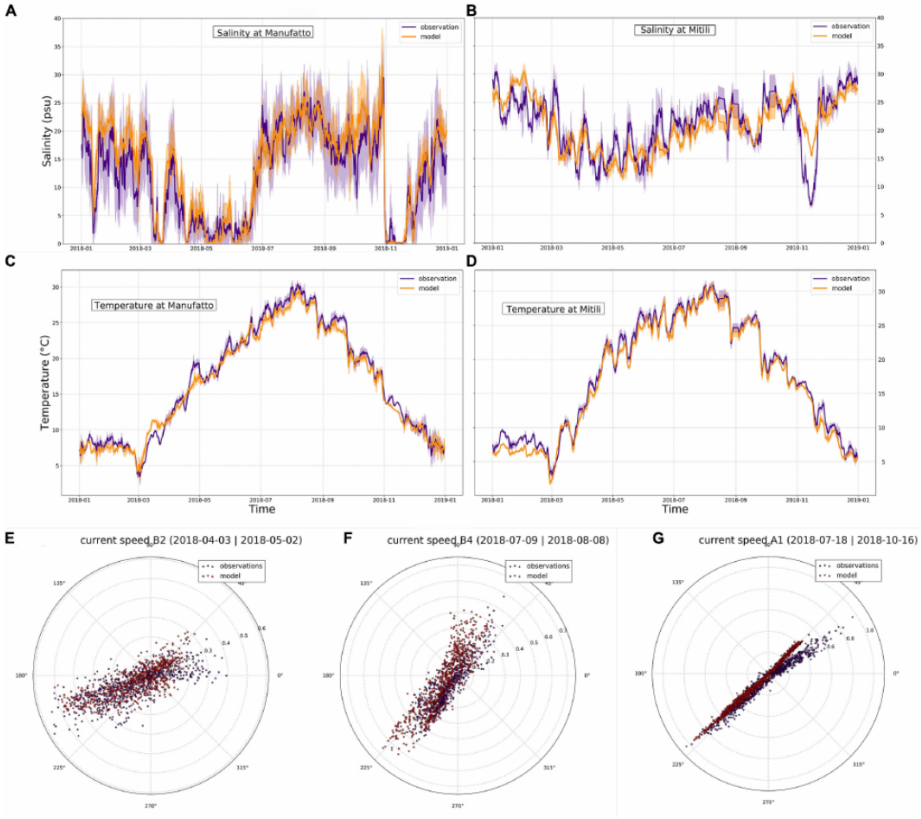

Figure 2.5: Comparison of observed and calculated salinities and temperatures at the Manufatto (MA) (A,C) and Mitili (MI) (B,D) stations. The solid lines and shaded areas are respectively the 24 hour running mean and standard deviation. In panels E,F and G, the comparisons of the polar plots of calculated and observed water velocity are shown for the western inlet channel (B2), the eastern inlet channel (B4) and Manufatto (MI or A1). Source: Maicu et al. (2021).

cient K_h. Values of 0.2, 0.02, 0 and $1\,m^2/s$ were tested respectively for the sensitivity experiments TS1, TS2, TS3 and TS4. The model output was compared with CTD temperature and salinity observations at the four stations of Manufatto, Mitili, Venus and Gorino (Fig. 2.1), and statistical indices were computed. Since the influence of K_h on the comparisons was very low, the default value for K_h, equal to $0.2\,m^2/s$ was used (model set-up, Maicu et al., 2018).

2.3.2.2 Validation

After the calibration phase, GOLFEM was validated over a 1-year simulation from 1 January 2018 to 1 January 2019. One month of spin-up time was considered (December 2017). Figure 2.5 shows the 2018 comparison of salinity and temperatures for the Manufatto and Mitili stations, and current velocity comparison for the western inlet channel (B2), the eastern inlet (B4) and for Manufatto (MA or A1).

	Salinity				Temperature			sea level		
Station	**R**	**BIAS** (psu)	**RMSE** (psu)	**MAE** (psu)	**BIAS** (°C)	**RMSE** (°C)	**MAE** (°C)	**R**	**RMSE** (m)	**MAE** (m)
Manufatto	0.83	1.62	5.55	4.2	-0.46	1.17	0.94	-	-	-
Mitili	0.74	-0.11	3.69	2.87	-0.79	1.14	0.93	-	-	-
Venus	0.57	-1.2	6.5	5.08	-1.08	1.58	1.28	-	-	-
Gorino	0.63	0.64	4.76	3.6	-0.97	1.34	1.1	-	-	-
Faro Goro	-	-	-	-	-	-	-	0.86	0.12	0.09
P.to Garibaldi	-	-	-	-	-	-	-	0.87	0.12	0.1
Ariano P.ne	-	-	-	-	-	-	-	0.98	0.13	0.09

Table 2.2: Statistical scores for temperature, salinity and water level stations.

In the winter months of 2018, the water temperature at the two stations ranged between 5 and 10°C with the lowest values of 2°C, while August values continuously exceeded 30°C, with peaks reaching 32°C. The R correlation for temperature was not computed because the strong seasonal signal would mask an eventual modelling error giving rise to an unrealistically high correlation value. Table 2.2 depicts the BIAS, RMSE and MAE for the four stations, with average values of -0.8, 1.3 and 1.0°C, respectively. Since river temperature inputs are monthly means derived from several years of observed data, deviations from this mean of the real temperature can lead to model temperature deviations. Moreover, the temperature used for the Po of Goro River is the one that is actually taken on the main branch and significant differences may exist. Additionally, only one of the three pumping plants discharging into the lagoon has a temperature measurement (Romanina). Therefore, the same temperature was assumed for the other plants. Temperature errors from boundary conditions could

also have an impact.

The average salinity scores are 0.7, 0.2, 5.1 and 3.9 psu for R, BIAS, RMSE and MAE respectively. There is a high variability in the salinity values due to the high variability in the river run-off. The high RMSE and MAE are influenced by different aspects. The unknown maneuvers at the connections with the Po of Goro introduce a first-order uncertainty in salinity and too strong salinity gradients could not always be adequately reproduced. However, the general salinity structure is well reproduced by the model (Figure 2.5A,B) even though big departures may occur, especially during extreme events (*e.g.*, see November 2018 in Figure 2.5B) with very high discharge rates.

The modelled sea levels show similar scores (Table 2.2) and are in good agreement with observations at three tide gauges, although a better detiding procedure on the input data (such as the one used in Chapter 3) could further improve the comparison. Current velocity was compared at three stations; the western inlet channel (B2), the eastern inlet (C1) and Manufatto. These stations show a BIAS and RMSE for the current intensity of -0.01 and 0.12 m/s for B2, 0.03 and 0.13 m/s for C1 and -0.11 and 0.28 m/s for Manufatto, respectively. The polar plots in Figures 2.5E-G compare the directions of measured and modelled currents at stations B2, C1 and Manufatto, respectively. There is generally good agreement with regard of the flow direction, which is mainly E-NE/W-SW for B2 and NE/SE for C1.

2.4 Results

The Goro Lagoon's circulation and thermohaline characteristics are discussed in this section, with an emphasis on their relationship to the tidal, meteorological and hydrological forcing. These findings are the results of a combination of two techniques. First, the downscaling model propagates the sea level signal (including the large-scale meteorological surge) through the shelf into the lagoon and fully resolves the coastal mixing processes occurring outside the lagoon in this multiple-mouthed delta. Second, the lagoon's high-resolution modelling allows to resolve hydrodynamics caused by several forcings in such a complex environment with multiple connections to other

water bodies. The results are based on three main experiments, CNT, SC1 and SC2 shown in Table 2.3 as well as two shorter simulations, FWI and NOTIDE to evaluate freshwater and tidal influence.

Simulations	Period Simulated	Features
CNT	S: Jan 1, 2018 E: Dec 31, 2018	Actual conditions
FWI	S: Oct 31, 2018 E: Nov 24, 2018	Gorino Lock and Manufatto open
NOTIDE	S: May 6, 2018 E: June 6 2018	No tidal forcing
SC1	S: Jan 1, 2018 E: Dec 31, 2018	Secondary channel drag ($4\,m$ depth, $100\,m$ wide)
SC2	S: Jan 1, 2018 E: Dec 31, 2018	Channels in ex-nursery area ($3\,m$ depth, $40\,m$ wide)

Table 2.3: Final table of experiments.

Sections 2.4.1, 2.4.2 and 2.4.3 refer to the CNT experiment, while also taking FWI and NOTIDE simulations into consideration. Section 2.4.5 deals with simulations SC1 and SC2.

2.4.1 The Estuarine Dynamics of the Goro Lagoon

The Goro Lagoon exhibits estuarine circulation due to the high freshwater input continuously received by the Po of Goro and pumping plants. This is clearly portrayed by the 2018 average circulation in Figure 2.6, where the lagoon's outflow is composed of surface fresher water (Fig. 2.6A), while at the bottom (Fig. 2.6B), an inflow of saltier water spreads into the interior region of the lagoon. The velocity across the vertical cross section of the inlet (Fig. 2.6C) helps to visualize and better understand the estuarine circulation.

A harmonic analysis of the simulated sea level by applying the T_Tide tool (Pawlow-

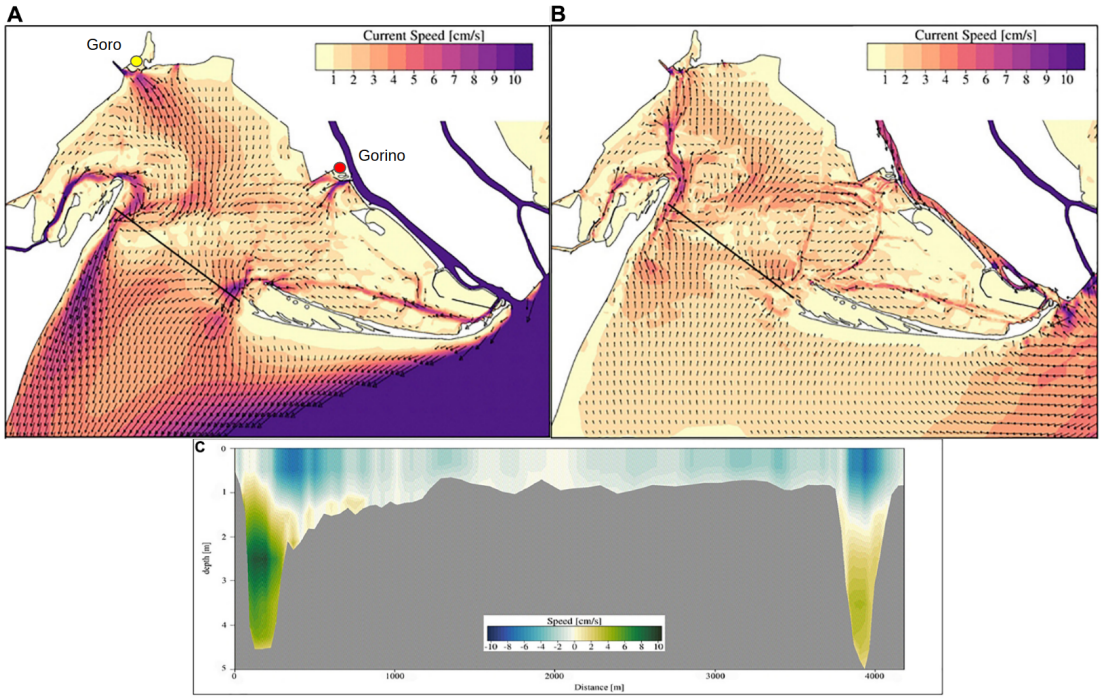

Figure 2.6: Average surface (A) and bottom (B) circulation, and (C) current speed across the vertical cross section of the inlet, indicated by the black lines at plots (A) and (B). Green colors indicate saltier water entering the lagoon, and blue colors indicate fresher water exiting the lagoon. The yellow and red dots indicate the position of the Goro harbour and Gorino, respectively. Source: Maicu et al. (2021).

icz et al., 2002) to three points within the domain reveals that the main tidal components are evenly transmitted within the lagoon. A reference point is taken at Porto Garibaldi (Fig. 2.1b). The phase delay and amplitude difference is computed for a point close to Gorino and for Goro Harbour (Fig. 2.6A) and are shown in Table 2.4. The circulation pattern remains the same during neap and spring tides. Current streamlines extend from the main channel to the western and central areas of the lagoon, and from the secondary channel toward Gorino and the eastern corner of the lagoon. During flood and ebb tides (Fig. 2.9) the current velocity is greatest in the inlet channels, reaching values of $1\,m/s$ and $0.8\,m/s$ respectively, for the main and secondary channel during spring tides and $0.5\,m/s$ for both inlets during neap tides (Fig. 2.9). Values of around $0.3\,m/s$ can be found during flood and ebb tides in the

	P.to Garibaldi			Goro Harbour		Gorino	
Tidal component	Period (h)	Amplitude (m)	phase (°)	Amplitude Difference (m)	Delay (min)	Amplitude Difference (m)	Delay (min)
M2	12.42	0.16	263.97	-0.01	15.9	-0.01	15.5
K1	29.93	0.14	58.45	0.00	6.6	0.00	6.4
S2	12.00	0.11	264.52	0.00	18.2	-0.01	17.5
P1	24.07	0.04	62.62	0.00	3.9	0.00	8.3
O1	25.82	0.03	60.78	0.00	29.6	0.00	30.3
K2	11.97	0.03	268.23	0.00	18.0	0.00	16.2
N2	12.66	0.03	264.89	0.00	23.8	0.00	23.3

Table 2.4: Characteristics of the Porto Garibaldi tidal signal and its modification inside the lagoon.

central shallow area of the inlet and in some of the main navigation channels of the lagoon (*e.g.*, the channel leading from Gorino to the main channel). In most of the other areas of the lagoon, the velocity does not exceed $0.2\,m/s$ - $0.1\,m/s$ during spring and neap tides, with even lesser values in marginal areas. The lagoon's net transport at

Model Layers	Western Channel	Central Tidal Flat	Eastern Channel
Flux Layer 1	-15.9	-39.2	-19.9
Flux Layer 2	3.0	-	-0.2
Flux Layer 3	12.6	-	4.0
Flux Layer 4	8.5	-	5.1
Flux Layer 5	2.1	-	2.1
Net Barotropic Flow	10.3	-39.2	-8.9

Table 2.5: Yearly mean volume fluxes through the three different portions of the section at the opening of the Goro Lagoon. Positive values indicate volume flux into the lagoon, while negative values indicate an outflow. The units are m^3/s.

the mouth is equal to $-37.8\,m^3/s$ which is differently distributed among the two inlets and the central tidal flat. The main channel has a positive net transport (inflow) of $10.3\,m^3/s$ when computed over the entire year of 2018. On the other hand, the eastern inlet has a negative net transport (outflow) of $-8.9\,m^3/s$. In the shallow central tidal

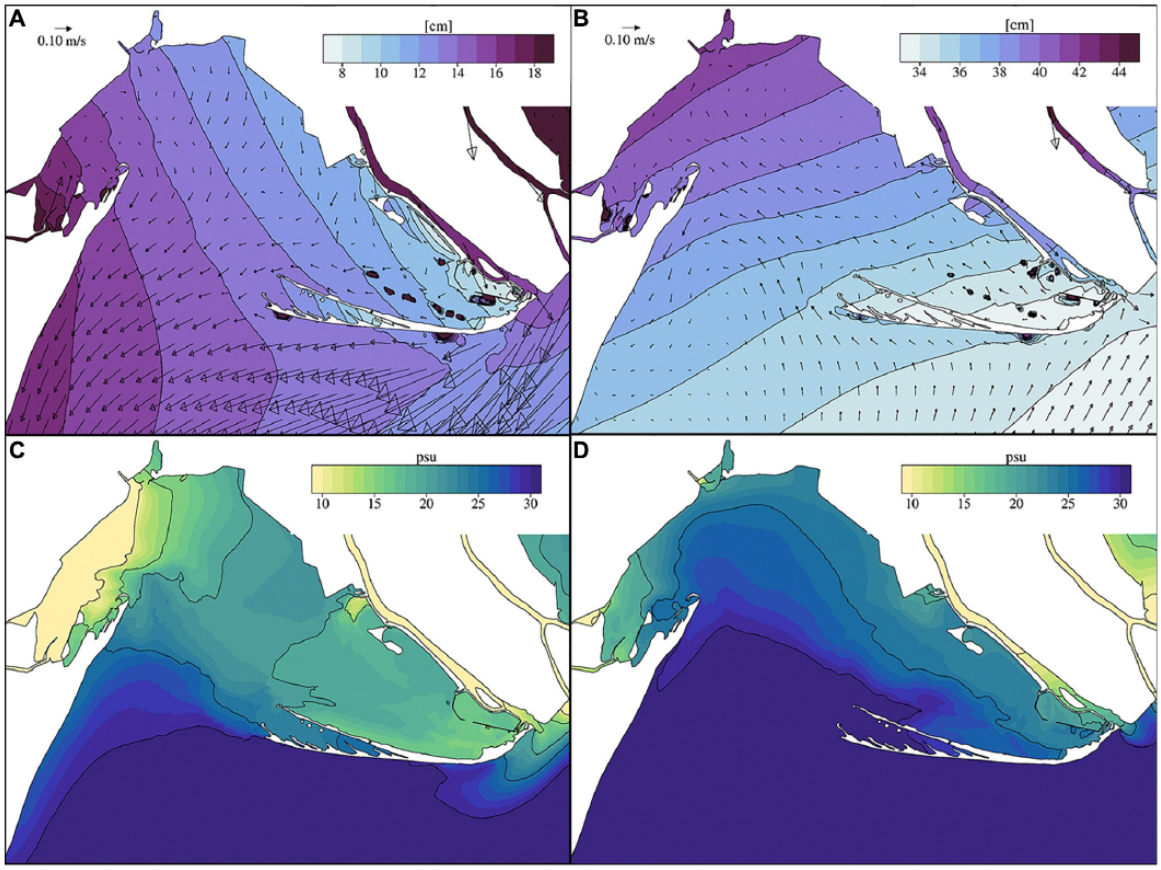

Figure 2.7: Mean sea level (A) and surface salinity field (C) during an intense Bora wind event that occurred in February 22-26, 2018. Means sea level (B) and surface salinity field (D) during an intense Scirocco wind event that occurred in October 27-31, 2018. Plots (A) and (B) show also mean surface currents. Source: Maicu et al. (2021).

flat the net transport is $-39.2\,m^3/s$ and is the main contributor to the seaward flux. Table 2.5 shows the yearly mean flux divided per layer, highlighting the mean outflow and inflow at the inlets. The largest volume of open sea water transport occurs in the western channel and the largest outflow of surface waters is from the central portion of the inlet section (Valle-Levinson, 2010; Valle-Levinson et al., 2015).

As land-locked lagoon, the importance of winds in generating changes in the circulation and the sea level within the lagoon cannot be underestimated. In the Adriatic Sea, the two dominant wind regimes, the Bora (NE) and Sirocco (SE) force the general circulation at short time scales (Orlić et al., 1994; Ursella et al., 2006; Jeffries and Lee, 2007). The morphology of the Po Delta coastline significantly modifies the coastal current in front of the Goro Lagoon (Falcieri et al., 2014; Maicu et al., 2018; Bellafiore

et al., 2019). The Bora strengthens the SW coastal current and piles up the water on the coastline south of the delta (Figure 2.7A). The effect of the Bora wind regime on the lagoon's average circulation is to force surface currents to exit the lagoon, in turn favoring the advection of low salinity waters over the whole lagoon (Fig. 2.7C). These meteorological conditions do not generally cause flooding in the Goro Lagoon while the Sirocco does. Figure 2.7B shows that during an intense Scirocco, the lagoon is exposed to an average increase in sea level of up to 10 cm and a re-circulation current pattern is generated in the lagoon's NW region. At the peak of the event (27-31 October, 2018), the sea level difference between the Goro harbor and the shelf outside the lagoon reaches 20 cm. The wind-driven average circulation at the inlet is mainly from the sea to the lagoon (Figure 2.7B) and higher salinity waters are advected into the lagoon (Fig. 2.7D).

The lagoon's hydrodynamics is generated by the non-linear interaction of tides, fresh-

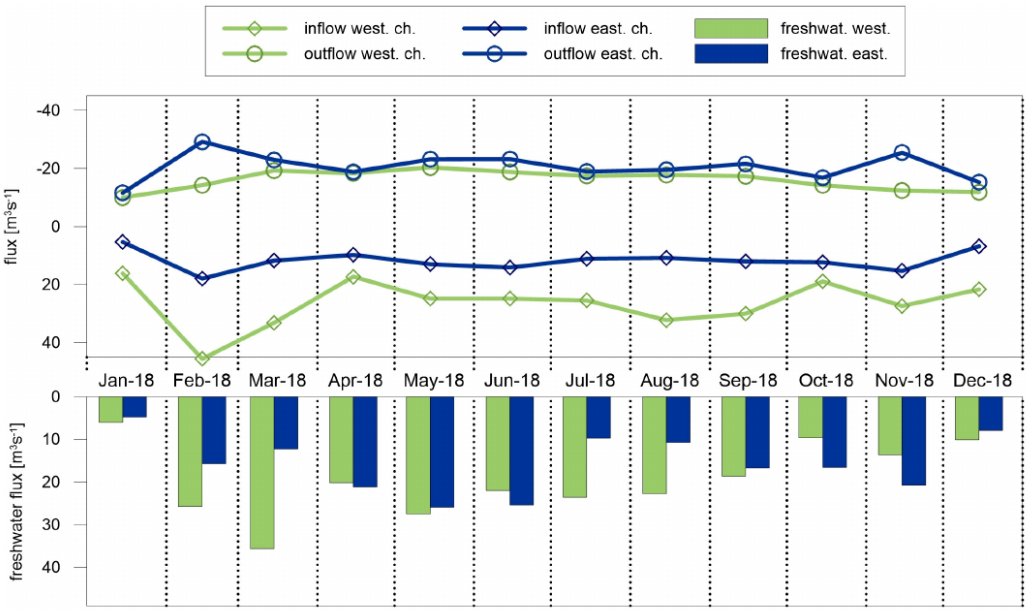

Figure 2.8: Average volume fluxes in the inlet channels, differentiated by inflow positive values (in the deeper layers) and negative outflow values (in the surface layer). The average freshwater inputs in the lagoon are considered positive. The western freshwater is the sum of the Po of Volano and the pumping stations of Giralda (G), Romanina (R), and Bonello (B) (Fig. 2.1). The eastern freshwater is the sum of the volume fluxes at the Manufatto gate and Gorino lock. Source: Maicu et al. (2021).

water inputs and winds. The average circulation is baroclinic for the whole year in both inlet channels (Fig. 2.8). The surface layer flux has strong variability and is related to the freshwater input's seasonality, while the bottom inflow is less variable with respect to the 2018 average. The 2018 monthly flux at the inlets in Figure 2.8 shows a western outflow following the Po of Volano and pumping plants' seasonality. On the other hand, the outflow at the eastern channel is less correlated to the Po of Goro's seasonality due to tidal and wind forcing inducing a partial redistribution of the freshwater volume throughout the lagoon. The deeper inflow is the largest in February and March, when strong N-NE winds increase the lagoon-open sea density gradients, as shown in Figure 2.7C, increasing the stratification and enhancing the baroclinic circulation (Scully et al., 2005).

The effect of freshwater on circulation and salinity was analysed in the FWI simulation, taking into consideration the period between 31 October to 24 November 2018, when the Po River flooded (Fig. 2.2). In the CNT experiment, the Gorino Lock was totally closed and the Manufatto was partially closed during the flood. In the FWI simulation they were both left open, leading to an increase in freshwater input of $48\,m^3/s$. This decreases the FWI salinity from -6 to $-10\,psu$ in the central lagoon, thus increasing the horizontal density gradient with a larger inflow of $4.8\,m^3/s$ in deeper layers.

If we remove tidal forcing, as in the NOTIDE simulation, for the period from 6 May to 6 June 2018, the result is an increase of $8.4\,m^3/s$ in the average freshwater inflow at Manufatto. This is an indirect effect of removing tidal forcing, working in the same direction as the increased discharge. This leads to an increased density gradient and a stronger gravitational circulation, also due to a lack of vertical mixing that occurs during flood tidal flow.

2.4.2 Tidal Asymmetry and Tidal Straining

Tidal asymmetry is weak but present. Flood and ebb almost have the same duration, with some exceptions where longer ebb tides are observed (no more than 1 hour difference), quite a common feature in the estuarine environment (Jay and Musiak, 1996). The effect of tidal straining, denominated "Strain Induced Periodic Stratifica-

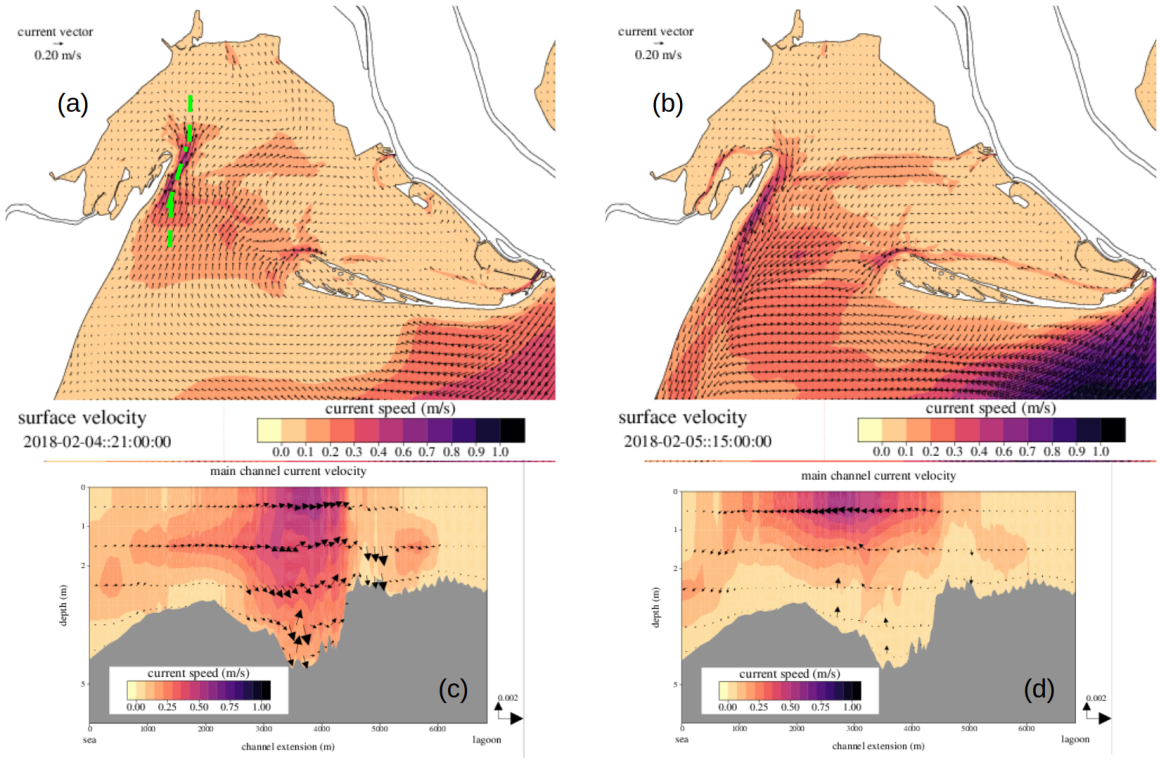

Figure 2.9: Surface current velocity for a flood (a) and ebb (b) during spring tides and the relative cross section (green dashed line in (a)) along the principal channel (c) and (d).

tion" (SIPS; Simpson et al., 1990), is relevant because the stratification is periodically destroyed during the flood, although occasionally, especially during neap tides, stratification can persist for more tidal cycles. During ebb flow, stratification is increased and persists for longer periods, which may contribute on average to an enhancement of the gravitational circulation. This is a common feature in the estuarine environment, and in some cases can be an important factor generating residual gravitational circulation (Burchard and Baumert, 1998), even though for the Goro Lagoon, tides also reduce the amount of freshwater entering the lagoon from the Po of Goro, hence influencing the residual circulation as will be shown later. Figure 2.9 shows the circulation pattern during a flood and an ebb tide with a cross section along the principal channel. The cross section in Figure 2.9c shows the velocity field's vertical structure at the height of a flood. It is evident how the entire water column is involved with the high vertical mixing. The final mixing effect can be seen in the salinity at the end of the flood (Fig. 2.10a) where stratification is almost absent. On the other hand, the cross section velocity field at the height of the ebb (Fig. 2.9d) is concentrated at the

surface with a strong enhancement of stratification and suppression of vertical mixing as can be seen in the salinity cross section in Figure 2.10b.

As suggested by Jay and Musiak (1996), tidal asymmetry can be attributed to the

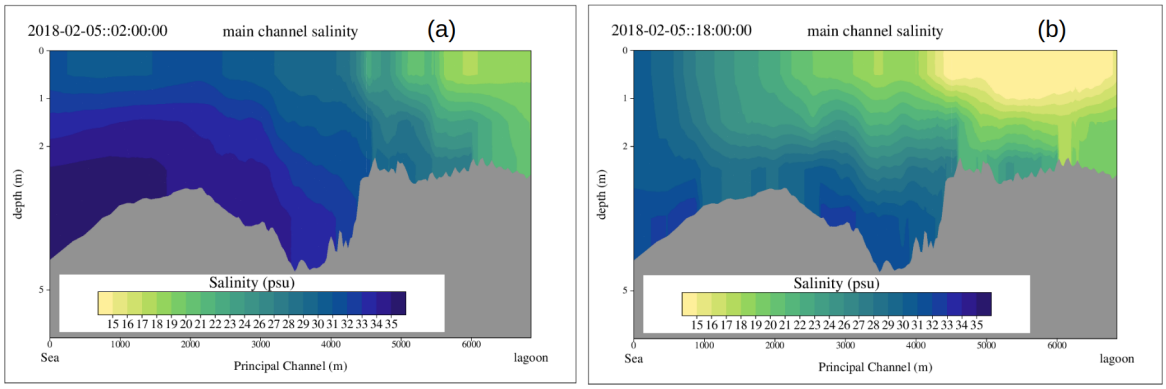

Figure 2.10: Salinity cross section along the principal channel (green dashed line in Fig. 2.9a) at the end of the flood (a) and ebb (b) tide .

non-linear interaction between the tidal wave and the bottom friction. This interaction generates overtides, *e.g.*, M4 derived from the M2 tidal wave, generating a shear flow that is in phase with the flood tide near the bottom and out of phase with the ebb, giving rise to the velocity profile that can be observed in Figure 2.9c,d. Figure 2.11 depicts the sea level from 5 February to 13 February 2018 and the volume flux for the principal channel for the same period. It is clear the reversal of the flux at each tidal cycle. It is interesting to note the presence of a baroclinic flow with a surface outflow and a bottom inflow at the beginning of the neap tide on 7 February when stratification is not broken by the flood tide.

2.4.3 Water Renewal Time

Water Renewal Time (WRT), (Cucco and Umgiesser, 2006) is an important parameter indicating the lagoon's replenishment with newer (and possibly more oxygenated) water (Fig. 2.12). The lagoon's average WRT is 5.8 days, with high spatial variability due to lagoon's specific morphology. WRT starts to increase beyond the mouth of the lagoon due to the central tidal flat's bathymetryc constraint. Water renewal from freshwater input coming from the Po of Volano and Po of Goro, respectively, is

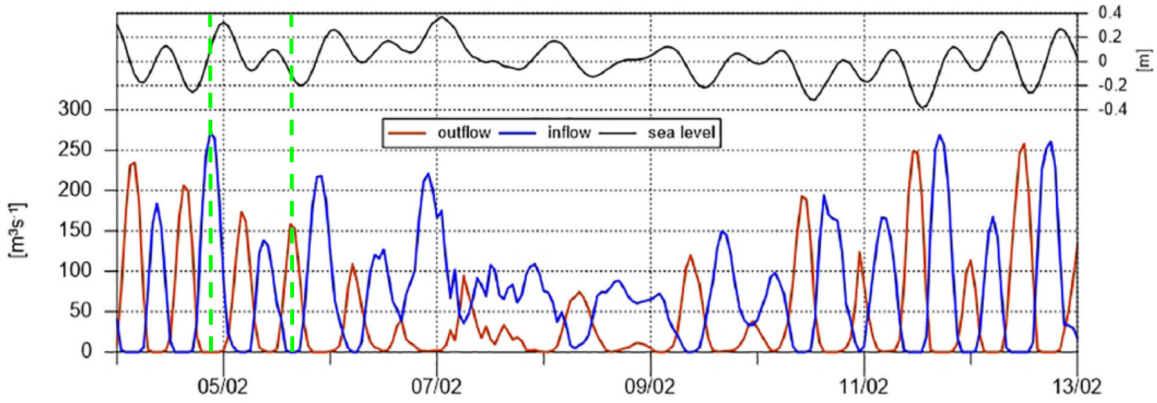

Figure 2.11: Time series of the net volume inflow/outflow in m^3/s^{-1} calculated in the western inlet channel (bottom) and sea level in m calculated at the B2 sampling point, for 1 week from February 5-13, 2018 (top). Source: Maicu et al. (2021).

guaranteed in the marginal western and eastern areas, while there is an increase in the NW area, where no freshwater sources are present. The highest WRTs (10-12 days) are found in the ex-nursery area between the two sand spits of the Scanno of Goro and in a western basin between the Scanno of Volano and the Po of Volano river outflow.

2.4.4 Salinity and Temperature

The Goro Lagoon's mean salinity (Fig. 2.13A) is deeply influenced by the freshwater input from the western and eastern sides. Low mean values of about $10\,psu$ or even less are found in the western side, with also less variability, as can be seen by the standard deviation in Figure 2.13B, due to the more stable freshwater flux at the Po of Volano. On the eastern side salinity values are of 13 to $16\,psu$ with a higher standard deviation ($6-8\,psu$) caused by the strong seasonality of the Po of Goro. Mean salinity in the central part of the lagoon is between $20\,psu$ at the northern side and $26-27\,psu$ at the mouth. The daily standard deviation of salinity is $4-5\,psu$, with most of the mixing that occurs due to the tidal cycle at the lagoon mouth and Po of Goro mouth.

The GOLFEM grid also partially resolve the Po delta structure. Therefore, it can be used to evaluate important parameters related to rivers, such as the saltwater intrusion, which in a depressed environment like the Po Valley, where agriculture is

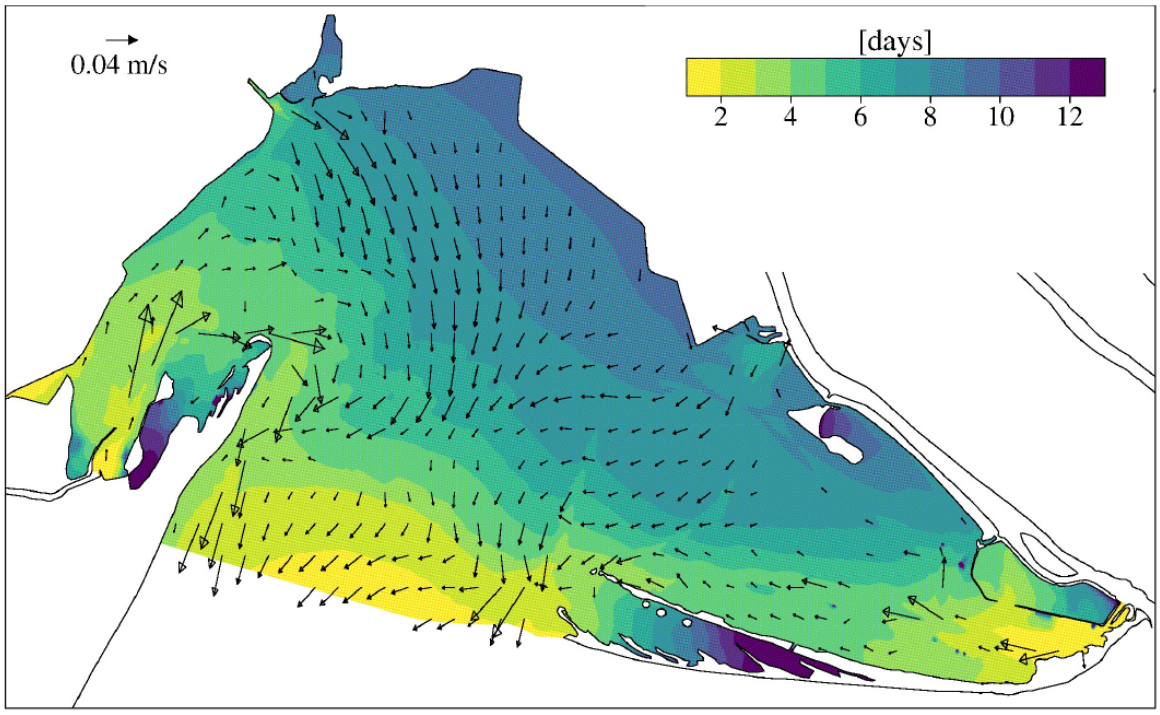

Figure 2.12: Average water renewal time and surface circulation calculated in 2018. Source: Maicu et al. (2021).

very widespread, must be accurately monitored to avoid damage to cultivation as a result of saltwater contamination of fresh groundwater aquifers. To asses saltwater intrusion, the salinity cross section was analysed along the Po of Goro thalweg (Fig. 2.14), which is indicated by the red dashed line in Figure 2.13A. The period covered is July-October 2018, when the Po River discharge at Pontelagoscuro was $845\,m^3/s$ with a standard deviation of $130\,m^3/s$. Figure 2.14 shows the classical salinity and current velocity pattern for an estuarine environment, with freshwater going downstream over a layer of saltwater going upstream at the bottom. During this period, average saltwater intrusion was $13\,km$, such that the bottom salinity values is between 2 and $3\,psu$. This result is in agreement with measurements taken by the Ferrara provincial authorities between 2003 and 2009 for a similar range of freshwater discharge. The maximum extension of saltwater intrusion is $20\,km$ in August 2018, when the minimum Po River discharge of $600 - 650\,m^3/s$ is observed. One consequence is that water entering the lagoon at the Manufatto and the Gorino lock is brackish, with an average salinity of 9 and $5.5\,psu$ respectively.

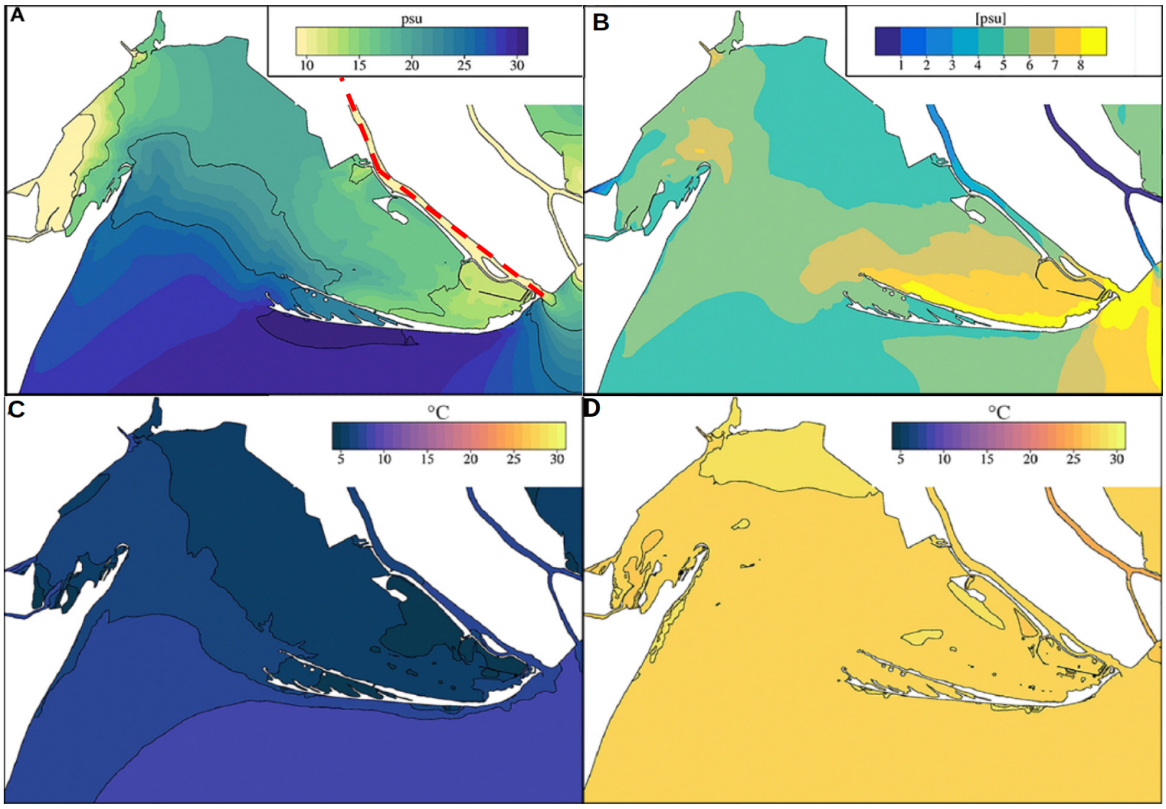

Figure 2.13: The Goro Lagoon's mean surface salinity for 2018 (A) and yearly standard deviation (B). The bottom panels depict the average temperature in February (C) and August (D) for the Goro Lagoon in 2018. The red dashed line in (A) indicates the cross section shown in Figure 2.14. Source: Maicu et al. (2021).

The lagoon's 2018 monthly surface temperature reached its minimum and maximum in February and August respectively. The temperature in August has low spatial variability, with a basin average of $27.9\,°C$ and a standard deviation of $0.24\,°C$. In winter, the difference between the lagoon and the open sea temperature is higher, with the lagoon being colder by up to $4\,°C$ in December. The basin average temperature in February is $6.0\,°C$ with a standard deviation of $0.68\,°C$. Temperature stratification is low and limited to the channels, where there is colder surface water with a vertical gradient of $-1.5\,°C$ in winter, while surface water starts to warm up in April when the vertical gradient is $1\,°C$. The lagoon's temperature is influenced by a number of elements, the most significant being the heat flux exchanged with the atmosphere, which practically equally affects the lagoon area. An important role is also played by the tidal cycle, at diurnal and semi-diurnal frequency, particularly affecting the lagoon

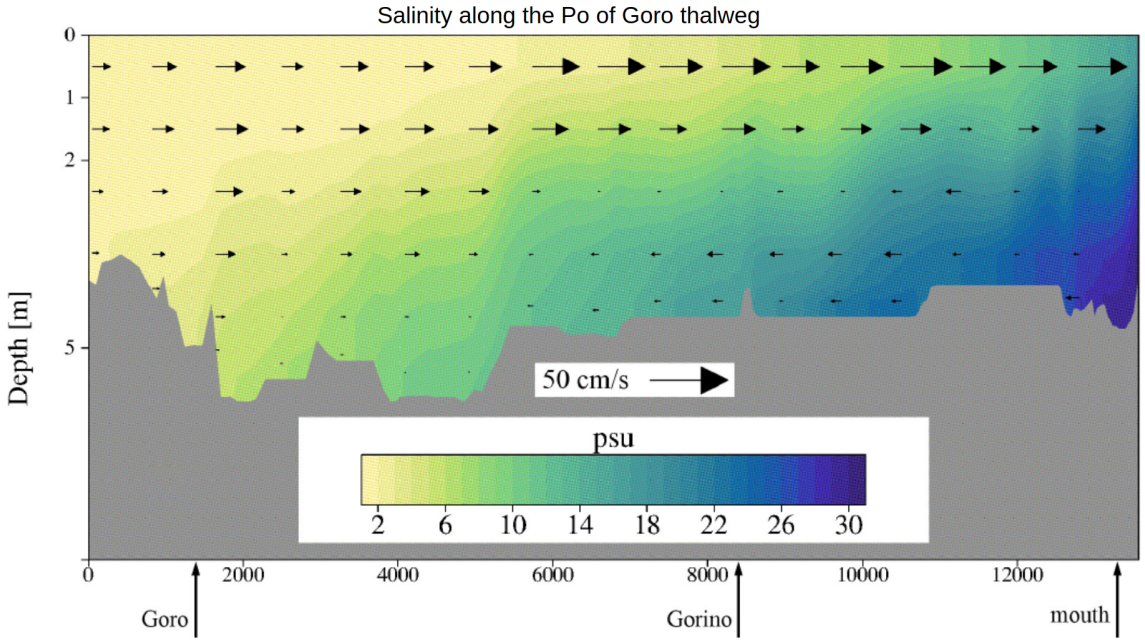

Figure 2.14: Period July-October 2018: average salinity along the axis of the Po di Goro branch and superimposed average current. Source: Maicu et al. (2021).

near the mouth where the mixing of lagoon and open sea water occurs. A minor role is played by the water temperature of the freshwater sources discharging into the lagoon.

2.4.5 What-if Scenarios

The GOLFEM model's calibration phase was a necessary step in developing a reliable model that was subsequently validated for the entire year of 2018 with positive results. The lagoon's ecosystem health and productivity levels are connected to the area's morphology and dynamics, the hydrodynamic regime, freshwater inputs, water salinity, and the specific ecosystem of the area. All these aspects concur to produce suitable conditions for the lagoon's biological productivity. Therefore, a reliable model capable of accurately reproducing physical interactions can be used for "what-if scenarios" to investigate the possible effects on productivity as a result of morphological interventions on the lagoon. The authors could only address factors concerning changes in morphology, hydrodynamics and thermodynamics at the time of the writing (coupling with biogeochemistry is ongoing).

Two what-if scenarios are evaluated here, indicated as SC1 and SC2 in the Table 2.3.

Both scenarios concern changes in the lagoon's morphology which are expected to improve the lagoon's hydrodynamic conditions (and thus its productivity). The two interventions to be evaluated were suggested by fishing cooperatives in agreement with the local authorities. The first, referred to as SC1, is the enlargement and deepening of the secondary channel on the eastern side of the lagoon mouth, indicated by the red contour in Figure 2.1a. The channel currently has a width of about $50\,m$ and a depth varying from 5 to $1.5\,m$ near the sea outlet where most of the sand is deposited from the along-shore sediment transport. The SC1 scenario foresees an enlargement of the secondary channel to a width of $100\,m$ and an even depth of $4\,m$ along the entire length of the channel. The morphological changes of the SC2 scenario are indicated by orange lines in Figure 2.1a. They involve the dredging of new channels, $30\,m$ in width and $3\,m$ in depth, in the area between the two spits of the Scanno of Goro. This was once a nursery area for clams, which degraded with the growth of the spit enclosing the area that is now lacking in oxygen and can no longer sustain the clam nursery. The low hydrodynamic activity is also highlighted by Figure 2.12. This is the area with the longest WRT, which has an average value of 12 days.

The analysis of results was carried out by evaluating the differences in salinity and current velocity for SC1 and SC2 compared to the CNT experiment. As differences in the mean velocity field were negligible, differences in the maximum amplitude were evaluated by extracting the max value every $12\,h$ (*i.e.*, over a tidal cycle). The results of the computation are shown in Figure 2.15. The enlargement and deepening of the secondary channel in SC1 led to a mean increase in salinity in all the eastern part of the lagoon with values up to $+3.5\,psu$ (Fig. 2.15A). The rise in current velocity is limited to the channel, where it reaches $+15\,cm/s$, and to the nearby NE and S areas where the increase is reduced from 1 to $4\,cm/s$ (Fig. 2.15B). A drop in velocity amplitude of up to $5\,cm/s$ is recorded NW of the channel, a consequence of the increased velocity in the secondary channel. Only during spring tides does the inflow/outflow flux at the eastern inlet increases by $8-10\%$, while it is negligible during neap tides.

The same analysis was carried out for the SC2 scenario. In this case there is a double effect on salinity due to the new channel connecting the ex-nursery area with the SE part of the lagoon, where mean salinity increases of $5.5\,psu$ are recorded (Fig. 2.15C),

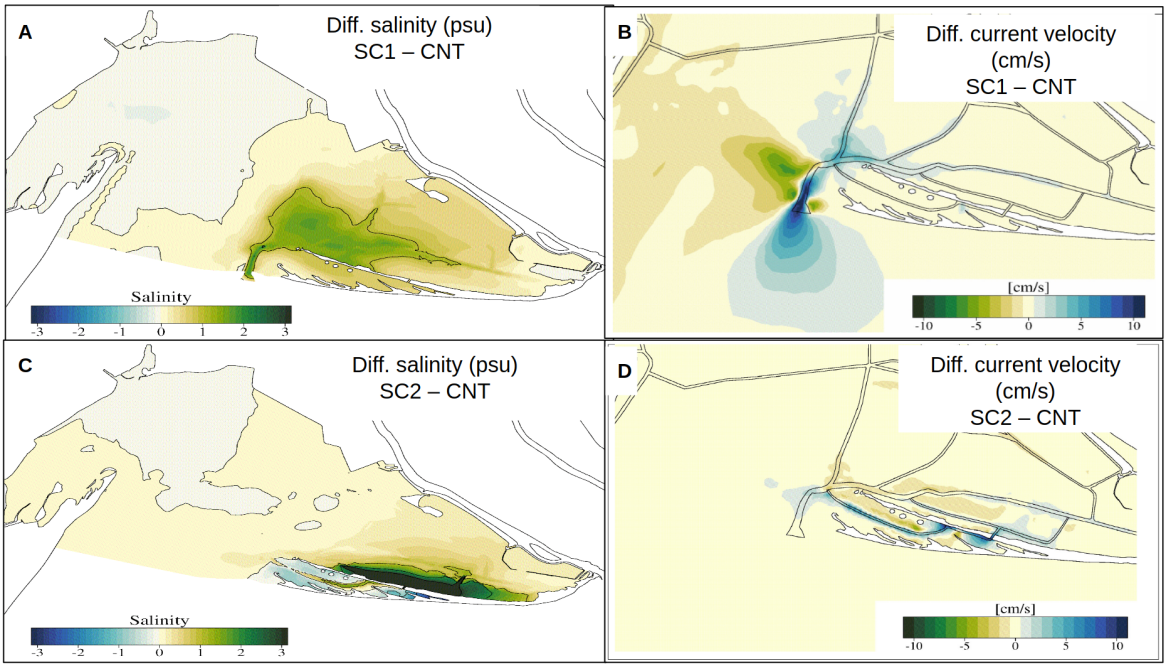

Figure 2.15: Plots (A) and (C) show the vertical integrated salinity difference between CNT simulation and SC1 and SC2 respectively for the 2018. Plots (B) and (D) show differences in maximum current velocity amplitude between CNT simulation and SC1 and SC2 respectively for the same period.

with a very localised maximum increase of $10\,psu$ near the channel dredged in the internal spit that allows the ingress of sea water during flood tides. However, since the lagoon's SE area is heavily influenced by the freshwater from the Po of Goro, when the channel is cut, fresher water flows into the ex-nursery area, lowering the salinity between the spits from 1 to $2\,psu$. The effects on current velocity are limited to the new channel's extension, where a slight increase in velocity is observed and a small decrease of $1-2\,cm/s$ is shown in the surrounding areas (Fig. 2.15D).

Two "fitness indices" (FT), developed in a previous study (Istituto-Delta-Ecologia-Applicata, 2004), were considered for a better insights into the relationship between clam productivity and changes in lagoon morphology. The two indices used here range from 0 to 1 and are related to the lagoon's hydrodynamic (FT1) and salinity (FT2). The indices are shown in Figure 2.16. A threshold of 0.5 is defined. Optimal clam growing conditions are considered only when the indices exceed this threshold. For FT1 there are optimal conditions for barotropic velocity values ranging from 0.2 to

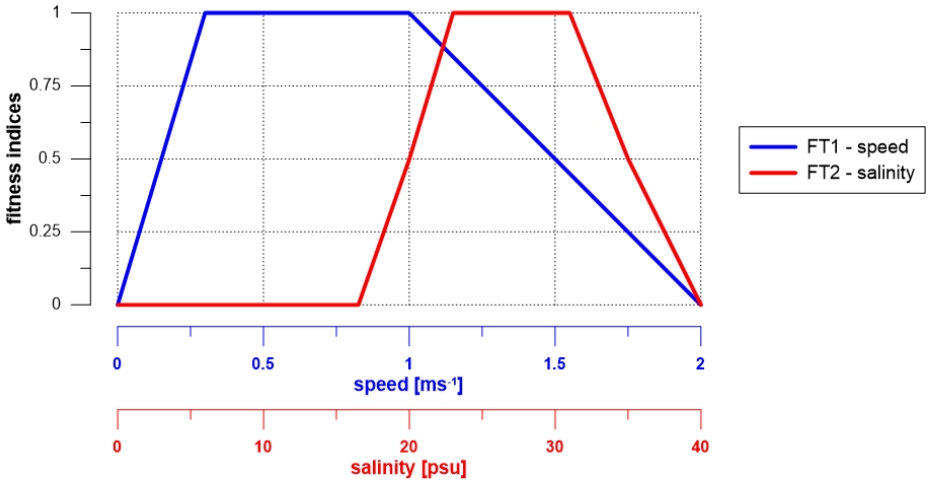

Figure 2.16: Fitness hydrodynamic and salinity indices for the growth of *T. Philippinarum*. Optimal conditions for the Clam growth occur when the indices are equal or exceed 0.5. Source: Maicu et al. (2021).

$1.5\,m/s$ while for FT2 bottom salinity values for optimal conditions are between 20 and $35\,psu$. The percentage of time in which FT1 and FT2 stay above the threshold value was then computed, resulting in FT1 and FT2 being considered as the percentage of time with optimal conditions. Results are presented in Figure 2.17 where FT1 and FT2 are shown for CNT together with the differences between the two indices for SC1 and SC2 with respect to CNT. Most of the clam farms are located in an area where FT2 is higher than 60 %. A more limiting factor is given by FT1, which is also the most important index. However, this index is influenced by the tidal cycle, when current velocity is reduced to zero due to tidal inversion. As expected, the ex-nursery area shows a very low FT1 value, due to the weak hydrodynamics of that area, in agreement with the high WRT value found there. The results for SC1 and SC2 reflect what was observed in salinity and velocity differences (Fig. 2.15). For SC1 there is an increase of $10 - 12\,\%$ in FT2, which spreads in the lagoon's eastern area due to the increase in salinity. For FT1, the increase is limited to the channel (10 %) and the nearby NE area ($3 - 5\,\%$). However, there is a maximum decrease of $-10\,\%$ in FT1 to the west of the channel, spreading westward and decreasing from -1 to $-3\,\%$. For SC2, changes are more significant as regards FT2, with values of up to $+15\,\%$ recorded in the lagoon's SE area and producing a decrease between -3 and $-7\,\%$ in

the ex-nursery area (except the channel itself), where fresher water flows from the Po of Goro. The effects on FT1 are almost negligible with only a localized increase in the channel.

FT1 and FT2 are only a part of the total productivity index (although FT1 is the

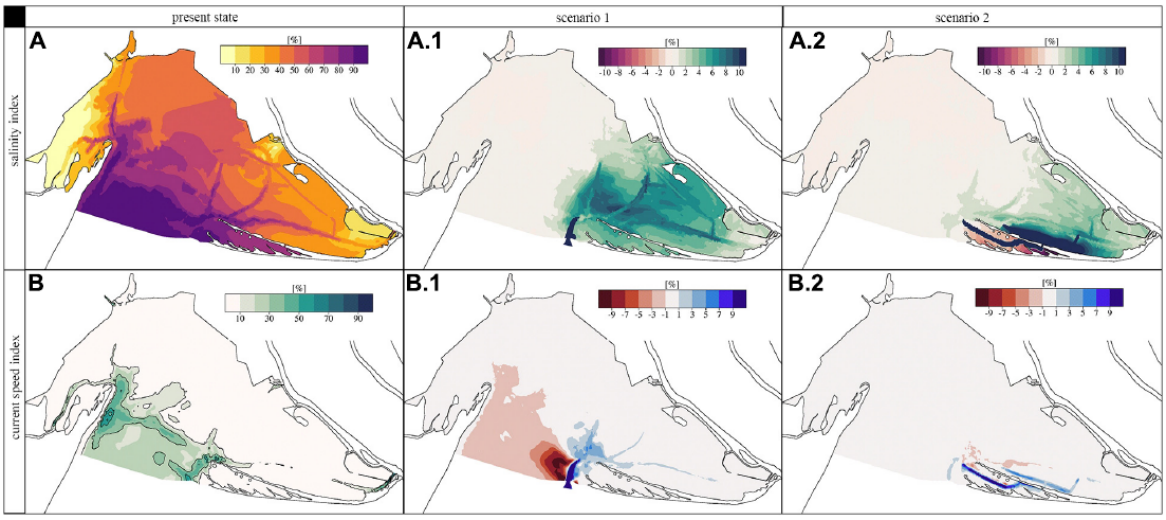

Figure 2.17: Fitness indices for optimal clam growing conditions as a result of CNT simulation for salinity (FT2, A) and current velocity (FT1, B). Differences between SC1 and CNT for FT2 (A.1) and FT1 (B.1). Differences between SC2 and CNT for FT2 (A.2) and FT1 (B.2). Source: Maicu et al. (2021).

most important), also accounting for sediment grain size, oxygen and bathymetry. To this end, multiple interventions need to be undertaken to improve the lagoon's hydrodynamics. SC1 has a positive influence in the SE area of the lagoon, while a slight negative effect should be accounted for to the west of the secondary channel. The SC2 scenario has no positive effects on the ex-nursery area for FT1 and FT2, even if a reasonable reduction in WRT is observed and can not be ignored.

2.5 Concluding Remarks

The very high resolution unstructured model GOLFEM was implemented in the Goro Lagoon, in northern Adriatic Sea. The Goro Lagoon is known, at national and international levels, for its clam production. However, euthrophication may occur during summer with the risk of anoxic events and consequent clam death and economical

losses for the population. In this work GOLFEM was used to study the lagoon's dynamics and evaluate two "What-if scenarios" (SC1 and SC2) that were designed with local stakeholders to assess the dynamical impact of dredging works in the lagoon and possible effects on clam productivity. The results evidence the estuarine dynamic of the lagoon, essential to keep acceptable salinity values, highlighting the importance of the freshwater influence in the lagoon. The assessment of the "what-if scenarios" is carried out with the help of two indices accounting for clam productivity and connected to current velocity (FT1) and salinity (FT2). The SC1 consider the enlargement and deepening of the eastern inlet, while SC2 account for dredging of new channels between the two spits (the ex-nursery area). In SC1 the saltwater intrusion in the lagoon's eastern area lead to a 10% increase of FT2. However, the FT1 increase is localized only in the channel and a $-10\,\%$ decrease is observed NW to the inlet. In SC2 the FT1 increase is negligible while FT2 slightly increase in the SE lagoon's area due to saltwater intrusion and decrease between the two spits due to freshwater coming from the Po of Goro. In conclusion SC1 shows some productivity improvement due to the increase of salinity in the lagoon's eastern area, however the decrease of FT1 NW the inlet indicates a slight reduction of productivity. Contrary to what expected, SC2 shows no improvement of productivity in the ex-nursery area.

Chapter 3

Ensemble Storm Surge Modelling of the Goro Lagoon

In this chapter GOLFEM is used to develop an ensemble prediction system (namely GOLFEM-EPS) to improve the forecast of Sea Level (SL) during extreme events affecting the Goro Lagoon and the surrounding areas. The storm surge hazards are introduced and an overview of Ensemble Prediction System (EPS) methods is provided. The ensemble technique is applied to five recent extreme events, providing an estimate of the uncertainty due to each forcing. The EPS is composed by 45 members forced by different atmospheric and open-ocean models and river run-off perturbations. The Ensemble Mean (EM) is computed with simple average and through a weighting technique to find an improved Weighted Ensemble Mean (WEM). For a very limited-area model, such the one here presented, it is found that the greatest uncertainty is given by the open boundary conditions. Furthermore, the tidal signal propagated from the boundaries may strongly contributes to the sea level uncertainty.

3.1 Introduction

The operational forecast of SL is a widely spread service to prevent flooding and storm surge hazards that represent a potential threat for human life and activities (Chaumillon et al., 2017; Forzieri et al., 2016). However, there has been no success up to date in really using the SL forecast for early warning of inundation and damage

forecasting mainly due to the high computational modelling requirements for both atmospheric and ocean numerical models (OECD, 2019) and the additional problems associated with climate change (Emanuel, 2017).

The northern Adriatic Italian coast represents a vulnerable area due the presence of important cultural heritage sites (*e.g.*, Venice), the land subsidence and the important socio-economic activities occurring all along its coastal beaches, all determining a high coastal risk due to storm surge.

3.1.1 Flooding Hazard in the Adriatic Sea

Flooding events are the consequence of a superposition of multiple forcing (Fig. 3.1). The most relevant are tides and the surge component due to wind forcing and atmospheric pressure. Tidal forces are related to the astronomical movements of Moon and Sun and, to minor extents, to the other planets of the Solar System. Depending on the geographical position, the tidal range can be classified as micro-tidal (up to $2\,m$), meso-tidal (between 3 and $4\,m$) and macro-tidal (higher than $4\,m$). Tides can be treated as a linear combination of an infinite number of harmonic components. However, for practical uses, the eight principal diurnal and semi-diurnal components are often considered (K1, O1, P1, S1, K2, S2, M2 and N2) enough to model the major features of the tidal dynamics (*e.g.*, , spring-neap cycle). Tides propagate as long gravity waves under the influence of the Coriolis force due to earth rotation. The velocity and features of tidal propagation strictly depend on the shape and depth of the basin bathymetry. The interaction of tidal waves with the coasts produces Kelvin waves that propagate along the coast. In the Adriatic Sea, Kelvin waves propagates counter-clockwise at semi-diurnal periods, while topographic waves travel across the basin at diurnal periods (Malačič et al., 2000). When tides reach shallow waters, the nonlinear interaction with the bottom become important, tides may be distorted and resonance phenomenon can arise, with an amplification of the tidal forcing. (Speer and Aubrey, 1985).

The meteorological contribution to storm surges manifests itself in two ways. The most important is the stress exerted by the wind on the sea surface. The direct action

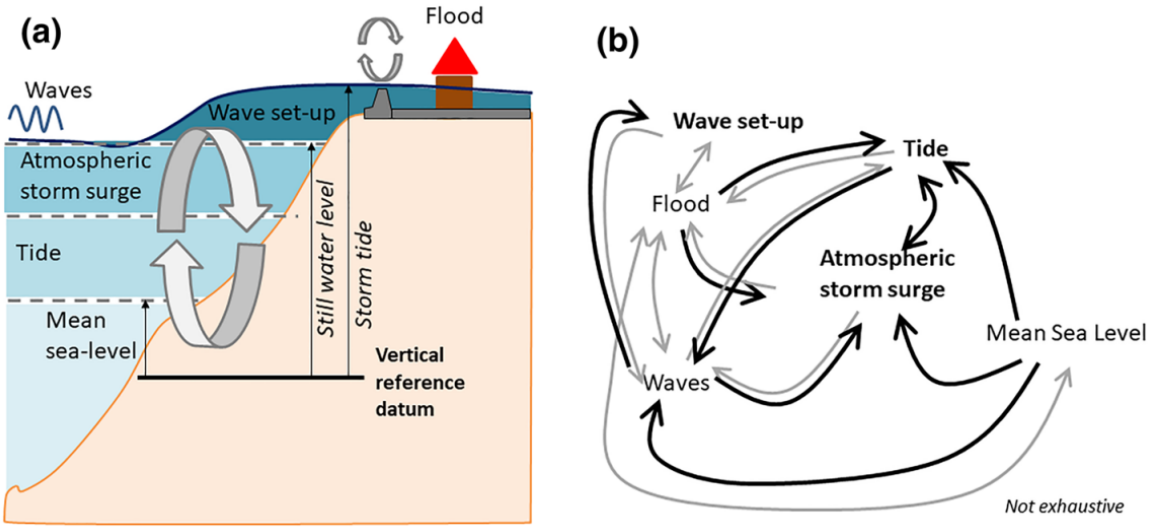

Figure 3.1: Principal physical components of a storm surge (a) and their interaction (b). Source: Idier et al. (2019).

of the wind generates a "wind set-up". The water moved by the wind forcing slows down in shallow water due to bottom friction, causing water to pile-up. In the Adriatic Sea this condition occurs more likely when the Scirocco (SE direction) wind blows for several days (Orlić et al., 1994). However, the Bora wind (NE direction), that usually has larger amplitude, is the most threatening, especially if concomitant with high tides and with an already established Scirocco wind blowing in the southern part of the Adriatic (Lionello et al., 2021). The second contribution is the "inverse barometer effect". Atmospheric perturbations are usually connected to a pressure drop, and the SL adjusts to atmospheric pressure changes. A pressure drop of $1\,hPa$ corresponds approximately to an increase of SL of $1\,cm$.

As a consequence of the wind stress, wind waves are generated which, approaching the shallow waters, may be threatening depending on fetch, wind intensity, bottom and coastal geometry. Eventually, the breaking waves transfer momentum to the flow (*i.e.*, the radiation stress; Longuet-Higgins and Stewart, 1964) that may cause a further rise (or fall depending on waves direction) of the SL, the so called "wave set-up". During storm events, and especially with Bora wind conditions, waves can reach a significant height $Hs > 3\,m$ (Armaroli et al., 2009) along the ER coast, representing an actual risk for the coast. The wave set-up adds to the SL excluding only wave run-up con-

tributes (Fig. 3.1a) to coastal inundation and coastal erosion (Ciavola et al., 2007).
In the Adriatic Sea, *e.g.*, a semi-enclosed sea, seiches can be generated in response to the wind. The Scirocco wind blowing over the Adriatic Sea can trigger the fundamental mode of seiches with a period of 21.2 hr and a decay time of about 3.2 d (Cerovečki et al., 1997) and an amplitude rising up to 50 cm (Godin and Trotti, 1975). Hence, the seiches can contribute to high SL values if they superimpose with a storm surge enhanced SL (Vilibić, 2006; Bajo et al., 2019). The first and second mode of the Adriatic Seiches have a 10.7 hr and 6.7 hr period, respectively (Raicich, 1999), and a much more smaller amplitude that usually does not represent a threat.
The inter-decadal and inter-annual SL variability can also play a role in setting favorable conditions for inundation events (Lionello et al., 2021) as well as long-term meteorological forcing due to long planetary waves (Pasarić and Orlić, 2001).
The so called meteotsunamis can occasionally occur in the Adriatic Sea, triggered by Proudman resonance (Proudman, 1929). This phenomenon occurs when the speed of an atmospheric disturbance matches the speed of long ocean waves and may be the cause of some flooding events that occurred along the Adriatic coasts (*e.g.*, , Vela Luka Bay; Orlić, 1980).
The Goro Lagoon, which is the application of this study, is exposed to storm surges that threaten the towns around the lagoon (Bondesan et al., 1995). On 4 November 1966, a dramatic flooding event (Garnier et al., 2018) caused by a persistent and strong Scirocco wind, caused serious damage to buildings, roads and cultivated lands. In the Goro town almost 80 families were moved away from their homes. In more recent times, on 28 October 2018, another Scirocco event (see Section 2.4.1) caused the inundation of the Goro harbour. The EPS system developed here is thought to be the final part of the early warning system running operationally at Arpae.

3.1.2 Ensemble Forecasting Methodology

In a complex system such the ocean, described by nonlinear equations, the multiple sources of uncertainty can amplify and destroy the capacity to predict environmental conditions. The accurate knowledge of the initial state of the ocean is of paramount

importance as well as the atmospheric forcing (Pinardi et al., 2011). Many predictability studies have focused on the model response to initial values perturbations, while less efforts were given to boundary values perturbations (Chu, 1999). In coastal domains, even rivers may represent a source of uncertainty. The measure in which each forcing contributes to the uncertainty of the forecast depends on a number of factors (*e.g.*, the dimension of the domain, the type of boundary conditions, the model used to force the system, etc.). The physical parametrizations and the specific numerical schemes used in the ocean models add further uncertainty to the system.

While the first deterministic storm surge numerical forecasting systems were developed throughout the 1960s and 1970s, ensemble systems only started to appear in 2000s for an estimation of the forecast uncertainty (Pinardi et al., 2017). The notion of ensemble forecast first emerged in the pioneering work of Lorenz (1963), where the sensibility to initial conditions was demonstrated for a simple nonlinear system. Across the 1960s it was already clear that there was a "limit of deterministic predictability" in weather forecast (Palmer, 2018). During the 1980s and 1990s much efforts were done to develop ensemble weather forecasting systems leading eventually to an operational system at the European Centre for Medium-range Weather Forecasting (ECMWF) (Palmer et al., 1992; Molteni et al., 1996) and at the National Meteorological Centre (NMC) (Toth and Kalnay, 1993). Further developments arose with the concept of multimodel ensemble and superensemble (Krishnamurti et al., 2000). Considering output from different models to create an ensemble system (multimodel concept) allows to limit the systematic errors that can affect a single model. Instead of generating the EM with a simple process, where each model has the same weight, the superensemble procedure consists in applying different weights (depending on the chosen metrics) to each output based on the performance of each model during a training period to generate a WEM. In oceanography, the multimodel superensemble concept was applied for the Mediterranean Sea Sea Surface Temperature (SST) forecasting by Pistoia et al. (2016) using a multiple linear regression technique applied to a multi-physics and multi-model dataset. The Mediterranean Sea was indeed the subject of early ensemble systems for the determination of ocean response to the surface wind uncertainty (Pinardi et al., 2008; Milliff et al., 2011; Pinardi et al., 2011).

Nowadays, different storm surge forecasting systems are already operational in European seas, mainly run by national institutes and international consortium (for a detail review see Umgiesser et al., 2021), but only a few of them use an ensemble approach. A first EPS was made operational by Flowerdew et al. (2009) with further verification of the results in Flowerdew et al. (2010) where the sensibility of surge forecast to meteorological forcing and initial conditions were studied.

A multimodel storm surge EPS is operational in the North sea, combining a series of storm surge forecasting systems using a Bayesian Model Average (BMA) to weight each individual forecast (Beckers et al., 2008). The same methodology was applied in the western Mediterranean (Pérez et al., 2012). A multimodel EPS approach was also developed for the Adriatic Sea by Ferrarin et al. (2020), where several operational forecasting systems are used to generate an EM and to assess the uncertainty. Outside Europe, a mulitimodel EPS is applied in the coastal area of New York (Liberto et al., 2011).

Different post-processing techniques can be applied to the ensemble members to have a reliable mean (the superensemble), that for the case of storm surge are well described in Salighehdar et al. (2017). Beyond the already cited BMA, weights can be computed using other metrics, such correlation or standard deviation together with bias correction, or the estimation of RMSE on a training period. Moreover, only a subset of the members can be used, discarding those members with poor performance.

In this work the possibility to implement a storm surge EPS (GOLFEM-EPS) with a baroclinic very high-resolution model (GOLFEM; Maicu et al., 2021) is investigated considering five recent extreme events, using forcing from different meteorological and ocean operational models and also perturbing the rivers discharge. The GOLFEM model was extensively described in Chapter 2 and includes the Goro Lagoon, the Po River Delta and the surrounding areas. The sources of uncertainty are evaluated and the performance of the ensemble is assessed also considering some techniques from the superensemble concept. The Surge Residual (SR), *i.e.*, the SL after removing the astronomical tides, is analysed to evaluate the storm surge components.

3.1.3 Goro Lagoon Extreme Events Description

All the extreme events described here (see Table 3.1) were collected from Perini et al. (2020) and Perini et al. (2019), which gave an exhaustive description and statistics of the extreme events and their impacts on the ER coast. The events for this study

Event No.	Date	P.G. tide gauge max time(UTC),SL(m),SR(m)	Faro tide gauge max time(UTC),SL(m),SR(m)	Impacts	Prevailing winds
1	2019-12-23	07:40 -> **1.17**, **0.56**	07:50 -> **1.21**, **0.60**	spread impacts	NW
2	2020-10-03	10:50 -> **0.86**, **0.51**	10:30 -> **0.82**, **0.51**	no impacts*	SE
3	2020-12-02	08:20 -> **1.02**, **0.61**	08:30 -> **0.93**, **0.54**	spread impacts	N-NE
4	2020-12-08	15:30 -> **1.06**, **0.96**	15:10 -> **1.10**, **0.85**	Ferrara province	E-SE
5	2020-12-28	08:30 -> **0.90**, **0.72**	09:00 -> **0.90**, **0.78**	minor impacts Volano	SE

Table 3.1: Events analysed in this study, with date, hour, max observed SL and max observed SR at P.to Garibaldi and Faro. Impacts and prevailing wind for each event are also indicated. The (*) for event 2 means that for this event, even if there were no impacts, an alert was sent by the Arpae-SIMC early warning system.

were chosen also based on the availability of data (observations and input model data) more than on their impacts on the coast. This is why important events, like the one occurred on 12 November 2019 and that caused the flooding of Venice are not present. The event 1 is considered a minor event of 2019, even though it caused some impacts on the coast. A low pressure system moving NE produced NW winds along ER coasts, with maximum wind speed between 8 and 15 m/s. Due to the NW winds, the SR tendency was to decrease. However, an exceptionally high tide was in phase with a seiche wave, leading to a total SL exceeding critical thresholds.

Events 2, 4 and 5 were caused by an intense Scirocco generated by low pressure systems centered in the western Mediterranean, south of the Alps for event 2 and 5 and in the Tyrrhenian sea for event 4. Some impacts were recorded in the Ferrara province coastal area for event 4 as well as for event 5.

Event 3 was triggered by a Bora (NE) event due to an intensification of a low pressure system in the Ligurian Gulf. The wind reached values between 15 and 20 m/s causing some impacts along the northern part of ER coast.

3.2 Datasets and Model Set-up

The deterministic model used to run the ensemble is GOLFEM (see Chapter 2 for more details). In this section the model set-up is briefly discussed and the forcing model and data, used to build the ensemble, are listed and characterized.

3.2.1 Multi-Model Forcing and Observations

Multiple operational and pre-operational meteorological and ocean model outputs were used to build the forcing for the ensemble system simulations (Table 3.2).

		Ocean model				
Meteorological Model	**River Forcing**	**Adriac (An + Fc)**	**AdriaRoms (An+Fc)**	**Med-currents (An+Fc)**	**Global (An+Fc)**	**Med-currents with tides (An+Fc)**
Cosmo-2I (An+Fc)	**data**	*exp-1*	*exp-10*	*exp19*	*exp-28*	*exp37*
	data−30 %	*exp-2*	*exp-11*	*exp-20*	*exp-29*	*exp-38*
	data+30 %	*exp-3*	*exp-12*	*exp-21*	*exp-30*	*exp-39*
Cosmo-5M (An+Fc)	**data**	*exp-4*	*exp-13*	*exp-22*	*exp-31*	*exp-40*
	data−30 %	*exp-5*	*exp-14*	*exp-23*	*exp-32*	*exp-41*
	data+30 %	*exp-6*	*exp-15*	*exp-24*	*exp-33*	*exp-42*
ECMWF (An+Fc)	**data**	*exp-7*	*exp-16*	*exp-25*	*exp-34*	*exp-43*
	data−30 %	*exp-8*	*exp-17*	*exp-26*	*exp-35*	*exp-44*
	data+30 %	*exp-9*	*exp-18*	*exp-27*	*exp-36*	*exp-45*

Table 3.2: Table of ensemble simulations. Meteorological and ocean models are indicated. River forcing "data" are taken from measurements. "An" means analysis, "Fc" is forecast.

3.2.1.1 Large Scale Ocean Models for Downscaling

GOLFEM was nested in larger scale models, as described in Section 2 of the thesis. Five large scale models were available for nesting.

Adriac is an Adriatic Sea scale forecasting model (Fig. 3.2b) that is going to be operational at Arpae-SIMC (currently pre-operational). It is based on COAWST (Warner et al., 2010), which is a coupled ocean-atmosphere-wave-sediment transport model. In

the realization implemented at Arpae it uses the coupled ocean-wave modules. The ocean part is simulated with the ROMS model (Shchepetkin and McWilliams, 2005) at a resolution of about $1\,km$ and 30 σ-layers. It uses the EmodNET bathymetry ($\sim 250\,m$ resolution) merged with topo-bathymetryc multi-beam measurements along the ER coast ($\sim 5\,m$ resolution along each transect). The Po discharge data are used. Climatology is used for the other 48 Adriatic rivers. Initial and boundary conditions are provided by the Copernicus Marine Environment Monitoring Service (CMEMS) MED-Mediterranean Forecasting System (MFS) model for currents, salinity, temperature and sea level. Tides (eight components: K1, O1, P1, S1, K2, S2, M2 and N2) are given at the Otranto strait, computed by the TPXO model (Egbert and Erofeeva, 2002). The wave part is composed by the SWAN model (Booij et al., 1999) that provides waves height, period and direction. The meteorological forcing is provided by COSMO-2I and COSMO-5M models (Steppeler et al., 2003; COSMO-newsletter, 2004), both running operationally at Arpae-SIMC. It provides each day a hourly 3 days forecast with one spin-up day.

AdriaRoms is the operational model at Arpae based on ROMS. It covers the Adriatic basin (Fig. 3.2b) with an horizontal resolution of about $2\,km$ and 20 σ-layers. The Initial and boundary conditions are provided, as Adriac, by CMEMS MED-MFS. Tides (four components: K1, O1, S2, M2) are computed and provided by TPXO to the boundary at the Otranto strait. The bathymetry is realized from GEBCO dataset. The meteorological forcing is provided by COSMO-5M model. Rivers are the same as those used in Adriac. It provided 3 days hourly forecast with 1 spin-up day.

CMEMS MED-currents (Clementi et al., 2017, 2021) is a coupled hydrodynamic-wave model of the Mediterranean Sea and the adjacent Atlantic area (Fig. 3.2a) running operational in the framework of CMEMS. It is composed by the hydrodynamic model Nucleus for European Modelling of the Ocean (NEMO) version 3.6 (Madec, 2008) and coupled 2-way with the third-generation spectral wave model WaveWatchIII (Tolman, 2009). The horizontal grid is at 1/24° resolution ($\sim 4\,km$) with 141 unevenly vertical z levels. The model is forced by the ECMWF atmospheric fields. The model uses a 3D variational data assimilation scheme (3DVAR Dobricic and Pinardi, 2008) to correct the model output. The sea level anomaly and vertical profiles of temperature

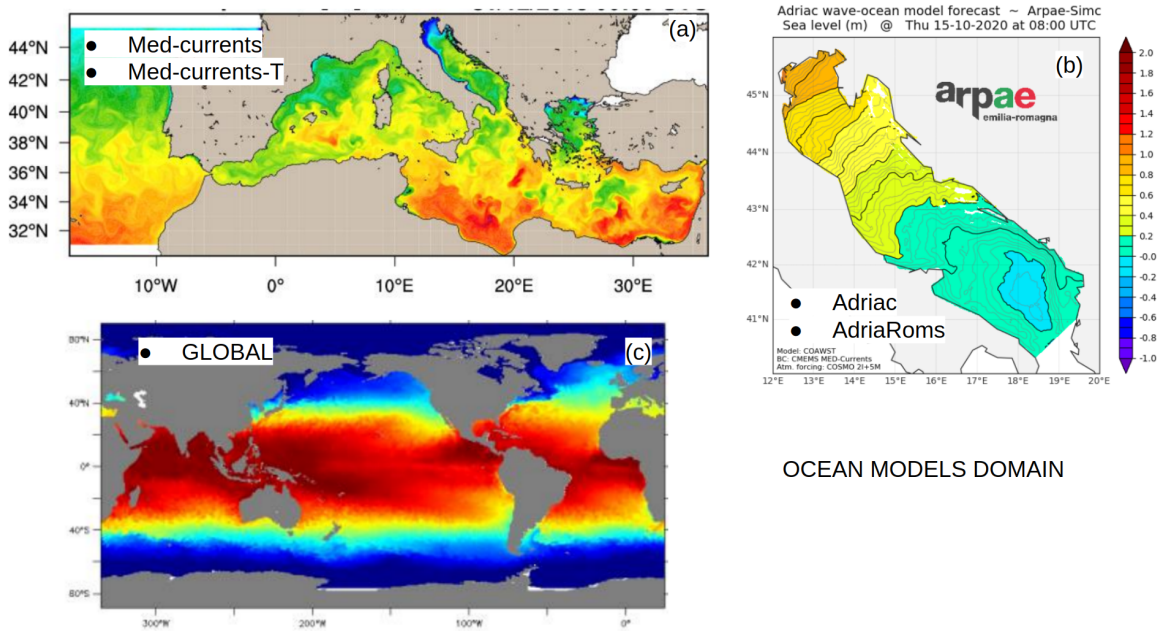

Figure 3.2: Domains of the ocean models used as initial and boundary condition for GOLFEM-EPS. (a) CMEMS Med-currents, (b) Adriac and AdriaRoms and (c) GLOBAL product domain.

and salinity are assimilated from satellite altimetry, ARGO and XBT observations. Satellite SST is assimilated to correct for the heat fluxes. Data assimilation provides the best analysis and initial conditions for the operational 10 days model forecast (hourly output). Recently the eight major tidal constituents were added to the model (hereafter MED-currents-T), including tidal potential for the Mediterranean Sea and providing tidal elevation estimated from FES2014 global tidal model (Carrere et al., 2015) at the Atlantic border. In this work both model versions, with and without tides, were used to force GOLFEM.

The operational CMEMS global ocean analysis and forecast system (hereafter **GLOBAL**; Lellouche et al., 2018) is the global ocean model (Fig. 3.2c) provided by CMEMS. It is based on NEMO (version 3.1) with a horizontal grid resolution of 1/12° ($\sim 8\,km$) and 50 vertical levels up to a depth of $5500\,m$. It uses the SAM-2 data assimilation scheme, based on a reduced-order Kalman filter. It is forced at the surface with the ECMWF meteorological fields. GLOBAL operational system provides every day a 10 days forecast (daily output) and every week it computes the best analysis for the

previous 14 days.

3.2.1.2 Meteorological Forcing

Three operational meteorological products were used as surface forcing.

The **ECMWF** weather forecast used here is based on the deterministic high-resolution global model (ECMWF-IFS; Owens and Hewson, 2018, Fig. 3.3a). This represents the best ECMWF forecast available in the short-term with a resolution of about 12.5 km. It provides a 10 days forecast at 3 hr frequency and the analysis (at 6 hr frequency) are computed using a 4DVAR assimilation scheme to correct the model for observations.

COSMO-5M is an operational meteorological model at Arpae. It is based on the

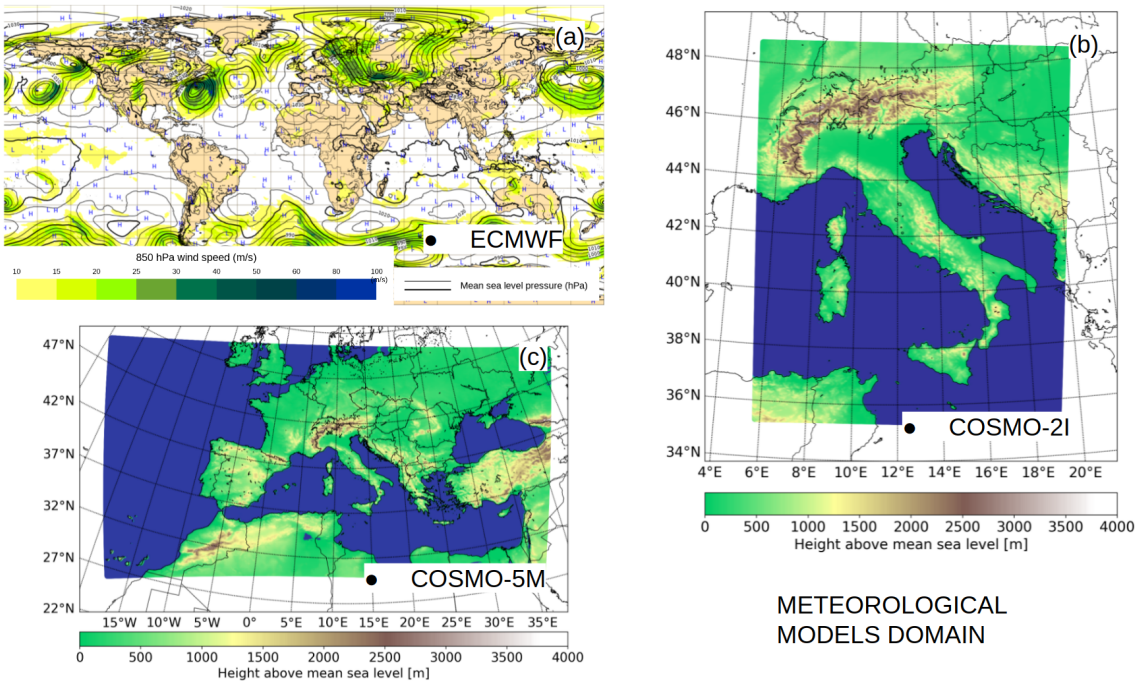

Figure 3.3: Domains of the meteorological models used as surface forcing for GOLFEM-EPS. (a) ECMWF, (b) COSMO-2I and (c) COSMO-5M.

COSMO model (Steppeler et al., 2003) and covers the Mediterranean region (Fig. 3.3c). It has an horizontal resolution of about 5 km and 45 vertical layers. It is initialized by the deterministic analysis of COMet-LETKF (the model used by Italian air force) and take the ECMWF-IFS fields as boundary conditions. It runs twice

per day, at 00 and 12 UTC providing 72 hr forecast (hourly output). **COSMO-2I** is the higher resolution operational weather forecast model at Arpae, covering the Italian domain (Fig. 3.3b). It is nested in COSMO-5M from which it takes boundary conditions. The initial state is computed from KENDA-LETFK system (Schraff et al., 2016). It has a resolution of $\sim$ 2.2 km and 65 vertical layers. It provides a 48 hr forecast (hourly output) and two run per day at 00 and 12 UTC. Both COSMO-5M and COSMO-2I run on the Cineca High Performance Computing (HPC) facilities, with a backup run carried out on the Arpae-SIMC HPC system.

3.2.1.3 Observations

Sea level observations collected at Faro (Fig. 2.1a) are used to assess the model performance. Data are available with 10 minutes frequency. Since the model provides hourly output, the data are averaged to have an hourly dataset. Additionally, the Porto Garibaldi tide gauge station is also available, but its location is at the extreme southern border of the domain considered and it is affected by lateral boundary conditions given to GOLFEM more than the SL predicted by GOLFEM itself. Figure 3.4 shows the sea level observations at Faro (from the end of 2019 to the beginning of 2021), where also the detided time series is shown (orange line). The time of the peak sea level recorded for each event is indicated by the vertical dashed lines. The horizontal dashed lines indicate the 99^{th} percentile of the sea level, in black for the actual data and in red for the detided time series considering all the data available starting from the April 2016. Considering percentiles between 95 and 99 is quite common in extreme value analysis of the sea level (Wahl et al., 2017; Kirezci et al., 2020). In this work the 99^{th} percentile is just took as a reference threshold for the considered events. The same percentiles

Station	99^{th} **SL percentile**	99^{th} **SR percentile**
Faro	0.64 m	0.49 m
P.to Garibaldi	0.70 m	0.53 m

Table 3.3: 99^{th} percentiles of the SL and SR for Faro and Porto Garibaldi stations.

computation was done also for the Porto Garibaldi station, where data are available

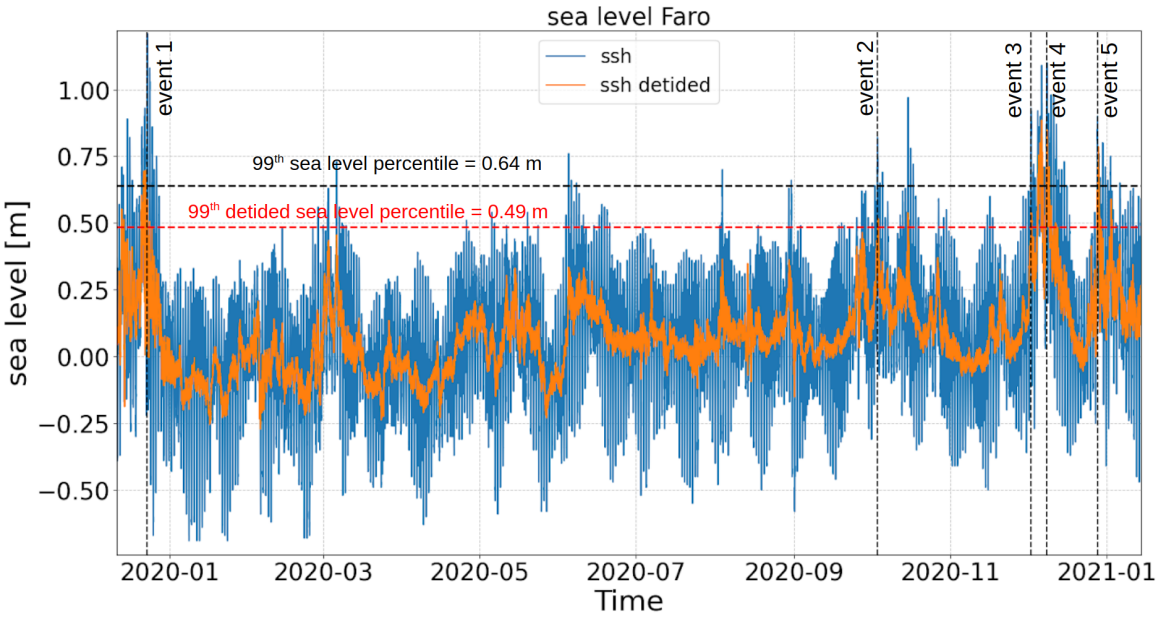

Figure 3.4: Sea level observation (blue) and detided sea level (orange) at Faro (see Fig. 2.1a for reference position). The vertical black dashed lines indicate the peak of the considered events. The horizontal dashed black and red lines indicate the 99th percentile of the sea level and detided sea level respectively.

starting from July 2009. The values found are shown in Table 3.3. Note that all the peak events considered for this work exceed both observed and detided 99^{th} percentile. The detiding procedure (described in appendix A) allows to remove the tidal signal from the time series. The residual signal conserve only the surge contribution, due to local wind, atmospheric pressure and from remote forcing (from open boundary). Hence, the events listed in Table 3.1 have all a non-negligible surge component.

The Po discharge, measured by Arpae at Pontelagoscuro (Fig. 3.5, blue), was used as a lateral boundary condition for simulations with actual rivers data. A 30% of the discharge was added (Fig. 3.5, green) and subtracted (Fig. 3.5, orange) to the actual dataset and used to force the other simulations members (see Table 3.2). The same procedure was applied to the other freshwater sources (pumping plants, Po of Volano and Po of Goro).

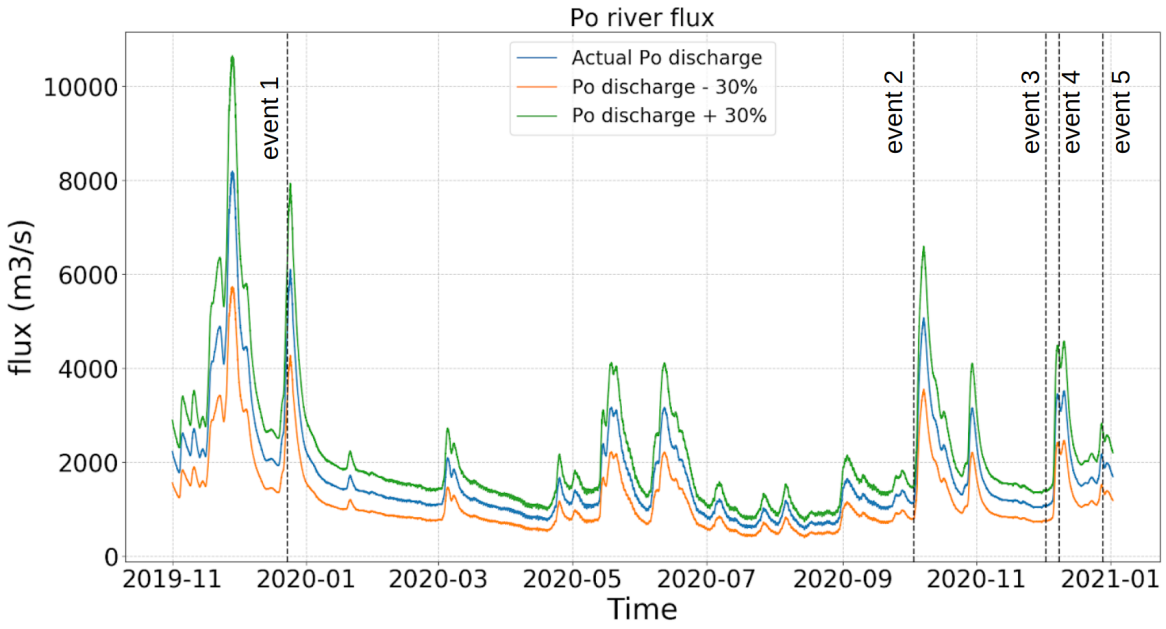

Figure 3.5: Actual discharge rate (blue), discharge -30% (orange) and discharge +30% (green) at Pontelagoscuro. The vertical black dashed lines indicate the peak of the considered events.

3.2.2 Simulations Set-up

This study is thought to be the precursor of a future coastal EPS for the Goro Lagoon. GOLFEM-EPS ran in the domain of Figure 2.1. Among the several grid configurations described in Section 2.3, to simplify the simulations only the *lo-mo* grid was used (Gorino lock and Manufatto open; Section 2.3). The focus of this chapter is on the sea level. Despite the different grid configurations can have strong impacts on the salinity, the effects on sea level are small.

The EPS is composed by 45 members. All the ocean and meteorological models described in the previous sections were used to force the simulations (see the reference Table 3.2). For each meteo-nesting ocean model configurations, three simulations were done: one with the nominal discharge of the Po River, Po of Volano, Po of Goro and the three pumping plants inside the Goro Lagoon and two others are defined by adding and subtracting the 30% of the run-off. The simulations were initialized 1 day before the nominal start of the "forecast", meaning that, 1 day spin-up (Federico et al., 2017) is assumed for the initial condition of a 3 days "forecast" (Fig. 3.6). The simulations

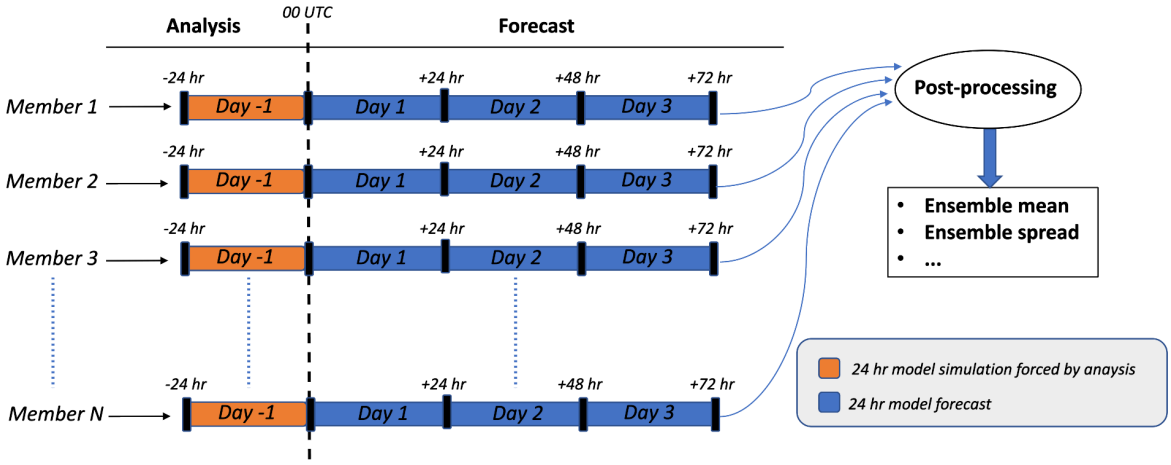

Figure 3.6: Schematic representation of the GOLFEM-EPS. The post-processing indicates a method (based on some metric) applied to build the ensemble mean, ensemble spread and other ensemble variables.

are made in order to have the peak of the event always on the second day of forecast. Adriac and AdriaRoms models do not have an operational data assimilation scheme. Hence, what is called analysis, for Adriac and AdriaRoms model is a simulation forced by meteorological and open ocean lateral boundary analysis.

Figure 3.7 shows the GOLFEM area average Kinetic Energy (KE) for two simulations of the member *exp-1* initialized 3 days and 1 day before the normal start of the forecast, respectively. The KE is initially zero for both simulations (all simulation are initialized with a zero velocity field). It is found that after about 14 hours they reach a very similar KE. This motivates the choice of only one day as spin-up, a reasonable time for such very limited-area domain. It is also well known that the spin-up time decreases with the scale of the implemented computational domain, and 1 day of spin-up is also used by authors dealing with very limited-area models (Gaeta et al., 2016). The CMEMS GLOBAL and Med-currents products are provided without tides. They are computed with the TPXO model and added to the GOLFEM open boundary. The SHYFEM model supports the tidal potential term to account for tidal forces generation inside the computational domain. However, due to the very limited size of the domain, the contribution to sea level of the tidal potential is negligible and was not considered.

Despite the contribution of baroclinic pressure gradient can be important during storm

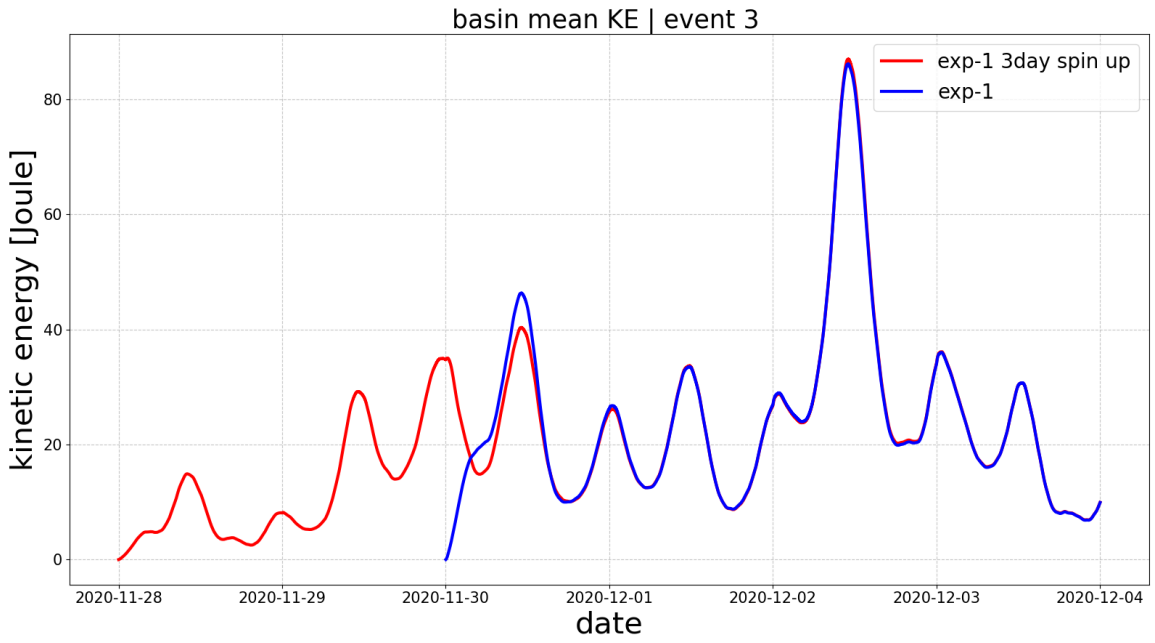

Figure 3.7: Mean basin kinetic energy of *exp-1* considering one (blue) and three (red) days of spin-up. From the plot it is possible to assess that one day is enough for the right initialization of the system.

surge events (Staneva et al., 2016), preliminary simulations have compared the sea level of baroclinic and barotropic runs, highlighting only a negligible difference, probably due to the very small and shallow area considered. However, all the simulations were done fully baroclinic since future studies will focus on temperature and salinity variability. This is in fact a key concept: for SL forecasts the baroclinicity might be site-by-site dependent but the build of a multi-hazard system requires that all processes are considered from the start so incremental improvements will be done keeping into consideration the achievements for SL forecasting.

3.3 Data Analysis and Methods

The SL is the main focus of this study. The surge due to atmospheric forcing, combined with tides and, occasionally with seiches, are analysed and compared with the available observations. An attempt of a superensemble system is done considering a training period to find the best weights to apply to the ensemble members and generate a WEM.

3.3.1 Ensemble Mean Estimation Methodology

There are several methods that can be applied to the members simulations output to make a best estimate of the EM. Part of them are listed in Section 3.1.2 and a detailed discussion can be found in Salighehdar et al. (2017). In this study few of them were tested. Using the notation of Salighehdar et al. (2017), a forecast matrix is defined as $\mathbf{X} = \{x_i^j\}_{(i,j)\in\{1,\dots,T\}\times\{1,\dots,m\}}$ where T and m are respectively the total times and the total number of forecast available in a determined location. So the point x_i^j represents the sea level or surge at time i predicted by forecast member j. The ensemble forecast mean produced by a determined ensemble technique is denoted by a vector $\mathbf{F} = \{F_i\}_i$ of all times i. The observed sea level or surge is denoted by o_i, denoting the observation at time i at a determined location.

The easier method to make an EM is to do a simple average of the ensemble members forecast defined as

$$F_i = \overline{x_i} = \frac{1}{m}\sum_{j=1}^{j} x_i^j \tag{3.1}$$

In this case each member has the same weight. It is a working solution if the performance of each member is similar. However, during extreme events, when usually the forecast uncertainty is greater, could not be the best solution.

Another tested method is the evaluation of the weights of each member based on the performance achieved during a training period. Here the correlation method is tested to compute a weighted EM (WEM). Moreover, only a subset k of the m members can be considered to compute a better average. The first k forecast are chosen based on the performance during the training period. However, the number k of the forecast to retain is a subjective choice. The steps to make the WEM are the following.

1. First the bias between model output and observations during the training period is removed for each member (this step is done also for the simple average)

$$B^j = \frac{1}{t}\sum_{i=1}^{t}\left(x_i^j - o_i\right) \tag{3.2}$$

where B^j is the bias vector and t is the length of the training period.

2. The standard Pearson correlation coefficient, defined in Eq. 2.4, is then computed for the training period for each member denoted by C^j_{o,x^j}. The forecasts are ranked based on correlation and the first k members are retained and used to compute the weights w_j

$$w_j = \frac{C^j_{o,x^j}}{\sum_{j=1}^{k} C^j_{o,x^j}} \tag{3.3}$$

3. eventually the WEM is computed as the weighted average of the selected forecasts

$$F_i = \sum_{j=1}^{k} w_j \left(x_i^j - B^j\right) \tag{3.4}$$

3.3.2 Evaluation Tools

The accuracy of the members forecasts, EM and WEM are evaluated computing correlation and RMSE as defined in Eq. 2.4 and 2.6 for both SL and SR. The RMSE is evaluated against the ensemble spread computed as the root mean square of the ensemble variance. For sufficiently large ensemble size the following equation should be approximately verified (Fortin et al., 2014)

$$RMSE \approx \sqrt{\frac{1}{T}\sum_{t=1}^{T} s_t^2} = \left(\overline{s_t^2}\right)^{1/2} \tag{3.5}$$

where s^2 indicates the variance of the ensemble.

Taylor diagrams (Taylor, 2001) are produced for chosen events, providing an evaluation of the models performances in terms of correlation, standard deviation (σ) and CRMSE (centered root mean square error) defined as

$$CRMSE = \sqrt{\frac{1}{T}\sum_{t=1}^{T} \left(f_t - \overline{f}\right) - \left(o_t - \overline{o}\right)} \tag{3.6}$$

3.4 Results

The results for the five events are analysed with the methods described above. The focus will be in the performance of GOLFEM-EPS in foreseen SR and SL. The uncertainty due to each forcing will be assessed. Some consideration on the main sources of uncertainty and on the importance of the tidal signal will be discussed.

3.4.1 Simulated Sea Level Analysis

Here the EM and WEM forecast is analysed for both SL and SR. The SR is computed for all the model outputs and for observations applying the Fourier transform tidal filter described in appendix A. The first and last 5 hours of the time series are removed from every computation, to avoid borders effects.

The total SL and SR are shown for event 2 (Fig. 3.8a and b), 3 (Fig. 3.8c and d),

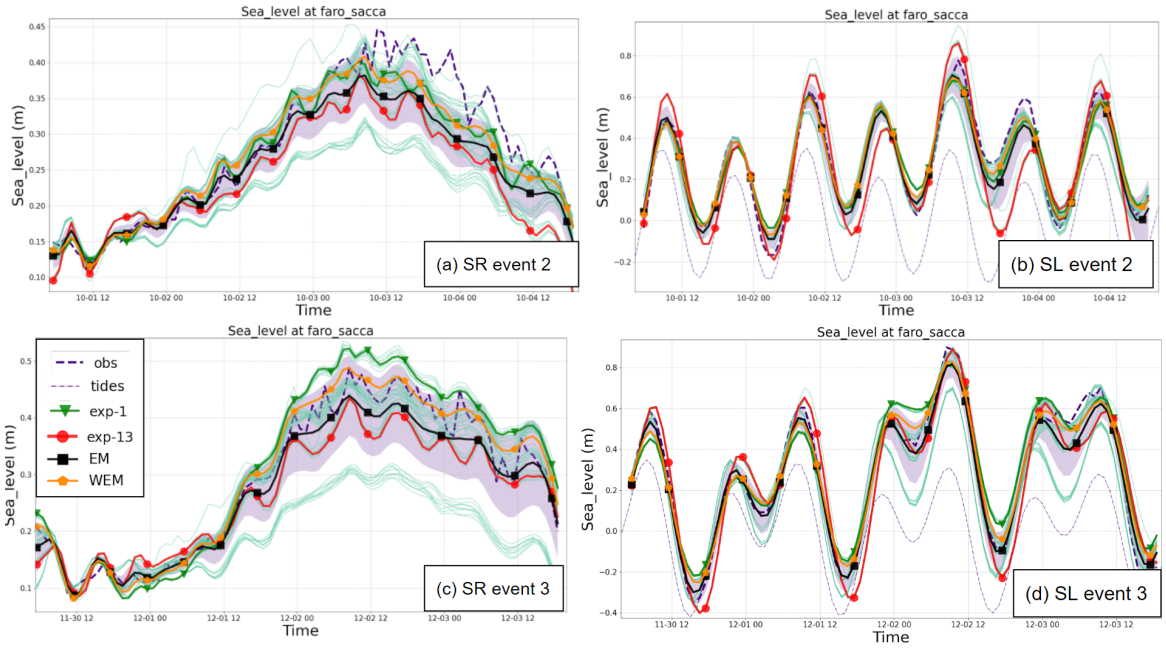

Figure 3.8: SR and total SL forecast comparison at Faro for event 2 (a,b) and event 3 (c,d). The shaded areas are the ensemble spread. Thin blue dashed lines in (a) and (c) are the astronomical tides as computed by TPXO.

4 (Fig. 3.10a and b) and 5 (Fig. 3.10c and d). All the members are shown according to Table 3.2. The member *exp-13*, forced by the current operational models at Arpae (AdriaRoms and COSMO-5M) is shown in thick red line. The thick green line (*exp-1*) is the member forced by the highest resolution models (Adriac and COSMO-2I). These are the deterministic reference models. The black and orange thick lines are the EM and WEM, respectively, where the weights are computed with the procedures explained in Section 3.3.1. The SR shows the maximum amplitude during the second forecast day because of the specific construction of the study case. The ensemble

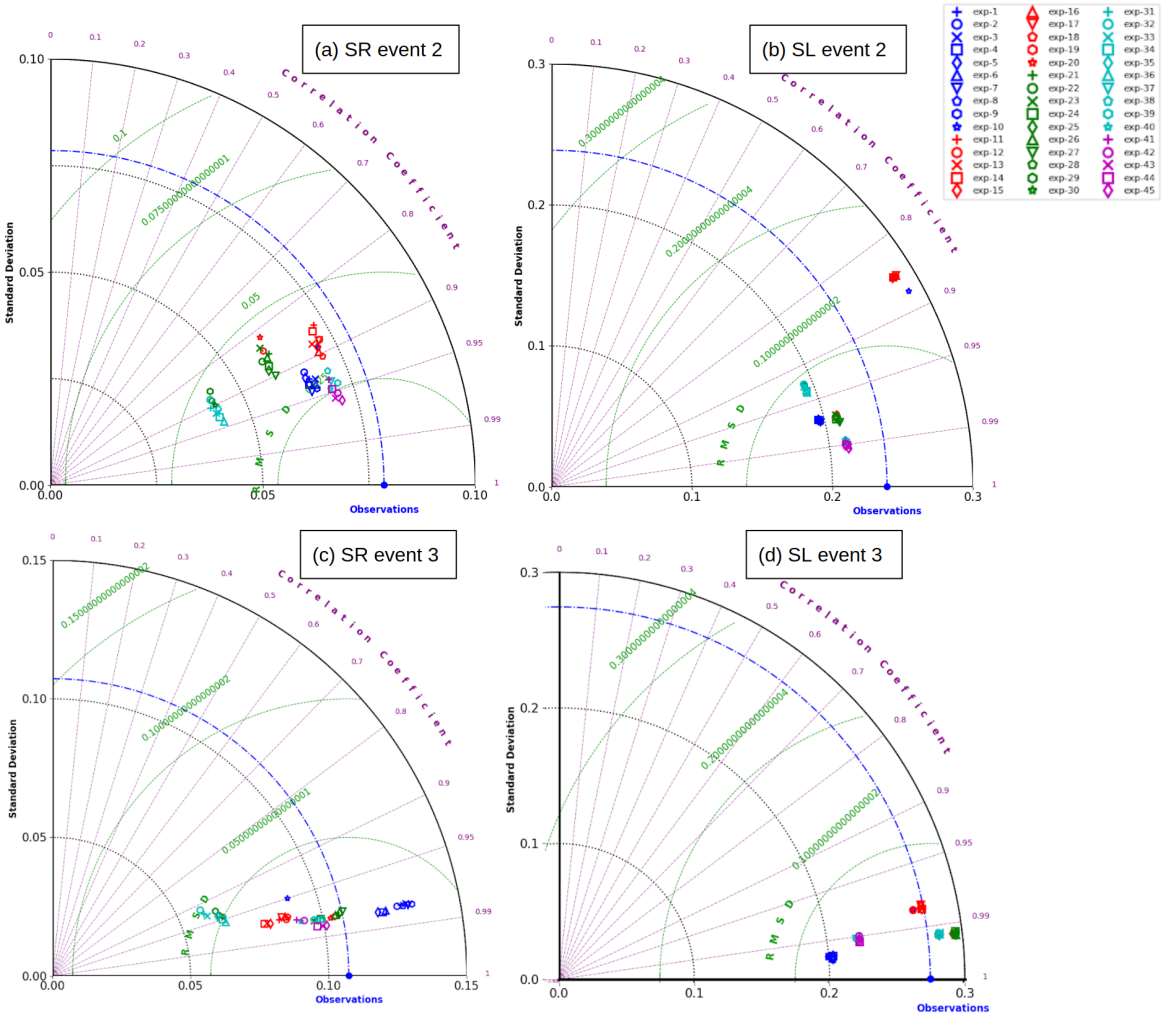

Figure 3.9: Taylor diagrams for SR and total SL for event 2 (a,b) and event 3 (c,d).

spread for SR is maximum at the peak of the event with values of 4.5, 7, 7 and 12 cm for event 2, 3, 4 and 5 respectively. If the total SL is considered, the maximum spread is doubled (at least), suggesting an important role of tides (and occasionally of seiches) in contributing to the sea level uncertainty.

The performances of single members are summarized for each event with Taylor diagrams (Fig. 3.9 and 3.11). The most evident feature is the grouping of members with the same ocean lateral boundary conditions. This becomes even more clear when total SL is considered (Fig. 3.9a,c and 3.11a,c) because of the lateral forcing of tides. If SR is considered (Fig. 3.9b,d and 3.11b,d), for each group there is a dispersion due by the different meteorological forcing and to a lesser extent, to the different river forcing. Therefore, the type of lateral open boundary conditions seems to be the most

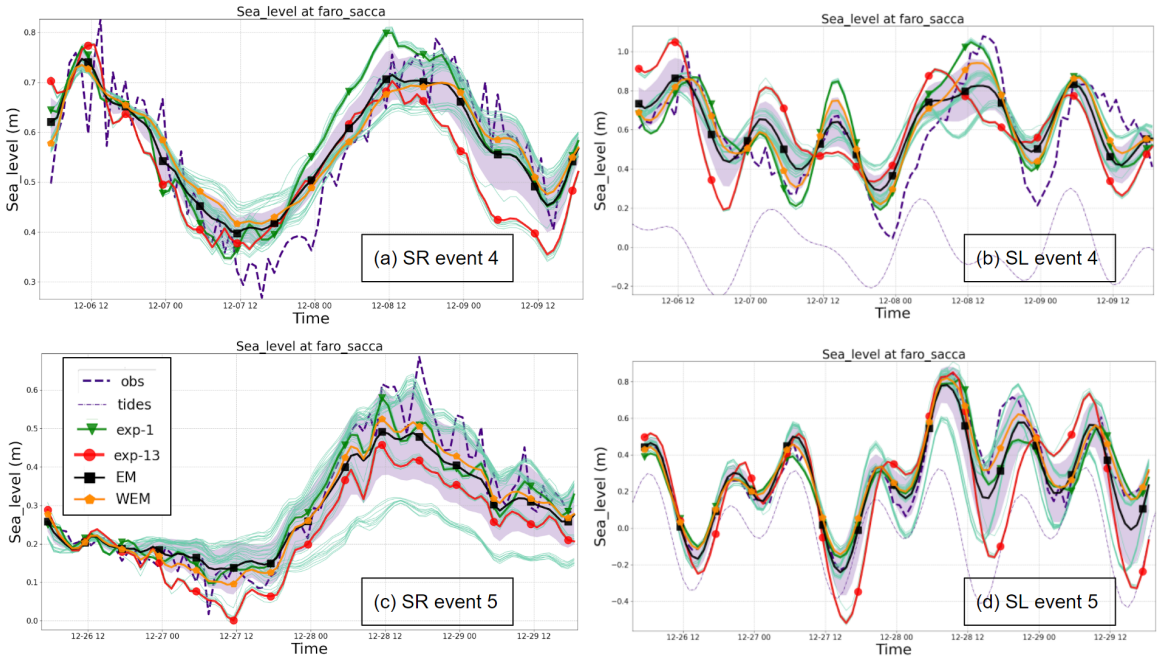

Figure 3.10: SR and total SL forecast comparison at Faro for event 4 (a,b) and event 5 (c,d). The shaded areas are the ensemble spread. Thin blue dashed lines in (a) and (c) are the astronomical tides as computed by TPXO.

impacting source of uncertainty (both for SR and SL), followed by the meteorological forcing and then by the river forcing. The uncertainty due to each forcing will be quantitatively estimated in the next section.

The event 2 was the one that generated an alert from the early warning system of Arpae-SIMC. This can be understood looking at SL in Figure 3.8b. All the members forced by AdriaRoms (from *exp-10* to *exp-18*) exceed the observed sea level from a minimum of 8 to a maximum of 15 cm at about 12:00 of the 3 October 2020. The error can be completely attributed to the tidal forcing since almost all the filtered members correctly catch the SR.

In both event 2 and event 3 the maximum surge co-occurred with the maximum tidal amplitude, producing impacts at the coast. Conversely, event 4 reached the peak during a tidal minimum but the observed sea level reached anyway a high value of 1.1 m. A spectrum analysis of the observed sea level (not shown) revealed that there was a high contribution from the fundamental Adriatic seiche ($\sim 0.25\,m$). If in synchrony with the tidal maximum it would have been a very impacting event, with a possible

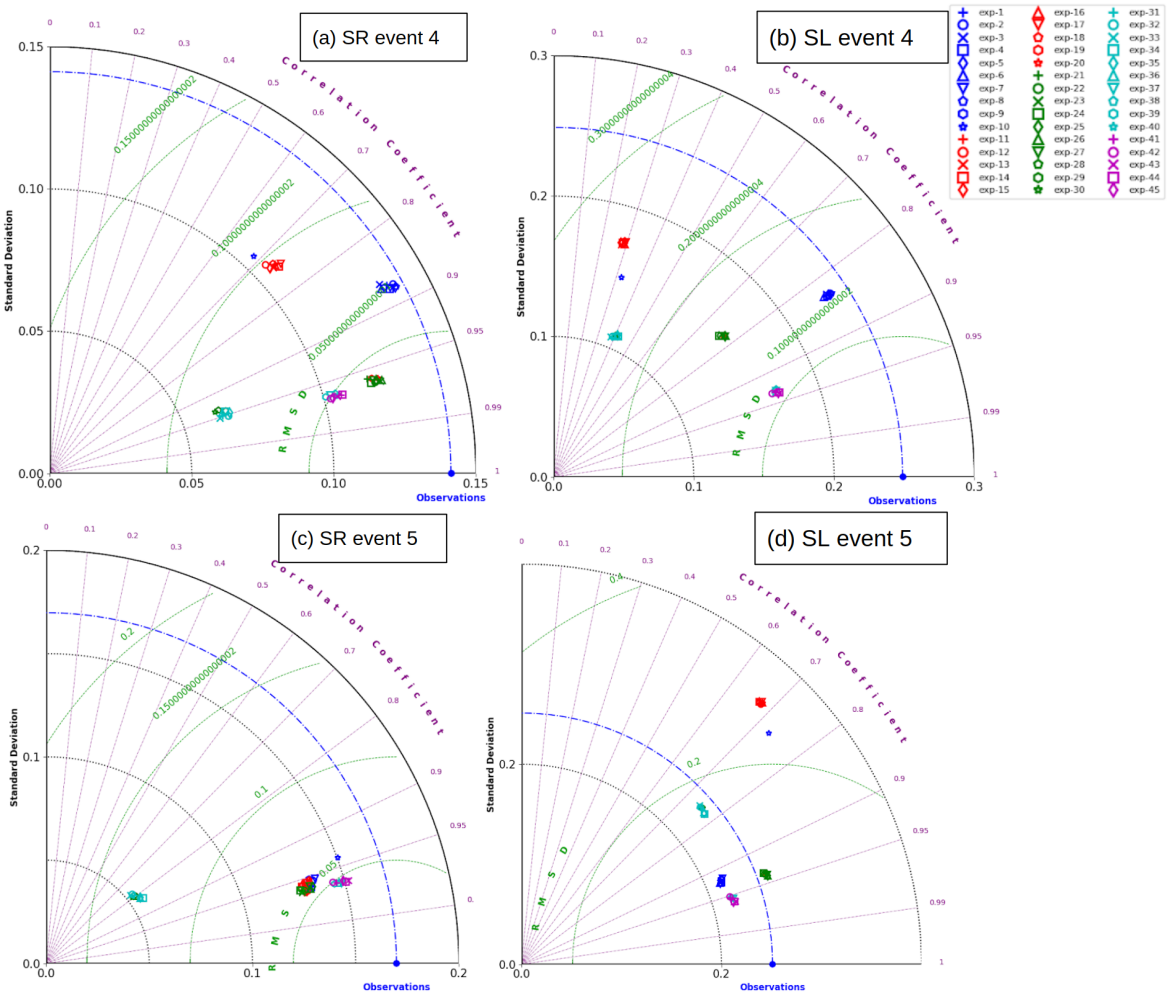

Figure 3.11: Taylor diagrams for SR and total SL for event 4 (a,b) and event 5 (c,d).

maximum SL close to 1.4 m.

Event 1 is the most peculiar since it reveals a decreasing SR during the peak experienced by the SL (Fig. 3.12a and b). Among the events analysed, this event shows the worst performance for most of the ensemble members, with even a negative correlation for the one forced by GLOBAL (Fig. 3.12c and d). However, EM and WEM benefits from error compensation and show satisfactory results in term of SR, although none of the members reproduced the peak of SL occurred on the 23 December 2019 at 07:50. The peak was caused by the fundamental mode of the Adriatic Sea that reached values close to 40 cm and triggered the event in conjunction with tides. The GLOBAL model is not able to reproduce adequately such phenomenon, probably due the low resolution. However, even all the other members forecast a SL much lower than the

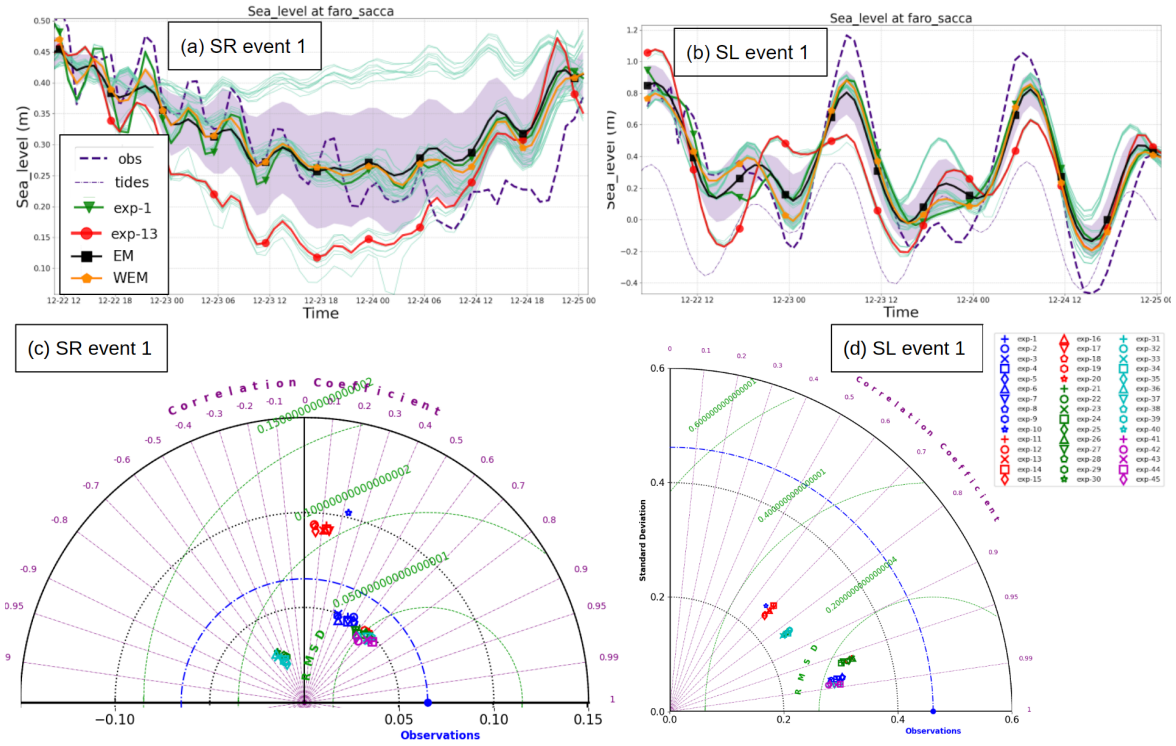

Figure 3.12: SR (a) and SL (b) forecast comparison for event 1. The shaded area in (a) and (b) is the ensemble spread. Taylor diagrams for SR (c) and SL (d) are also shown.

observed revealing some limitations in reproducing possible tide-seiches resonant phenomena. The WEM can be seen for single events in Figure 3.8, 3.10 and 3.12 (a,b). The weights were attributed computing the correlation of all members with observed data, considering one day of spin-up before the start of the forecast (the spin up time, Fig. 3.6). This short period was chosen to have the most updated correlation and a reliable weighting of the members. The members were sorted from the best to the worst and the first 21 members chosen to make the WEM. The Taylor diagrams can provide an overview of the members that were chosen to make the final WEM for each event. In most of the cases members forced with MFS-medcurrent-T (from *exp-37* to *exp-45*) show the best scores (corr. between 0.95 and 0.99; $\sim$ 0.7 for event 1 SR), followed by members forced with Adriac (*exp-1* to *exp-9*; corr. between 0.85 and 0.95; $\sim$ 0.5 for event 1 SR) and MFS-medcurrent (*exp-19* to *exp-27*; corr. between 0.85 and 0.99; $\sim$ 0.7 for event 1 SR). Simulations members forced by AdriaRoms (*exp-10* to *exp-18*) show usually the worst performance (corr. between 0.3 and 0.95; $\sim 0.1 - 0.2$ for event 1 SR) together with the simulations forced with GLOBAL product (*exp-28*

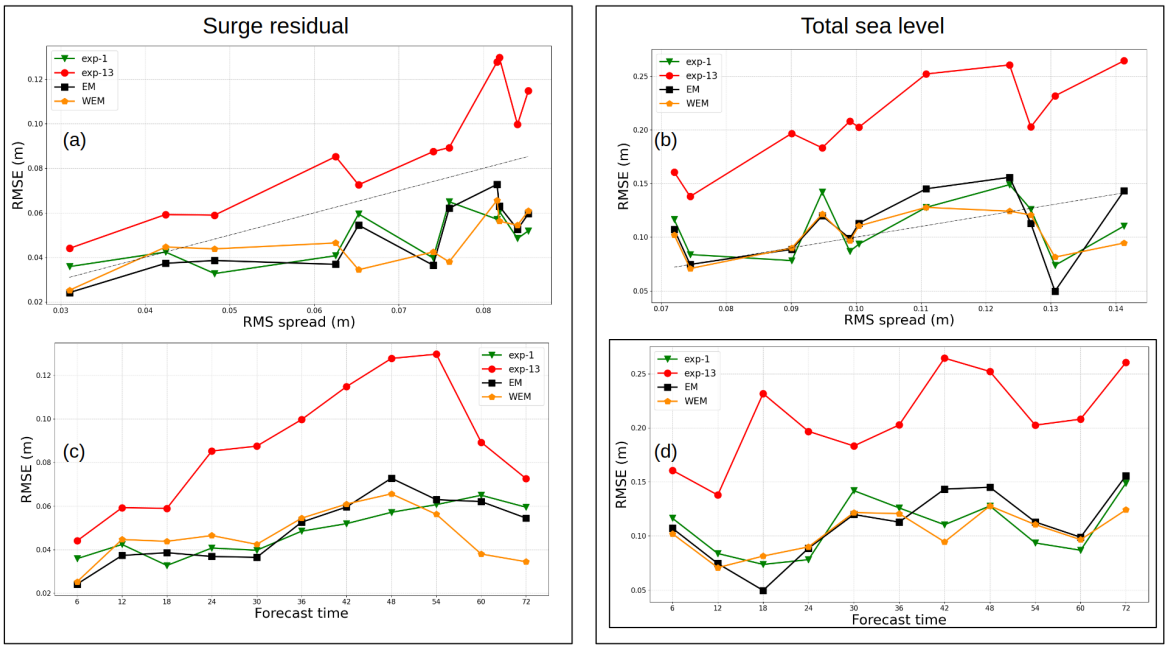

Figure 3.13: RMSE against ensemble spread and forecast time for SR (a,c) and total sea level (b,d). Data are computed aggregating all the events at P.to Garibaldi and Faro station.

to *exp-36*; corr. between 0.4 to 0.9; ~ -0.4 for event 1 SR). Indeed, the low resolution of GLOBAL lead often to low performance and to fall out of the ensemble spread. However, even low performance simulations can be useful in an EPS due to error compensation.

The root mean square error as a function of ensemble spread (Fig. 3.13a and b) and time (Fig. 3.13c and d) is computed for SR and SL, aggregating all the events in both Porto Garibaldi and Faro, considering intervals of 6h. Both EM, WEM and *exp-1* perform much better than *exp-13*. EM and WEM have the tendency to be slightly over-dispersed for spread between 0.05 to 0.08 m with lower than expected RMSE (Fig. 3.13a). The EM and WEM total sea level performance are good (Fig. 3.13b) with a slight over-dispersion at high spread (0.13-0.14 m), probably due to the high uncertainty on open boundary conditions. The SR RMSE error increase with time with a maximum after 48 hr. The *exp-13* seems to perform slightly better at the beginning of the forecast, while after 48 hr both EM and WEM performances are slightly better. The total SL RMSE increase is more linear for all simulations with slightly better performances for the ensemble weighted mean. The RMSE considered for all the forecasts

and all events give 9.8, 5.7, 5.5 and 5 *cm* for *exp-13*, EM, *exp-1* and WEM respectively for SR, while for SL the RMSE is 22.9, 12, 11.5 and 11 *cm*. Although the performance of the WEM is slightly better than *exp-1*, a greater improvement was expected.

3.4.2 Uncertainty Analysis

The spatial distribution of the uncertainty and the relative contribution due to river freshwater input, meteorological forcing and open boundary conditions is assessed. For each forcing a subset of the members used in simulations was considered to isolate forcing contributions to the sea level uncertainty (*i.e.*, the ensemble spread). The maximum uncertainty is computed considering the moment of maximum spread extension, *i.e.*, often at the peak of each event. However, the peak of the SR and of SL may not occur at the same time due to the strong influence of the tidal signal. Here, the uncertainty for river, meteorological and open boundary forcing was computed for the SR. Then the tidal filter was inverted to isolate the tidal signal introduced in GOLFEM-EPS by the different ocean models and the uncertainty associated with tides was computed. However, it is worth to stress that for MFS-medcurrent and GLOBAL boundary conditions, the tides are the one computed by TPXO.
The uncertainty linked to river forcing was evaluated considering simulations where the river discharge was the only different forcing (*e.g.*, *exp-1*, *exp-2* and *exp-3*; *exp-19*, *exp-20*, *exp-21*; ...). Once the spread was found for each of the 15 triplets of simulations, the mean spread was computed. The same methodology was applied to each event and the mean spread among all events was computed. A similar approach was designed to assess the uncertainty connected to meteorological forcing and boundary conditions.

Apart the rivers themselves, where the spread can reach values of 50-60 *cm*, the river run-off has a small influence on the sea level uncertainty (Fig. 3.14a) which remains confined along the coast and lagoons (Goro and Scardovari lagoons), south to the main Po River mouth, where maximum spread values between 3 and 4 *mm* are reached. At the rivers' mouth the spread quickly decreases without seriously affecting the coastal

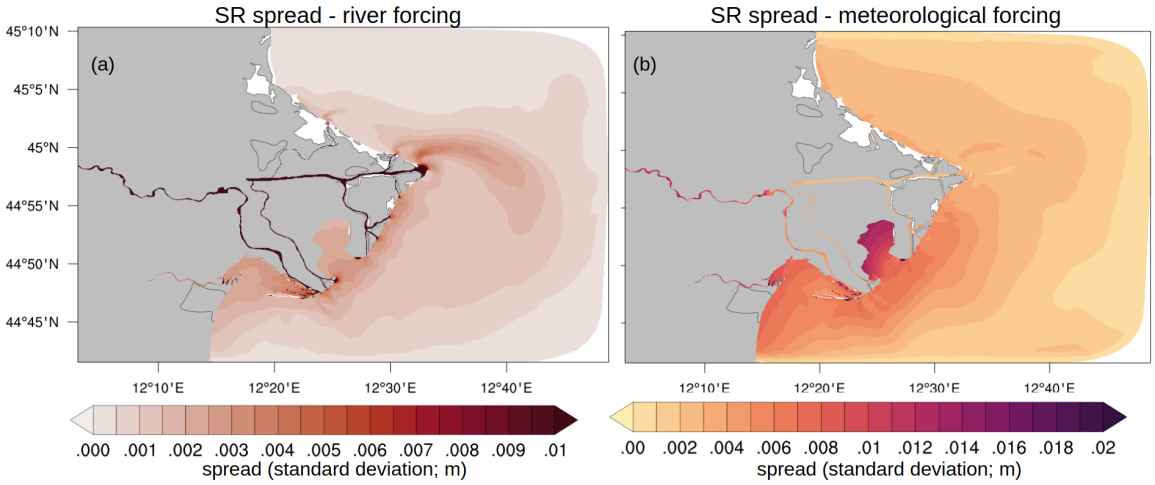

Figure 3.14: Spread due to differential river (a) and meteorological forcing (b). Data are computed aggregating all the events.

areas.

The dominant SE and NE winds during storm surge events, generate a wind set-up with maximum amplitude at the coast and in lagoons (and in rivers), where also the maximum uncertainty is found, with values between 1 and 3 cm (Fig. 3.14b). Despite the winds are one of the main forcing contributing to uncertainties in sea level forecast, the low values found here are a consequence of the small size of the domain. Due to the dominant SE wind in the chosen events the spread is maximum south the main Po mouth with a high variability inside the lagoons. Indeed, in the Goro Lagoon the spread ranges between few mm in the SE part to about 2 cm in the NW area.

The uncertainty due to boundary conditions is clearly dominant (Fig. 3.15a and b), exceeding by one order of magnitude the spread due to the meteorological forcing and two order of magnitudes the one due to the river forcing. In this case no bias correction was applied to the sea level field. The filtered sea level spread (Fig. 3.15a) is almost uniform over the entire domain with values between 12 and 13 cm. The tidal signal extracted inverting the filtering procedure, reveals that the contribution of tides to the sea level uncertainty is of the same order of filtered boundary conditions (Fig. 3.15b), with slightly smaller values between 9 and 10 cm. In order to avoid tidal uncertainty it would be possible, in principle, to filter out tides from parent models and then add the barotropic astronomical tides from tidal models (*e.g.*, TPXO, FES2014).

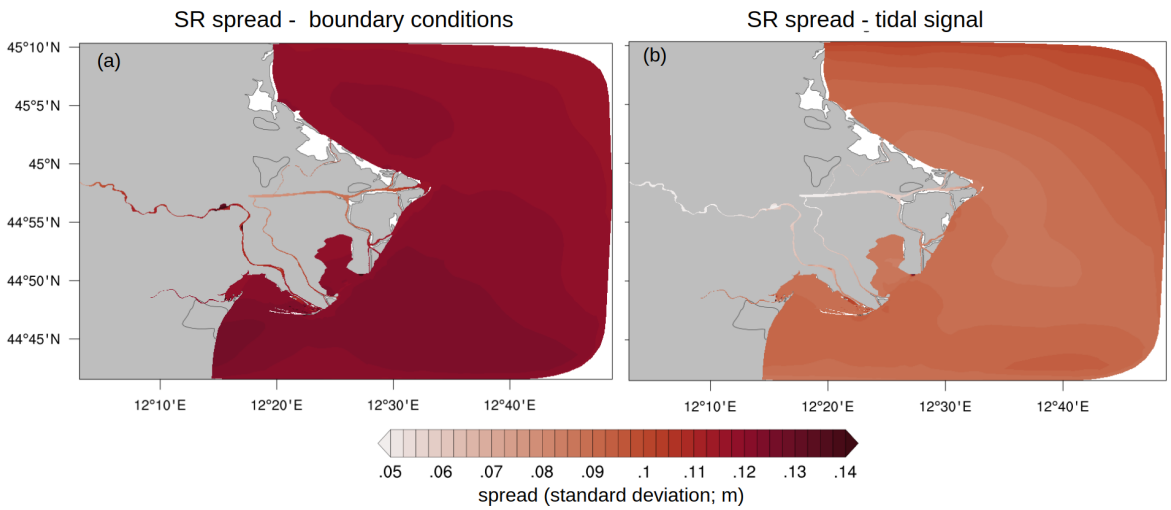

Figure 3.15: SL Spread due to different boundary conditions (a) and tidal signal (b). Data are computed aggregating all the events.

However, tides are modulated by the Adriatic Sea bathymetry and it is hard to expect that external large scale barotropic model would have the required accuracy.
The uncertainty analysis shows a predominant impact of the boundary conditions over the other forcing. A subset of 5 members considering only different boundary conditions, *e.g.*, *exp-1*, *exp-10*, *exp-19*, *exp-28* and *exp-37*, would be enough to reproduce most of the variability that is found with 45 members. This suggests that both for computational efficiency and system performance, storm surge EPS implemented in small domains, should focus on the boundary conditions, both if generated with a perturbation method or if taken from different ocean models.

3.5 Concluding Remarks

A coastal EPS was designed and developed for the Goro Lagoon (GOLFEM-EPS) using a baroclinic very high-resolution unstructured grid model. The EPS is composed of 45 members produced by model simulations done with different meteorological forcing, initial and lateral boundary conditions nesting coarser resolution ocean models and perturbations to the river discharge values. Each simulation uses one day spin-up and a "forecast" lead time of 3 days. A post-processing ensemble mean (EM) procedure is done and a weighted ensemble mean (WEM) methodology is tested based on the

performance of the members during the spin-up period considered to be equivalent to the training period. The total RMSE of the EM and WEM for the SL is respectively 12 and 11 cm, comparable with the simulation forced by the high-resolution models (*exp-1*) that has a final RMSE of 11.5 cm. Among the 45 members used for the ensemble, it was found that most of the variability can be reached including only members that differ in lateral boundary conditions, hence reducing the number of effective members to 5. Nevertheless, this study provided an estimate of the uncertainty due to different forcing. A perturbation of $\pm 30\,\%$ in the river run off contributes with $3 - 4\,mm$ in the ensemble sea level spread. Meteorological forcing has a greater impact between 1 and 3 cm while boundary conditions (including tides) provide most of the sea level uncertainty between 9 and 13 cm.

The conclusions about the skill of WEM or EM for SL 3 days forecast lead times are probably ultimately connected to the specific model domain size and the specific area dynamics. In order to have a general result for ensemble coastal forecasting, several coastal areas should be tried with the same WEM and EM methodologies. For the Goro Lagoon specifically, different model size domains should be tried and the optimal model domain size should be found in order to obtain a reduced SL forecast error.

Chapter 4

Nature-Based Solutions for Coastal Protection

In this chapter Nature-Based Solutions (NBSs) are investigated through a modelling study using a new domain that integrates all the coastal area of the Emilia-Romagna (ER) region, Shyfem Emilia-Romagna (ShyfER), in the northern Adriatic Sea. An introduction to the hazards and risks in the ER region is provided. The concept of NBS associated with seagrass is also described and the implementation of the seagrass NBS is demonstrated for current climate and future climate scenario conditions.

4.1 Risks for the Emilia-Romagna Coastal Area

Every year multiple hazards threaten the global coastal areas. In the previous chapters the hazards related to eutrophication in lagoons and flooding due to storm surges events were highlighted. In the Adriatic Sea, erosion along the ER coastlines, is also a serious issue that could become even more important as a consequence of climate change conditions that are expected over the next few decades (Gallina et al., 2019). This is primarily due to changes in river runoff that will decrease the sediment loading and thus the natural sources of replenishment for the dominant ER beaches (Milliman et al., 2016; Grottoli et al., 2020).

The ER coastal plain is bounded by the Po River in the northern boundary and by the Apennines in the south, with a total extension of $\sim 130\,km$. It is characterised

by wide areas below the mean sea level (SL) in the northern part (Ravenna and Ferrara provinces), where peaks of $-2/-3\,m$ can be reached, which are partially made up of reclaimed wetlands, where dune ridges are still present and partially active in protecting hinterland from flooding (Perini et al., 2015). The southern portion, which includes the province of Forlì-Cesena and Rimini, has a narrow coastal corridor with a general elevation above the mean SL ($2/3\,m$), where natural dunes almost disappeared due to the exploitation of human resources (*e.g.*, sand for concrete buildings) after the Second World War. The area is micro-tidal with a range of $80-90\,cm$ for spring tides and $30-40\,cm$ for neap tides (Harley et al., 2012). Waves are generally of low energy with a 91 % significant wave height $H_{sig} < 1.25\,m$ (Ciavola et al., 2007). However, when the 1 year return period significant wave height is considered, $H_{sig} = 3.3\,m$ (Armaroli et al., 2009) was associated prevalently with Bora wind weather conditions from north-eastern sectors.

Several morphodynamics factors make the shore and back shore unstable. The problem of land subsidence and the rise in SL, as a result of the climate change will increase shoreline instability even more. Land subsidence is a natural process, and a

RCP	ER coast (m)	Adriatic (m)	Mediterranean (m)	Global (m)
2.6	0.30 ± 0.07	0.31 ± 0.01	0.36 ± 0.02	0.38 ± 0.15
4.5	0.34 ± 0.09	0.37 ± 0.01	0.42 ± 0.03	0.45 ± 0.16
6.0	0.33 ± 0.08	0.36 ± 0.02	0.42 ± 0.03	0.47 ± 0.16
8.5	0.45 ± 0.12	0.48 ± 0.02	0.57 ± 0.03	0.60 ± 0.19

Table 4.1: Mean SL predicted for 2081-2100 compared to 1986-2005, according to the four IPCC AR5 RCPs. The Adriatic and Mediterranean values are averaged across these seas. Source: Perini et al. (2017).

consequence of the downward settling of sediment transported by rivers, which is very common in alluvial plains. The entire ER coast is part of the Po Valley, which is the biggest alluvial plain in Italy, and is naturally subjected to subsidence in the order of $2-3\,mm/year$ (Gambolati and Teatini, 1998). However, the strong anthropization of

the ER coast, after the Second World War, led to a drastic increase in subsidence with peaks of 110 $mm/year$ between 1972 and 1973 due primarily to groundwater pumping and gas resource exploitation from in- and off-shore reservoirs (Teatini et al., 2005). The consequences of the fast rate of subsidence led local authorities to decrease the exploitation of resources in order to reduce its impact, which was also already damaging buildings. From recent integrated Synthetic Aperture Radar (SAR) interferometry measurements and Global Navigation Satellite System (GNSS) time series, the current subsidence rate is shown to be between 2.5 and 7.5 $mm/year$ (Bitelli et al., 2020), in line with the rates of natural subsidence.

SL rise, associated with climate change is an increasing concern for the scientific community, governments and the public. This is caused primarily by the global warming and the consequent melting of land ice (44.8 %) and by the thermal expansion (38.6 %) of sea water which has a direct impact on the coastal areas (IPCC, 2021, data refer to the 2006-2018 period). Over the last century, tide gauges located across the Adriatic Sea have indicated a regional rate of SL rise of $1.25 \pm 0.04\, mm/year$ (Galassi and Spada, 2015). The SL rise variability in the Adriatic Sea is subjected to the influence of both interannual and interdecadal oscillation (*e.g.*, NAO, AMO, ENSO...) which can temporarily magnify or reduce the amplitude of long-term trends (Tsimplis et al., 2013). According to IPCC AR5 (IPCC, 2013) the SL rise expected for the Adriatic Sea is systematically lower than that of the Mediterranean Sea and the global value (Perini et al., 2017). If the worst IPCC scenario is considered, *i.e.*, RCP 8.5, the SL expected for 2081-2100 with respect to 1986-2005 along the ER coast is $0.45 \pm 0.12\, m$, which is $0.15\, m$ lower than the expected global value of $0.60 \pm 0.19\, m$ (see Table 4.1; Perini et al., 2017). The effect of the Glacial Isostatic Adjustment (GIA) on the SL is only of minor impact in the northern Adriatic Sea, with values not exceeding few fractions of $mm/year$ (Galassi and Spada, 2015). Since GIA induced SL variations evolve over millennial time scales, the future trends (on secular time scales) are not likely to change relatively to the current trends.

The ER coast is very densely populated and since 1945 the urbanization has increased by ~ 400 % in terms of occupied area (Lorito et al., 2010), increasing the risks for the population and infrastructures in terms of sea related hazards.

SE winds (Scirocco) are generally the triggering forcing for storm surge events. Although they are usually not as intense as the NE Bora winds, the Scirocco helps to pile-up water at the northern Adriatic coasts. However, the largest impacts are connected to the Bora wind occurring at the same time of high tides (Pirazzoli, 1981). The *Bora scura* and *Bora chiara* are the types of Bora wind that are common in the northern Adriatic (Umgiesser et al., 2021). The former is characterized by windy and stormy conditions associated with a cyclone centered in southern Italy and an anticyclone over northern Europe. The latter is characterized by a cold, dry and gusty wind, associated with an anticyclone over central and eastern Europe. Both types of wind events may generate large storm surge events, especially affecting the northern Adriatic Sea.

Since 1945, in most Italian rivers, there has been a significant reduction in sediment transport (Billi and Fazzini, 2017). This is caused by human activities such as bed material exploitation, landslide stabilization, dam construction and the exploitation of water resources in the Po Valley for agricultural purposes. Subsidence, in combination with the reduced river sediment discharge from the Po River, is responsible for the widespread coastal erosion, both on short- and long-time scales (Perini and Calabrese, 2010). Both wind-generated waves and coastal currents contribute to coastal erosion. During storm surges events, breaking waves impact the coast, resuspend sediments that are transported by along-shore currents, eventually giving rise, in the case of the ER sandy beach, to a typical accretion/erosion pattern. Considering 1946-2020 most of the impacts were due to erosion (56 %), followed by inundations (21 %) as shown in Figure 4.1. Considering the same period, impacts due to erosion are quite evenly spread along the entire ER coast, while inundations are more frequent in the northern and central part (Perini et al., 2020, figure 4.2).

Traditionally, the protection of coastal areas is approached from an engineering perspective. The entire extension of the ER shoreline is highly artificialied, with several types of coastal defences, emerged and/or submerged longitudinal breakwaters, localized jetties, groynes and sea walls. In addition, artificial nourishments are periodically needed to combat erosion.

There is growing interest in innovative solutions to protect the coasts. One approach

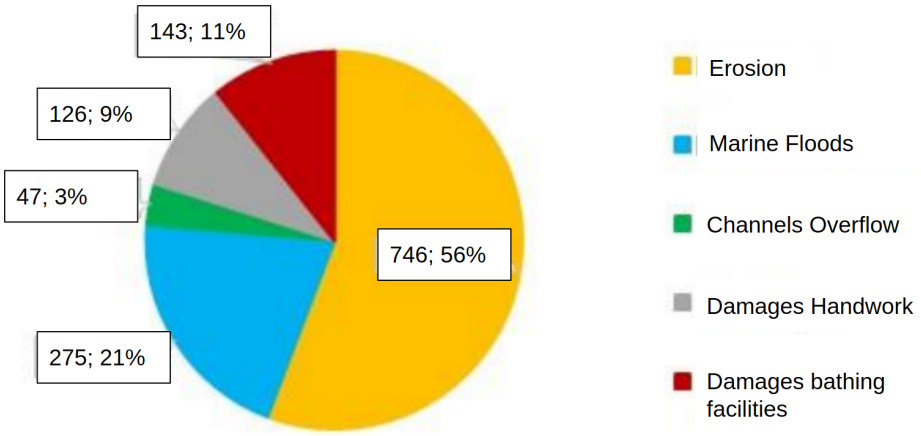

Figure 4.1: Type of impacts along the ER coast from 1946 to 2020. Source: Perini et al. (2020).

is NBSs related to marine seabed vegetation(*e.g.*, seagrass). Seagrass modifies the roughness and structure of the sea bottom thus changing wave amplitude, as shown in many laboratory experiments (Maza et al., 2013). The combination of ecology and engineering seems a promising way toward an integrated and innovative coastal protection methodology. However, in order to be effective, numerical simulations are needed together with the study of the impacts of NBSs. This is now possible due to the growing realism of numerical models that can account for almost all relevant hydrodynamic processes and a realistic coastline geometry.

The following sections assess the effects of seagrass NBS on ER coast protection.

4.2 NBS Approach and Methods

NBSs consist in the design, implementation and application of solutions that are inspired and supported by the natural environment, aimed at mitigating natural hazards and, simultaneously, providing biodiversity and/or ecosystem benefits (Cohen-Shacham et al., 2016). The NBS concept has emerged in the environmental sciences and nature conservation contexts within the last fifteen years or so. NBSs offer solutions aimed at the adaptation and mitigation of climate change impacts, while improving and protecting natural ecosystems and biodiversity. NBSs play a fundamental role in promoting the "transition" from a resources-intensive growth model toward a

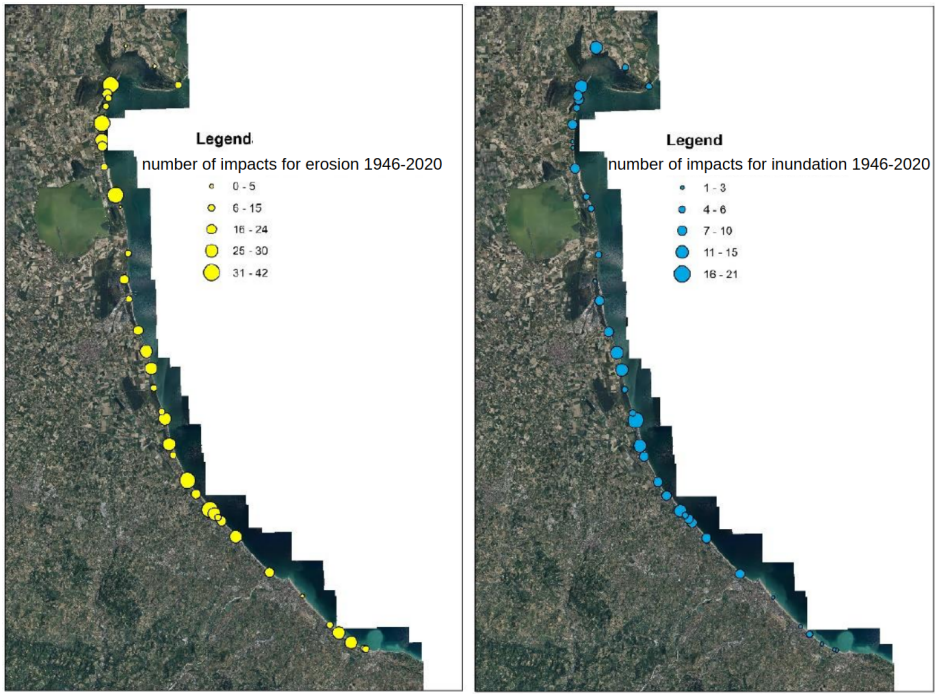

Figure 4.2: Spatial distribution of impacts for erosion (left) and inundation (right) for the period 1946-2020. Source: Perini et al. (2020)

more resources-efficient, integrated and sustainable growth model.

Ecosystem-based initiatives, such as ecological engineering, green/blue infrastructures, ecosystem-based adaptation/mitigation, which are already supported by the European Union, can promote a variety of policy goals. However, each one addresses social, economical and environmental challenges from a distinct perspective. There is currently no integrated approach that considers both human needs, ecosystem and biodiversity conservation at the same time (Nesshöver et al., 2017). Such an integrated approach is one of the major strengths of the NBSs. However, this requires an high degree of interdisciplinarity, involving different expertise and resources which need to be well coordinated and harmonized to reach the maximum effectiveness. The search for innovative solutions in climate change mitigation could collide with social, economic and political aspects, slowing down the "transition" process. Despite the complexity of the interactions between the actors involved, NBSs can provide social innovations and accelerate the transition to sustainability, thanks to the co-design and co-implementations of solutions in line with the NBS philosophy (Nevens et al., 2013).

NBS is an "umbrella" concept covering a range of different approaches (Cohen-Shacham

et al., 2016). Today, NBS holistically integrates both engineering and ecosystem components in its implementation and are currently emboldened in scientific research and practice. The interest in NBS is constantly increasing, both at academic and political levels, with policies already referring to NBS with the aim of further developing synergies among science, politics and practice (Droste et al., 2017).

Seagrass is one of the proposed NBSs which can reduce wave energy and hence the intensity of storm surges (Ondiviela et al., 2014). Seagrass may have important consequences for coastal erosion, since it can reduce the intensity of bottom currents and help sediment trapping, thereby reducing the along-shore sediment transport. The seagrass hazard mitigation and model implementation will be extensively discussed in the next section.

4.3 Seagrass

Seagrasses are rhizomatous angiosperms present in marine and brackish shallow water environments from tropical to temperate regions (Short et al., 2007). Seagrass can form extensive meadows providing key ecosystem services (organic carbon production and export, nutrient cycling, sediment stabilization, biodiversity, etc.; Boscutti et al., 2015). In the present work seagrass was selected as a potential NBS due to its proven role in the coastal protection (Ondiviela et al., 2014). In the last century, there was a large-scale decrease in the seagrass population due to both natural and anthropogenic causes (Waycott et al., 2009). Since seagrass meadows are usually dominated by a single species, they are sensitive to pandemics, such as the "wasting disease" of the 1930s which reduced the *Zostera marina* population by 90 % in the north Atlantic Ocean (Fischer-Piette et al., 1932). Human activities also threaten the seagrass population. Destructive fishing practices, coastal engineering, boat propellers are just some of the activities that lead to direct seagrass losses. Water quality degradation due to an increased discharge of the nutrient load from rivers is also threatening seagrass with the potential of even greater damage. Changes in the sediment load transported by rivers may prevent light reaching the bottom, which is a critical issue for seagrass growth. Most of the Mediterranean Sea bottom between 0 and 40 m is occupied by seagrass

meadows (Ondiviela et al., 2014). Of about 60 species of seagrass in the world, the following seven are found in temperate European and Mediterranean waters: *Halophila decipiens*, *Ruppia marittima*, *Zostera marina*, *Zostera noltii*, *Posidonia oceanica*, *Cymodocea Nodosa* and *Halophila stipulacea*. Of these, only four species are indigenous to the Mediterranean Sea: *Zostera marina*, *Zostera noltii*, *Posidonia oceanica* and *Cymodocea Nodosa*.

The Adriatic Sea shows evidence of all four native species of seagrass (Fig. 4.3)

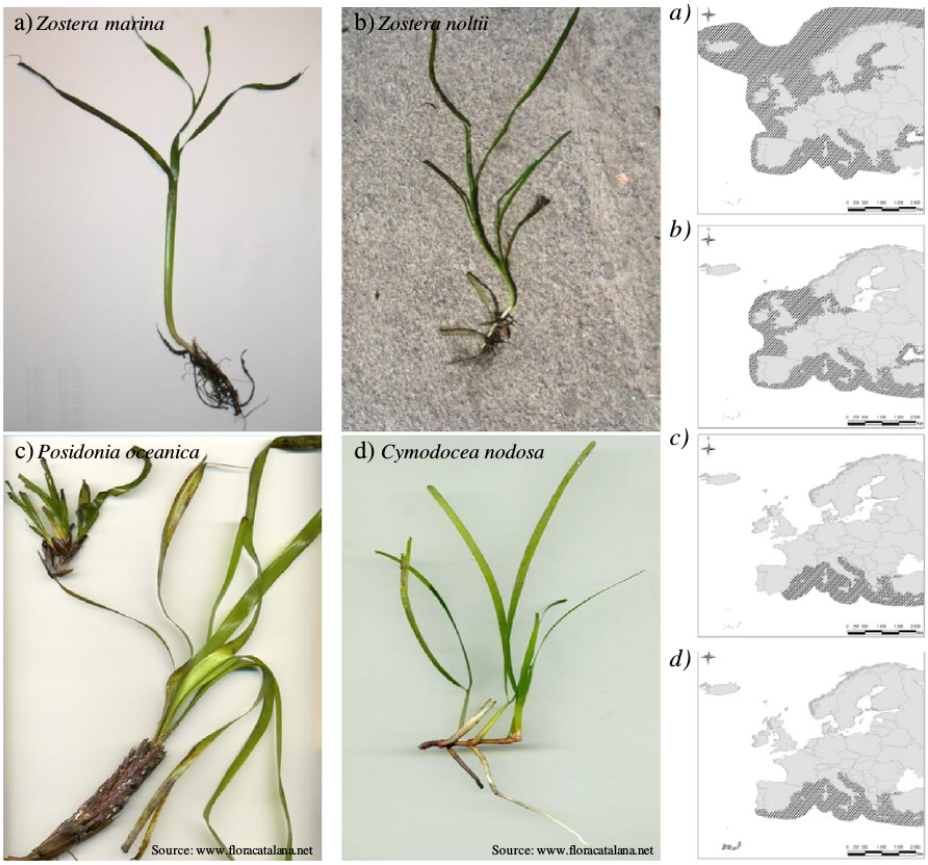

Figure 4.3: The morphology and geographical distribution of Zostera marina, Zostera noltii, Posidonia oceanica and Cymodocea nodosa in European coastal waters. Source: Borum et al. (2004)

although they are not evenly distributed. *Posidonia oceanica* is found in southern Adriatic Sea, along the coast of Puglia (Damiani et al., 1988). In the northern Adriatic Sea, *Zostera marina*, *Zostera noltii* and *Cymodocea Nodosa* are widespread, especially in coastal lagoons such as Grado-Marano and Venice Lagoon (Buia and Marzocchi,

1995; Boscutti et al., 2015). Close to the Po River Delta, there is more uncertainty regarding the presence of seagrass in the past. Sfriso et al. (2016) found no species of seagrass in coastal Po Delta lagoons (excluding the Goro lagoon, which was not analyzed). However, *Ruppia Chirrosa* grows in the Goro lagoon although with a decreasing trend (Piccoli et al., 1991; Pellizzari et al., 2009). Despite a general global trend of seagrass losses, the Adriatic Sea, like other European seas, in the last 50 years has experienced multiple decline and recovery cycles (Danovaro et al., 2020), and in the last few years several projects have focused on seagrass restoration in the Adriatic Sea (Ros et al., 2020; Curiel et al., 2021), aimed at preserving biodiversity and the benefits from seagrass ecosystem services.

The physical influence of seagrass on the flow of the current was first assessed by laboratory experiments (Fonseca et al., 1982), where the effects of seagrass on unidirectional flows was investigated. Further studies showed the effects of seagrass in wave energy reduction (Fonseca and Cahalan, 1992; Verduin and Backhaus, 2000, Fig. 4.4b). In the present work the focus is on the on the flow-vegetation interaction. The structure of the flow can be significantly modified by the presence of seagrass meadows. The underwater vegetation exerts a drag on the flow which may lead to a significant reduction in the velocity within the canopy (Fig. 4.4a), depending, to a certain extent, on the shoot density (Lacy and Wyllie-Echeverria, 2011) and on the flexibility of the plants (Dijkstra and Uittenbogaard, 2010). Fonseca et al. (2019) found that flexibility could be even more important than shoot density in current velocity reduction. Seagrass significantly modifies the vertical turbulent mixing. In the case of submerged vegetation, a new region of turbulence production is generated at the top of the canopy, where a shear-layer develops (*exchange zone*), representing a transition zone between the logarithmic velocity profile that can be found above the canopy (Fig. 4.5b) and the velocity profile within the wakes of the individual canopy elements (*wake zone*), which also represent a secondary turbulence source (Nepf and Vivoni, 2000; Lacy and Wyllie-Echeverria, 2011). The presence of seagrass moves the maximum turbulence generation from the bed to the top of the canopy (Fig. 4.5a and 4.5b). In the case of emergent vegetation (Fig. 4.5c), as can be found in very shallow areas, no shear layer is generated and the mixing in the *wake zone* become the main source of turbulence

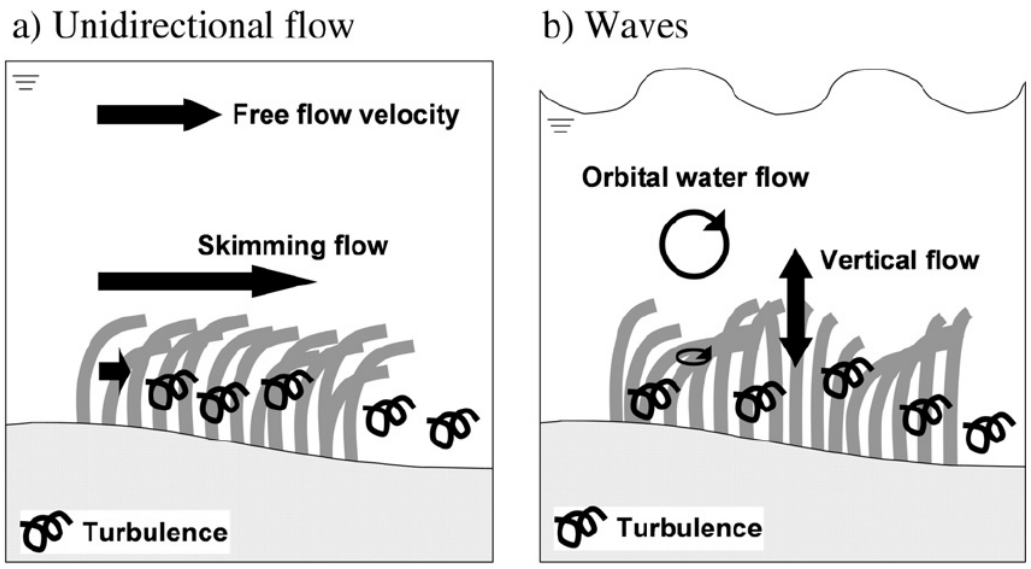

Figure 4.4: Physical processes occurring in the interaction between flexible seagrasses and (a) unidirectional flow (currents) or (b) waves. Source: Ondiviela et al. (2014)

(Nepf and Vivoni, 2000).

4.3.1 Physical Modelling of Seagrass

The representation of flow-vegetation interactions within theoretical and numerical models has been studied at the single plant scale to the regional scale (Morin et al., 2000; Uittenbogaard, 2003; Luhar and Nepf, 2011; Nepf, 2012; Ganthy et al., 2013; Beudin et al., 2017; Zhang et al., 2019). The complexity of vegetation modelling has grown over time. The first attempts to account for vegetation in homogeneous, shallow water models simply involved increasing the bottom friction in areas with vegetation (Morin et al., 2000). Uittenbogaard (2003) focused on the turbulence flow within and above a rigid canopy layer, by introducing a vegetation-induced turbulent term in a $k - \varepsilon$ turbulence closure model (Rodi, 1980). More recent attempts have focused on finding a parametrization of the physical flow-seagrass interaction which can be useful in basin/regional scale numerical ocean models (Beudin et al., 2017; Zhang et al., 2019). Considering horizontal Cartesian coordinates x and y for zonal and meridional directions on the earth surface, respectively, the vegetation acts on the flow as a form

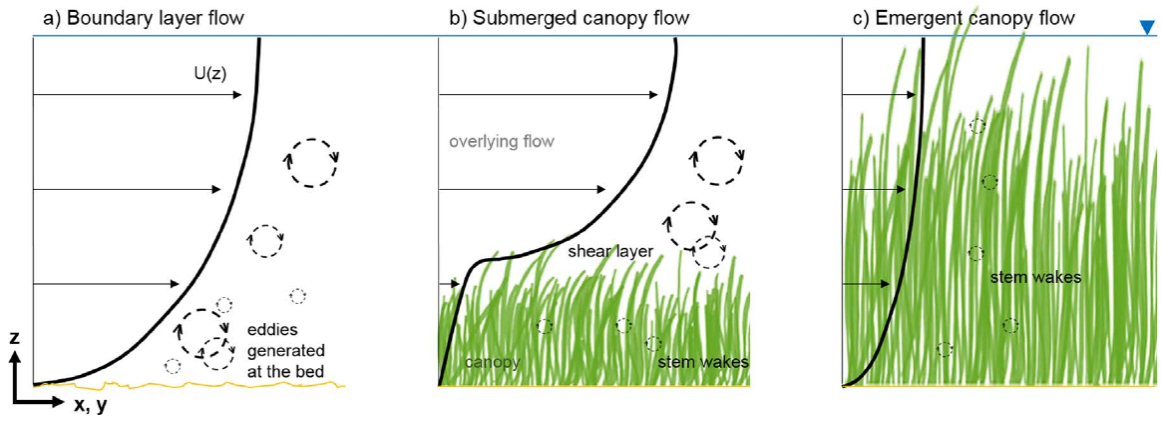

Figure 4.5: The velocity profile and turbulence generation with different structures of vegetation. No vegetation (a), submerged vegetation (b) and emergent vegetation (c). Source: Beudin et al. (2017)

drag which can be approximated using a quadratic formulation:

$$F_{veg,x} = \frac{1}{2} C_{Dv} D_v N_v |\vec{u}| u \tag{4.1}$$

$$F_{veg,y} = \frac{1}{2} C_{Dv} D_v N_v |\vec{u}| v \tag{4.2}$$

where C_{Dv} is a plant drag coefficient, with values that can vary from very small to 3 (Nepf and Vivoni, 2000; Tanino and Nepf, 2008), D_v is the stem diameter, N_v is the vegetation density (number of stems per m^2), u and v are the zonal and meridional components of the velocity and $\vec{u}$ is the velocity vector, respectively (Beudin et al., 2017; Zhang et al., 2019).

Vegetation induced turbulence mixing is accounted for by introducing a new term in the turbulence closure model. Considering a generic two-equation model for turbulent kinetic energy (TKE) and mixing lengths:

$$\frac{\partial k}{\partial t} + \overrightarrow{U} \cdot \nabla k = \frac{\partial}{\partial z}\left(\frac{A_v}{\sigma_k}\frac{\partial k}{\partial z}\right) + P_s + P_v + B - \varepsilon \tag{4.3}$$

$$\frac{\partial \psi}{\partial t} + \overrightarrow{U} \cdot \nabla \psi = \frac{\partial}{\partial z}\left(\frac{A_v}{\sigma_\psi}\frac{\partial \psi}{\partial z}\right) + \frac{\psi}{k}\left(c_{\psi 1} P_s + c_{\psi 4} P_v + c_{\psi 3} B - c_{\psi 2}\psi\right) \tag{4.4}$$

where the definitions are the same of Eq. 1.11 and 1.12 (Umlauf and Burchard, 2003) except for the new $c_{\psi 4}$ parameter and the vegetation term P_v which were added to account for seagrass induced turbulent effects (Rennau et al., 2012). P_v can be expressed as:

$$P_v = \frac{1}{2} C_D b_v N_v |\vec{u}|^3 \tag{4.5}$$

Various assumptions can be made in seagrass modelling. The formulation of Eq. 4.1 and 4.2 consider seagrass as thin cylinders of diameter D_v and height l_v, thus the number of leaves per plants is not considered. In the case of rigid seagrass, the form drag applies from the bottom up to a distance l_v from the bed. However, in the real world, plants modify their structure according to their stiffness, buoyancy and flow characteristics. Luhar and Nepf (2011) proposed a plant-scale model in order to account for seagrass flexibility. This model was implemented by Beudin et al. (2017) in the coupled circulation-waves model COAWST (Warner et al., 2010).

Due to the strong freshwater influence of the Po River along the ER coast, the *Zostera marina* was chosen due to his presence in the northern Adriatic Sea and its ability to survive and grow in environments with low salinity. The physical characteristics of *Zostera marina*, which are necessary to compute the seagrass form drag (Eq. 4.1 and 4.2), were provided by Mazzella et al. (1998):

Seagrass physical parameters			
species	$D_v\,(cm)$	$N_v(m^{-2})$	$l_v(cm)$
Zostera Marina	0.38	277.5	21.3

Table 4.2: Physical parameters of *Zostera marina* needed to compute Eq. 4.1 and 4.2.

4.4 Model Design and Implementation

To account for small-scale coastal processes a very high-resolution model was adopted based on SHYFEM (see Section 1.2). All the simulations in this chapter were performed with a computationally efficient and optimized Message Passing Interface (MPI) based parallel version of SHYFEM (Micaletto et al., 2021) on the ZEUS cluster (Lenovo SD530 biprocessor nodes, for a total of 12.528 cores) hosted by the CMCC SuperComputing Center. The numerical grid includes the ER coastal area and the Po Delta, which are needed to simulate the plume of the river that greatly influences the sea dynamics and the salinity along the ER coast (ShyfER domain, Fig. 4.6). ShyfER has a variable resolution from 2.2 km offshore to a maximum resolution of about 300 m

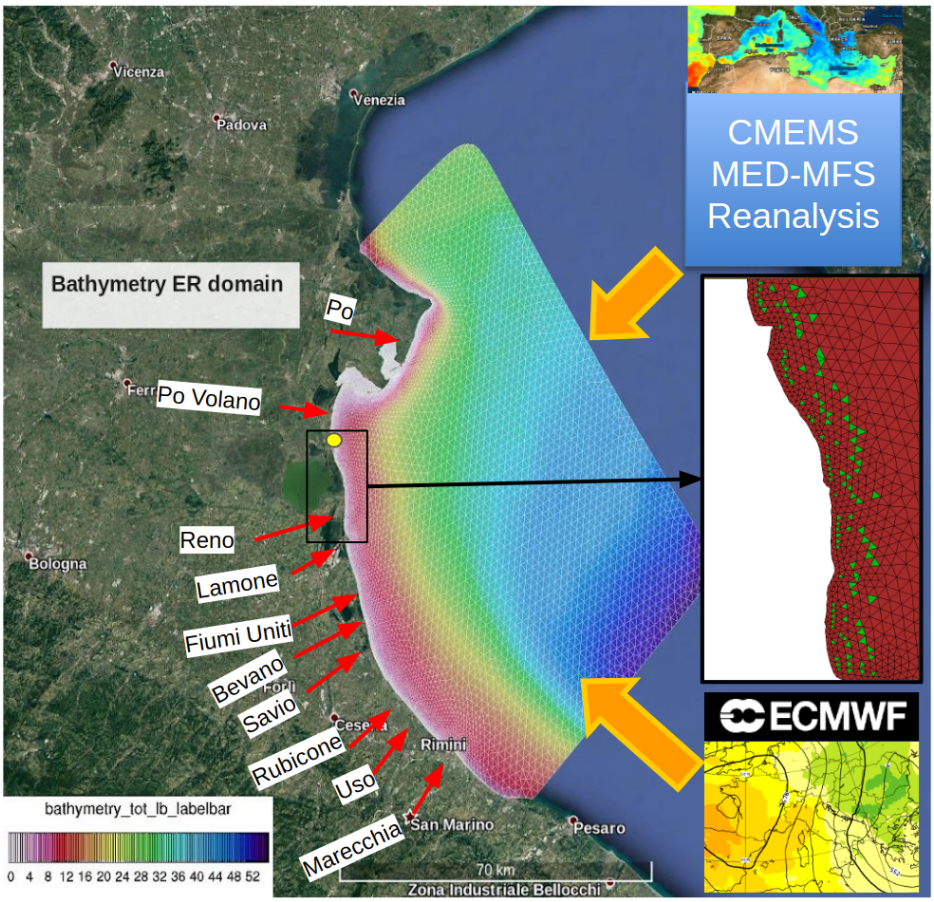

Figure 4.6: Domain of the ER model (ShyfER) with bathymetry. Names and position of the ER rivers are indicated by red arrows. Sources for boundary conditions and atmospheric forcing for the control simulation (ERM-CNT) are indicated on the right. The yellow dot indicates the position of the Porto Garibaldi station.

at the coast and inside the Goro and Scardovari lagoon with a total amount of 15392 elements and 8148 nodes. In the vertical direction there are 33 levels. In the first 10 levels the layer thickness is $1\,m$. Then layer thickness increases to $2\,m$, up to a maximum depth of $56\,m$. A $k-\varepsilon$ turbulence model is used to treat the vertical mixing (Burchard et al., 1999).

4.4.1 Seagrass Implementation in SHYFEM

The seagrass implementation in SHYFEM followed the approach of Zhang et al. (2019) for the momentum equations. Considering a generic layer l the SHYFEM momentum

equations can be written by adding the vegetation form drag as:

$$\frac{\partial U_l}{\partial t} + u_l\frac{\partial U_l}{\partial x} + v_l\frac{\partial U_l}{\partial y} + \int_{z_l}^{z_{l-1}} w\frac{\partial u}{\partial z}dz - fV_l = -gh_l\frac{\partial \zeta}{\partial x} - \frac{gh_l}{\rho_0}\int_{H_l}^{0}\frac{\partial \rho'}{\partial x}dz - \frac{h_l}{\rho_0}\frac{\partial P_a}{\partial x} + \nabla_h\cdot(A_H\nabla_h U_l) + \int_{z_l}^{z_{l-1}}\frac{\partial \tau_{xz}}{\partial z}dz - \int_{z_l}^{z_{l-1}}\mathcal{H}(z_l - z_v)\,F_{veg,x}dz \quad (4.6)$$

$$\frac{\partial V_l}{\partial t} + u_l\frac{\partial V_l}{\partial x} + v_l\frac{\partial V_l}{\partial y} + \int_{z_l}^{z_{l-1}} w\frac{\partial v}{\partial z}dz + fU_l = -gh_l\frac{\partial \zeta}{\partial y} - \frac{gh_l}{\rho_0}\int_{H_l}^{0}\frac{\partial \rho'}{\partial y}dz - \frac{h_l}{\rho_0}\frac{\partial P_a}{\partial y} + \nabla_h\cdot(A_H\nabla_h V_l) + \int_{z_l}^{z_{l-1}}\frac{\partial \tau_{yz}}{\partial z}dz - \int_{z_l}^{z_{l-1}}\mathcal{H}(z_l - z_v)\,F_{veg,y}dz \quad (4.7)$$

where the terms are defined in Section 1.2 except for the last one in the right hand side. $z_v = H - l_v$ is the depth of the top of the canopy layer with H being the total water depth, $F_{veg,x}$ and $F_{veg,y}$ are defined in Eq. 4.1 and 4.2 where $C_{Dv} = 1$ and the other parameters are taken from Table 4.2. $\mathcal{H}()$ is the Heaviside step function, defined as:

$$\mathcal{H}(x) = \begin{cases} 1, x \geq 0 \\ 0, x < 0 \end{cases} \quad (4.8)$$

From the numerical point of view, for a generic layer l, considering the x-momentum Eq. 4.6, the vegetation term is treated implicitly and is linearized following the same procedure that also applies to other non-linear terms (*e.g.*, bottom drag):

$$\frac{1}{2}C_{Dv}D_vN_v\int_{z_l}^{z_{l-1}}\mathcal{H}(z_l - z_v)\,|\vec{u^n}|u^{n+1} \cong \frac{1}{2}C_{Dv}D_vN_v|\vec{u^n}|\int_{z_l}^{z_{l-1}}\mathcal{H}(z_l - z_v)\,u^{n+1} \quad (4.9)$$

where u^n and u^{n+1} are the zonal velocity component at timestep n and $n+1$. Two different cases apply with this approach, depending on whether or not the vegetation cover the full layer thickness. Bearing in mind that for a layer l the vertical integrated horizontal velocity is defined by Eq. 1.3 and considering Eq. 4.9 the vegetation term reads:

$$\frac{1}{2}C_{Dv}D_vN_v|\vec{u^n}|\int_{z_l}^{z_{l-1}}\mathcal{H}(z_l - z_v)\,u^{n+1} = \begin{cases} \frac{1}{h_l}\frac{1}{2}C_{Dv}D_vN_v|\vec{U_l^n}|U_l^{n+1}, & z_v \leq z_{l-1} \\ \frac{z_l - z_v}{h_l^2}\frac{1}{2}C_{Dv}D_vN_v|\vec{U_l^n}|U_l^{n+1}, & z_{l-1} < z_v < z_l \end{cases} \quad (4.10)$$

The same procedure applies to y-momentum equation.

The $k-\varepsilon$ model is modified to account for the turbulence generated within the canopy

layer. A vegetation term is added to the two turbulence equations, as indicated in Eq. 4.3 and 4.4, where for SHYFEM, the $k-\varepsilon$ model requires $\psi = \left(c_\mu^0\right)^3 k^{(3/2)} l^{-1}$ (Umlauf and Burchard, 2003). Adding a vegetation term to the turbulence model, requires a further parameter $c_{\psi 4} = 1.44$. This value was chosen to minimize the impact of the vegetation term on the mixing efficiency, since no data were available for a better calibration (Rennau et al., 2012).

In this specific work, the turbulence due to the vegetation term in Eq. 4.3 and 4.4 is not included since it is much smaller than the one induced by the shear at the top of the canopy (see idealized testcase in next section), which represents the most important contribution of vegetation to the turbulence production.

4.4.2 Idealized Testcase

The effects of the vegetation term on the flow were tested with two specific benchmarks:(i) the first simply using the GOTM model (which is the turbulence model included in SHYFEM, Burchard et al. (1999)) aimed at assessing the role of turbulence induced by vegetation; (ii) the other using SHYFEM in order to assess the contribution of vegetation in a 2-D/3-D environment.

4.4.2.1 First Case: the GOTM One Dimensional Model

The first testcase was performed with the GOTM model (Burchard and Baumert, 1998) in its one-dimensional implementation (SGS-1D). A tidal forcing with a period of $12.42\,h$ (*i.e.*, M2 tidal component) was used as an idealized forcing to generate a barotropic pressure gradient on the water column. No baroclinic effects were considered. A water depth of $5\,m$ was chosen and discretized with 100 vertical levels. A rigid vegetation of $l_v = 21.5\,cm$ height was considered at the bottom. The simulation lasted for three tidal cycles. The same simulation was performed without seagrass (CNT-1D) and the results were compared.

The zonal velocity is shown in Fig. 4.7a for the simulation with no seagrass. If seagrass is added at the bottom, a reduction in the velocity is observed of up to 50 % in the layers occupied by vegetation (Fig. 4.7b) and a shear layer is generated at the

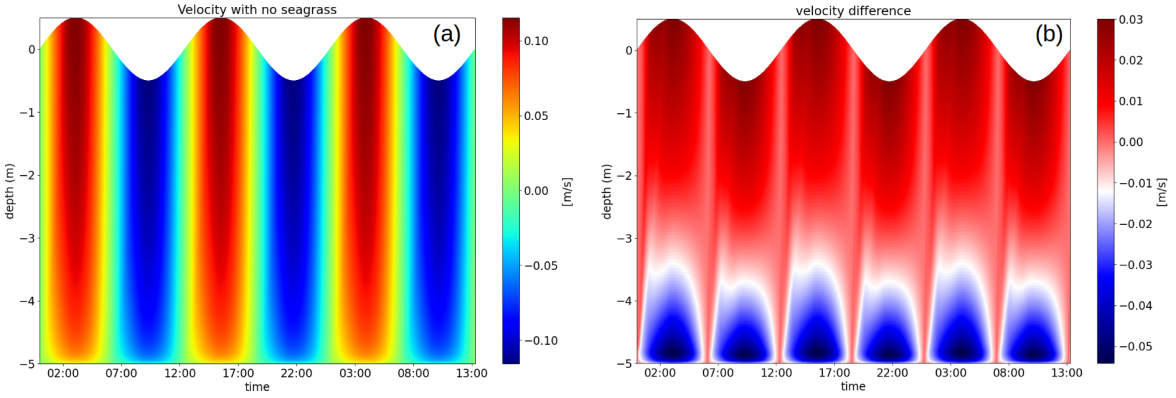

Figure 4.7: On the left (a) zonal velocity in the water column for the CNT-1D simulation. On the right (b) the velocity difference between SGS-1D and CNT-1D.

top of the canopy. The redistribution of momentum in the x direction lead to a slight increase in velocity in the upper layers of SGS-1D experiment. The turbulence produc-

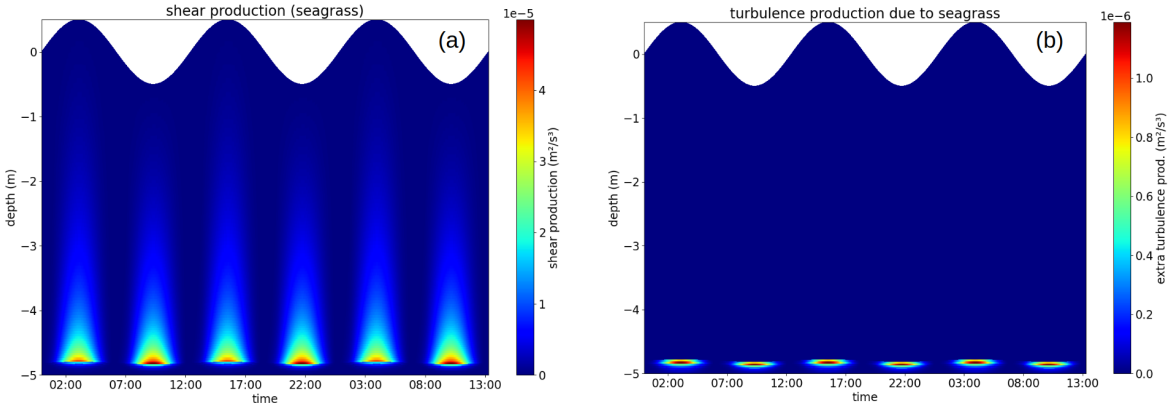

Figure 4.8: The shear turbulence production is shown in (a). The maximum is reached at the top of the canopy layer. The turbulence produced within the wakes of the seagrass is shown on the right (b).

tion due to the shear (P_s), mostly generated at the top of the canopy, is shown in Fig. 4.8a. The extra turbulence production due to vegetation (P_v) is one order of magnitude lower than the shear production (Fig. 4.8). P_v becomes more important for the H/l_v ratio close to one or smaller. The error of neglecting the turbulence production in the vegetation wake can thus be considered negligible for the seagrass configuration treated here and in the next section. A further experiment (not shown), excluding the turbulence in the wakes, confirmed the minor role of P_v when $H/l_v = 23.3$. The eddy

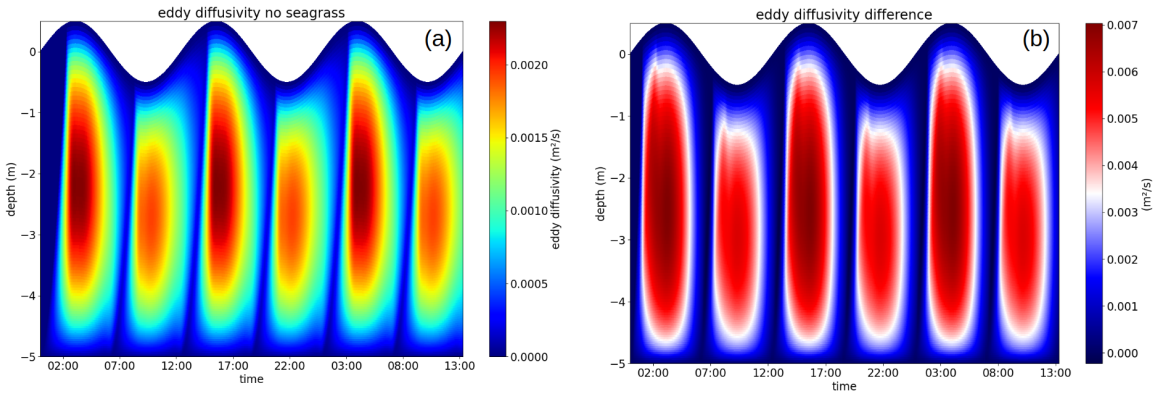

Figure 4.9: The eddy diffusion coefficient for the control experiment without seagrass CNT-1D (a) and the difference (SGS-1D)-(CNT-1d) (b).

diffusion coefficient is greatly enhanced by the presence of seagrass in simulation SGS-1D (Fig. 4.9a and b) both during high and low tides. This represents an important contribution to the vertical mixing along the water column.

4.4.2.2 Second Case: Idealized Seagrass Box in a Flow Field

The implementation of the vegetation module in the SHYFEM model was verified against an idealized testcase carried out by Beudin et al. (2017) (hereafter TC-B). The domain is a square box of $10\,km$ with a central box of $1\,km$ where the seagrass is positioned. The resolution of $100\,m$ is the same in the entire domain. Two different simulations were performed with different vertical discretizations (Table 4.3). The

Domain	Max depth	Number of Layers	Type of Run	Initial T/S
TCSG	$1\,m$	2	Barotropic with viscosity	-
TCSG-cbl	$5\,m$	11	baroclinic	$T = 15°C$ $S = 38psu$

Table 4.3: Table of idealized simulations: TCSG is barotropic run while TCSG-cbl considers baroclinic effects.

TCSG simulation has a maximum depth of $1\,m$ with two layers. No baroclinic effects

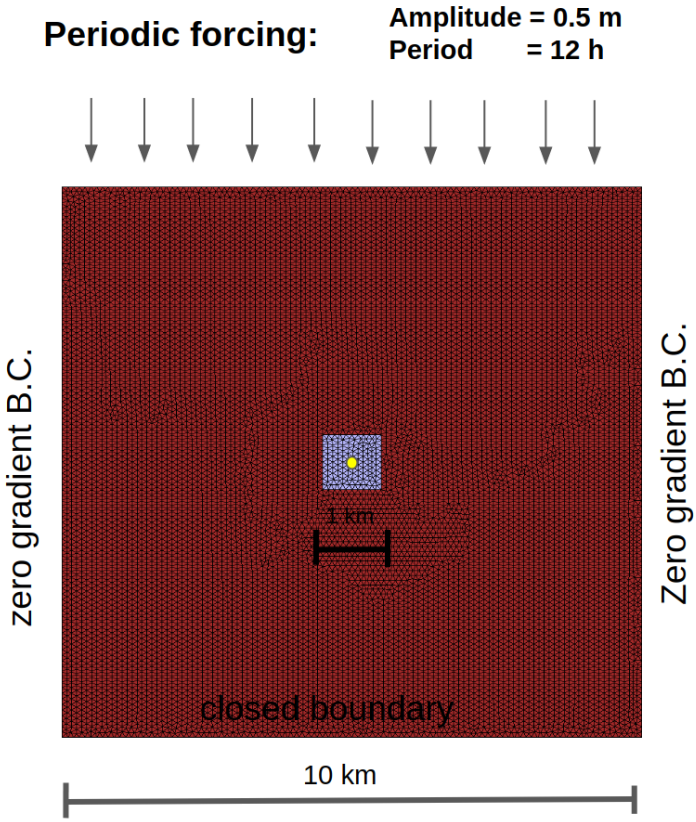

Figure 4.10: Idealized testcase domain. The vegetation patch is indicated by light blue elements at the center of the domain. Boundary conditions are also indicated. The yellow point at the center of the patch indicates the point where the velocity profile is shown in Fig. 4.13.

were added, however a $k-\varepsilon$ turbulence model computed the viscosity in order to control the vertical momentum mixing. This simulation has a similar set-up to the one described in Beudin et al. (2017). The TCSG-cbl was forced in the same way, however it is fully baroclinic with stable stratification and has a greater depth of $5\,m$ with 11 layers. More layers were added at the bottom in order to have a better representation of the canopy layer and test the seagrass implementation. The seagrass parameters for both configurations of the testcases were taken from Beudin et al. (2017), where $l_v = 0.3\,m$, $C_{dv} = 1$, $D_v = 0.3\,cm$ and $N_v = 2500\,stems/m^2$.

The simulations were forced at the northern boundary with an idealized tide of $12\,h$ period and $0.5\,m$ amplitude. The southern boundary is closed. The western and eastern borders have a zero gradient boundary condition for the flow (Fig. 4.10). After

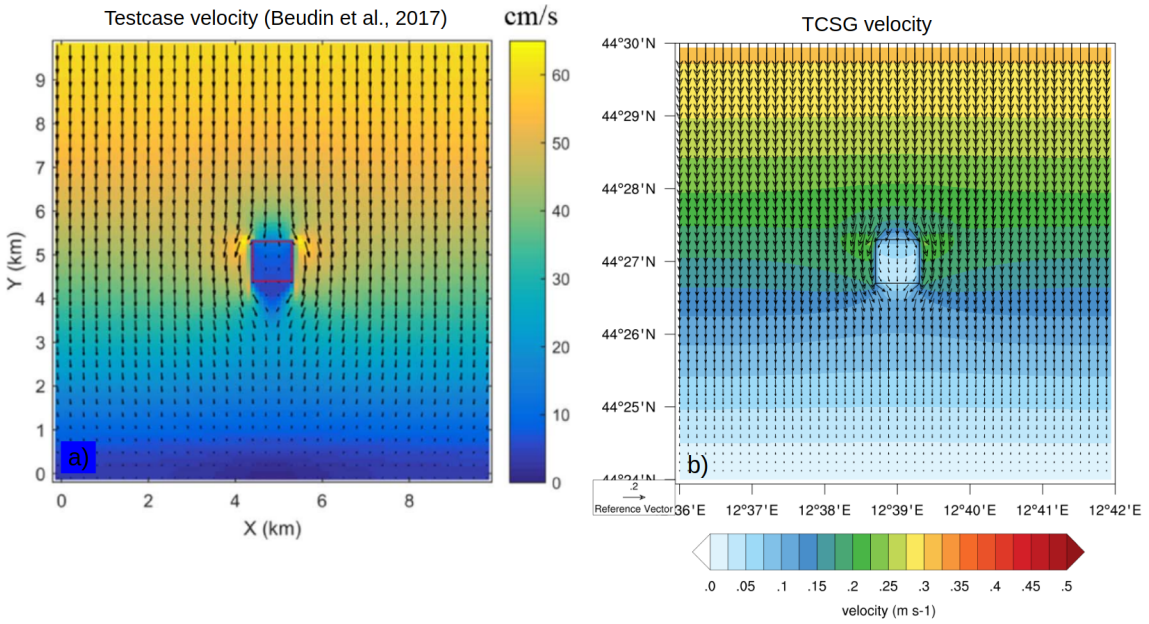

Figure 4.11: Velocity field at peak flood for TC-B (a) and TCSG simulation (b).

a few forcing cycles, the simulation reached a steady state and the velocity field was analyzed. The average depth velocity at the peak flood (*i.e.*, when the effect of seagrass on the flow is maximum) is shown in Figures 4.11a and b for the TC-B and TCSG run, respectively. The maximum amplitude of the velocity field is different in the two simulations, probably due to a different bottom friction implementation between TC-B, where the ROMS model was used and TCSG, where SHYFEM was used. However, in both simulations, the effects of seagrass are similar and the velocity field shows the same modified patterns due to the presence of vegetation. The velocity decrease is maximum inside the patch, where the amplitude is reduced up to 80 % in both simulations, with a smaller decrease in the northern and southern parts of the patch. The flow is deflected toward the western and eastern edges of the patch, where an increase in the velocity of about 40 % is observed.

The difference in water level between the experiment with vegetation and the one without is shown for the peak flood in Fig. 4.12a and b for TC-B and TCSG, respectively. The TCSG simulation well reproduces the result of TC-B (Beudin et al., 2017): the SL decreases by about 18% downstream of the seagrass patch, and increases by about the same amount on the side where the flow impinges on the seagrass. The effect of seagrass is thus complex and has the opposite sign depending on the direction of the

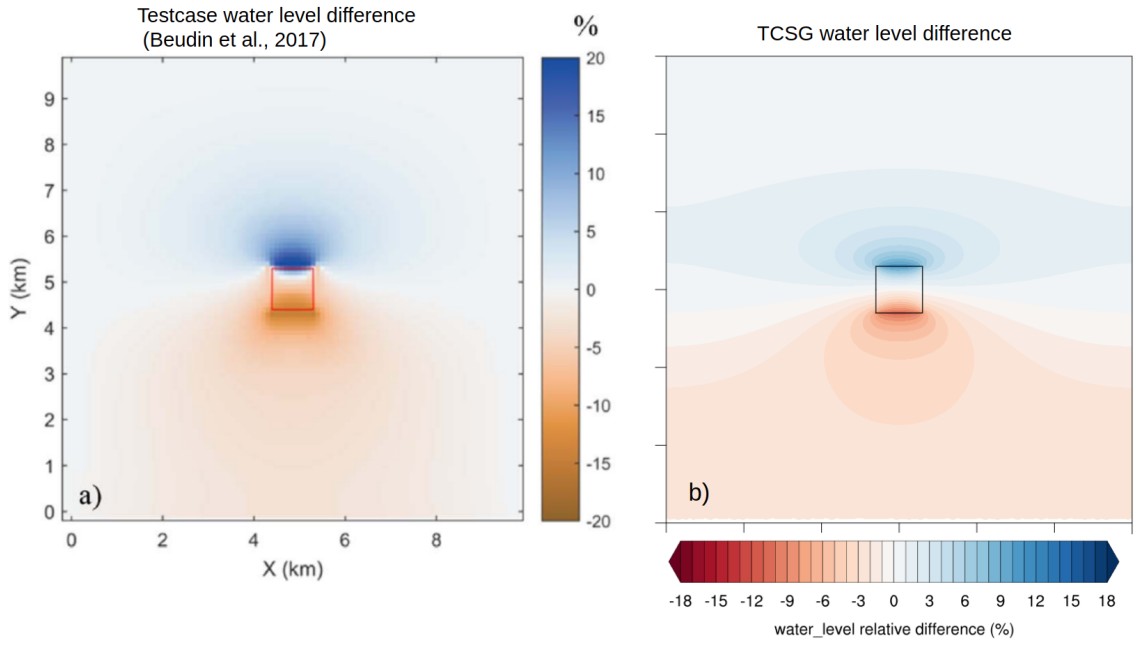

Figure 4.12: Water level difference between vegetation and no-vegetation simulation for TC-B (a) and TCSG simulation (b).

flow field against the seagrass considered as a barrier. The effects of seagrass on the SL decreases very rapidly with the increasing H/l_v ratio. In the TCSG-cbl simulation, where a depth of $5\,m$ is considered, a maximum difference of $5\,\%$ on the SL is observed (not shown). The velocity field shows the same modified pattern with a reduction in velocity of about $75\,\%$ at the bottom and $30\,\%$ at the surface (Fig. 4.13). In this simulation the canopy layer is described by three full layers and well represents the shear layer that is generated at the top of the canopy (Fig. 4.13). The next sections focus on simulations in realistic domains (*i.e.*, ShyfER).

4.4.3 ShyfER Experimental Set-up for Present and Future Climate Conditions

The effectiveness of the NBS, seagrass in this case, was evaluated by analysing ocean variables that play a significant role in coastal protection (*e.g.*, current velocity, SL) using numerical modelling under present and future climatic conditions. To achieve this objective, several simulations were needed (see Table 4.4).

The present condition was assessed with a ten-year simulation from 2010 to 2019

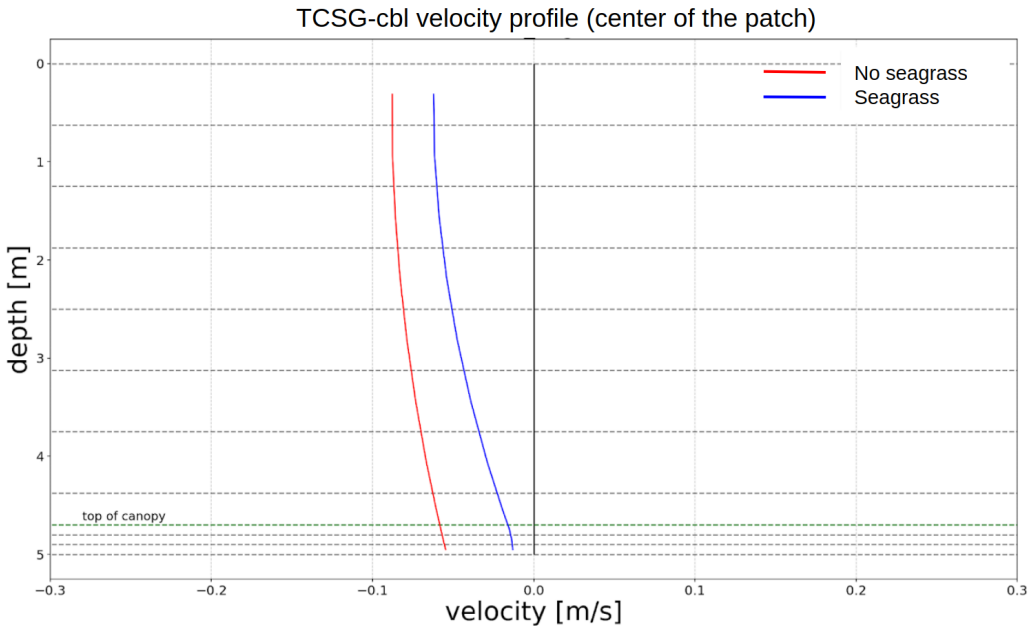

Figure 4.13: Velocity profile for TCSG-cbl simulation without seagrass (red) and with seagrass (blue) at the center of the vegetation patch (Yellow point in Fig. 4.10). A shear layer is generated at the top of the canopy for the case with seagrass.

(ERM-CNT) using 6h ECMWF analysis data at 12.5 km as the surface forcing and daily MED-MFS reanalysis at 1/24° as initial and boundary conditions. In the shallow northern Adriatic Sea, although tides are an important component of the total SL, they are not considered in the MED-MFS reanalysis product. In order to account for tides, the daily SL input data were interpolated hourly and added to the hourly astronomical tides computed by TPXO model (Egbert and Erofeeva, 2002). The signal was then provided as a BC to ShyfER.

Along the ER coast, the run-off of ten rivers was provided as the lateral boundary condition at the river mouth indicated in Figure 4.6. The discharge of the Po River measured by Arpae at Pontelagoscuro (Fig. 4.15) was divided among seven branch of the delta following Arpa-Veneto (2012), except for the Po of Goro, where the relation 2.1 was used. All the other river run-offs provided in ShyfER were computed from climatology (Raicich, 1994).

There are several possible designs for the seagrass distribution. The final design chosen for the simulations is indicated by green triangles on the right in Figure 4.6. This selec-

Simulations	Period	Atmospheric forcing	IC and BC	River	Seagrass
ERM-CNT	2010-2019	6h ECMWF analysis at 12.5 km	daily MED-MFS reanalysis at 1/24° + tides from TPXO	Po River from Arpae data + climatology (Raicich, 1994)	No
ERM-SG	2010-2019	6h ECMWF analysis at 12.5 km	daily MED-MFS reanalysis at 1/24° + tides from TPXO	Po River from Arpae data + climatology (Raicich, 1994)	Yes
ERM-CNT-SC	2010-2019	6h MedCordex-Cosmo scenario at 0.11°	daily MedCordex-NEMO scenario at 0.11° + tides from TPXO	Po River from Arpae data + climatology (Raicich, 1994)	No
ERM-SC	2040-2049	6h MedCordex-Cosmo scenario at 0.11°	daily MedCordex-NEMO scenario at 0.11° + tides from TPXO	Po River scenario (Vezzoli et al., 2015) + climatology (Raicich, 1994)	No
ERM-SC-SG	2040-2049	6h MedCordex-Cosmo scenario at 0.11°	daily MED-MFS reanalysis at 1/24° + tides from TPXO	Po River scenario (Vezzoli et al., 2015) + climatology (Raicich, 1994)	Yes

Table 4.4: Table of experiments

tion considered the seagrass requirements for life sustainment and distribution found in the literature (Danovaro et al., 2020). The most limiting factor is the availability of light. Due to the high turbidity of Adriatic Sea coastal water along the ER, from the Po River sediment discharge, seagrass can survive only in shallow waters. The seagrass was then positioned between 2 m and 10 m depths. Areas with very energetic waves does not support the growth of seagrass. The chosen area has a mean wave height $< 0.4\,m$ which may allow the seagrass root system to be efficiently anchored to the bottom. Seagrass tends to develop and grow in patches at the bottom, hence, the patch distribution of seagrass was chosen as the most realistic (Boscutti et al., 2015; Danovaro et al., 2020).

The NBS was also tested under future climate conditions. The ten-year period from 2040 to 2049 was simulated (ERM-SC) taking scenario data from the MedCordex initiative (Ruti et al., 2016) considering the representative concentration pathway 8.5 (RCP8.5, IPCC, 2013). MedCordex is an implementation of regional climate models (RCMs) focused on the Mediterranean area and was conceived as part of the coordinated regional climate downscaling experiment, CORDEX. It uses coupled atmosphere-ocean models to account for better air-sea interaction. COSMO-CLM

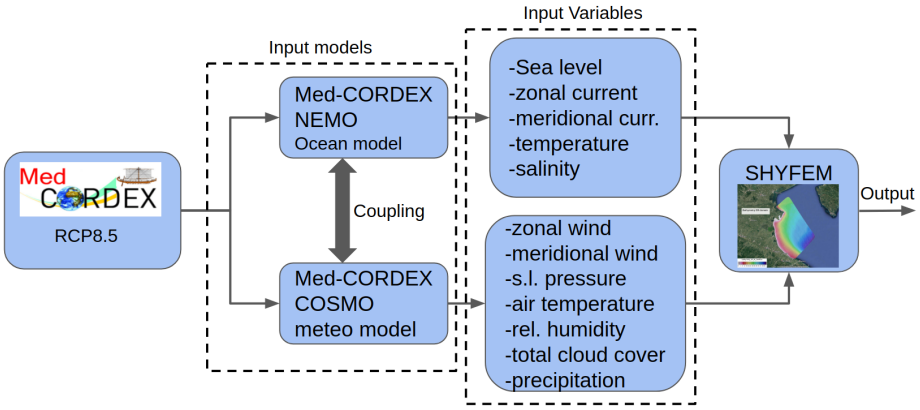

Figure 4.14: MedCordex models and the variables provided for ShyfER.

(Lange et al., 2014) is the climate version of the COSMO model (Steppeler et al., 2003) and is the atmospheric part of the coupled model described in Cavicchia et al. (2015, 2016). The ocean part is given by NEMO_MFS (Oddo et al., 2009) at 1/16° of horizontal resolution and 71 levels along the vertical. The coupled system was de-

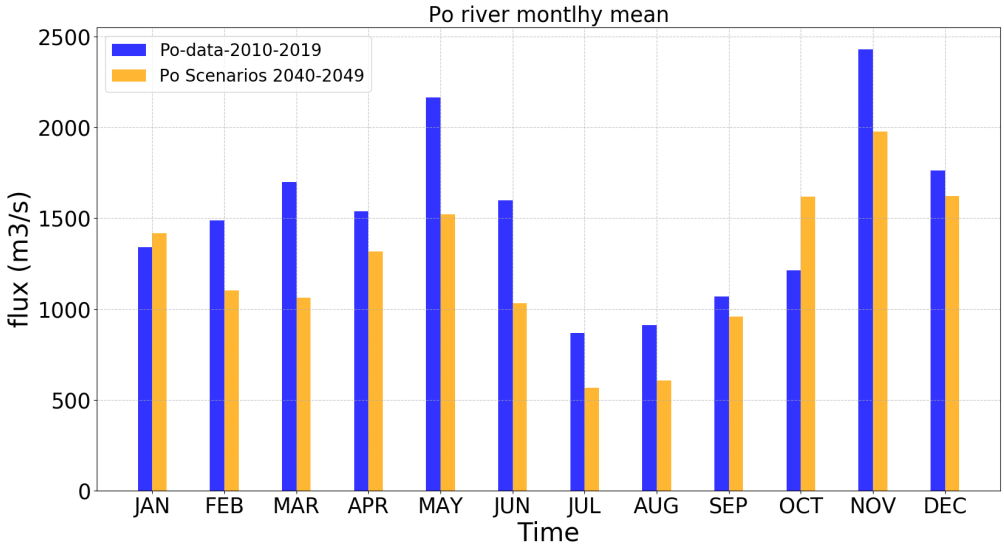

Figure 4.15: Monthly mean values of the Po River discharge from data for the period 2010-2019 (blue) and from Vezzoli et al. (2015) scenarios for 2040-2049 (orange).

veloped at different resolutions of the meteorological model (0.5° and at 0.11°). In the current work the output of the COSMO-NEMO_MFS model at 0.11° was provided as surface forcing to ShyfER (Fig. 4.14). The tides computed by TPXO were added

to ShyfER, following the same methodology described for the present conditions. Po River scenario data from Vezzoli et al. (2015) were used for the ERM-SC simulation (Fig. 4.15) while climatology values (Raicich, 1994) were used for the other rivers since no scenario data were available. MedCordex dataset was also used to simulate the 2010-2019 period (ERM-CNT-SC). This simulation was needed for an homogeneous forcing and to better compare present and future conditions.
After verification of the seagrass implementation in SHYFEM (see Sections 4.4.1 and 4.4.2), simulations were performed by activating the "vegetation module" for both present (ERM-SG) and future (ERM-SC-SG) conditions. The results of the simulations and the assessment of NBS is described in Section 4.5.

4.4.4 Model Validation

The control run (ERM-CNT) was used to validate the model for the entire ten-year simulation period (2010-2019), comparing the model output of salinity, temperature, SL and the observations (Fig. 4.16) available at Porto Garibaldi station, where a CTD and a tide gauge are installed (yellow point in Figure 4.6). The model output shows

	Salinity				Temperature				sea level		
Simulation	**R**	**BIAS** (psu)	**RMSE** (psu)	**MAE** (psu)	**R**	**BIAS** (°C)	**RMSE** (°C)	**MAE** (°C)	**R**	**RMSE** (m)	**MAE** (m)
ERM-CNT	0.71	1.58	3.89	2.93	0.98	-1.65	2.29	1.82	0.69	0.10	0.08
ERM-CNT-SC	0.33	2.53	5.72	4.30	0.93	-3.45	4.31	3.71	0.17	0.15	0.11

Table 4.5: Pearson correlation coefficient, BIAS, RMSE and MAE for salinity, temperature and SL of ERM-CNT and ERM-CNT-SC at Porto Garibaldi station.

a general good agreement with the observations (see Table 4.5 and Fig. 4.16). The salinity of the ER coastal area is greatly influenced by the high discharge rate of the Po River and follows its seasonality. High freshwater inflow in spring and autumn lead to low salinity values along the ER coast and vice-versa for the summer season. This feature is well reproduced by the model. However, in the case of a sudden increase in the Po River discharge, low salinity values are observed in a short time period and the model is not able to reproduce such an abrupt salinity gradient (*e.g.*, end of 2018 in

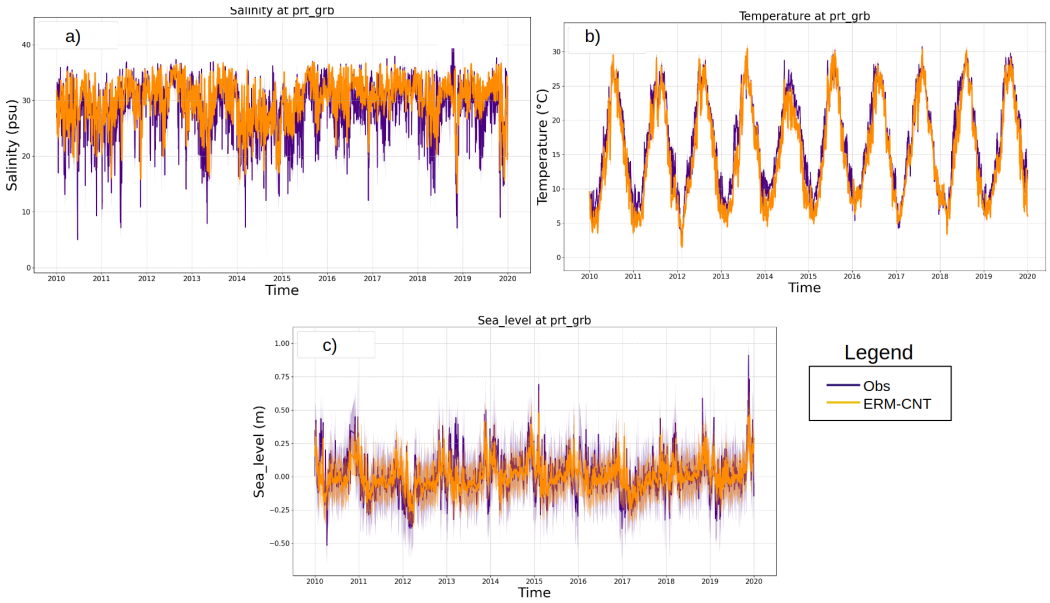

Figure 4.16: Daily comparison between model output of ERM-CNT simulation and observations for salinity (a), temperature (b) and sea level (c) at Porto Garibaldi (Yellow point in Figure 4.6). The shaded areas indicates the daily standard deviation for model output (dark orange) and observations (blue).

Fig. 4.16a. This partially explains the quite high salinity RMSE obtained.

The modelled temperature and its variability is good (Fig. 4.16b), the seasonal cycle is reproduced with no drifts. However, the model has a cold bias, especially during the winters of 2011, 2013, 2014, 2015 and the summer of 2014. The last four years of simulation show a better agreement with observations.

The daily SL comparison is shown in Fig. 4.16c. The variability of the model output is smaller compared to the observations. Nevertheless, the comparison is generally satisfactory and the model reproduces the observed SL.

The ERM-CNT-SC run uses MedCordex scenario data (RCP8.5) to simulate the present state (2010-2019), in order to have a consistent dataset available to compare with future scenarios. The ERM-CNT-SC run is assessed by comparing the model output with observations. The statistical scores for salinity, temperature and SL are summarized in Table 4.5 and the time series comparisons are shown in Figure 4.17a, b and c. Unlike ERM-CNT, where meteorological and ocean forcing come from the analysis and reanalysis respectively (*i.e.*, where data assimilation is used), no data from

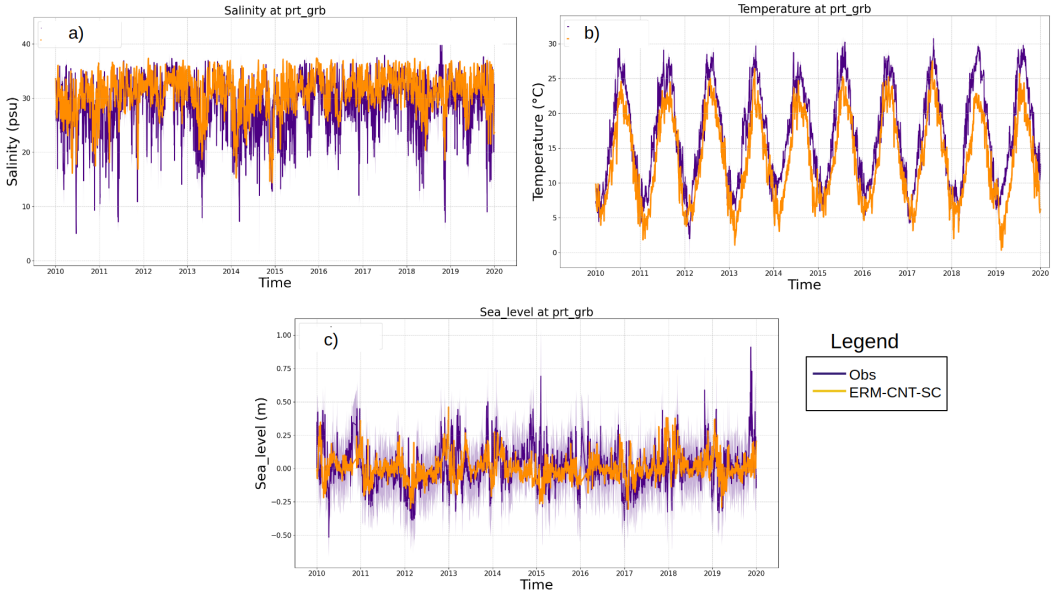

Figure 4.17: Daily comparison between model output of ERM-CNT-SC simulation and observations for salinity (a), temperature (b) and sea level (c) at Porto Garibaldi. The shaded areas indicates the daily standard deviation for the output (dark orange) and observations (blue), respectively.

observations are entered in the ERM-CNT-SC simulation, except for the Po River discharge. This is reflected in the low correlation and high BIAS, RMSE and MAE in ERM-CNT-SC. A high correlation remains in the temperature due to the strong seasonal cycle although a high cold BIAS affects the simulation. Nevertheless, despite the limitation due to the use of scenario data, the scores and time series are relatively good.

4.5 Results

The results of the model are shown here for the simulations listed in Table 4.4. The present state is assessed in Section 4.5.1. The results for future scenario simulations and the comparison with present conditions are shown in Section 4.5.2.

4.5.1 Present State Conditions

The ERM-CNT run is shown by means of current velocity, salinity, temperature and SL. Monthly means for the entire 2010-2019 are computed and analyzed to assess sea-

grass effects. The western Adriatic coastal current (WACC) shown in Figure 4.18a

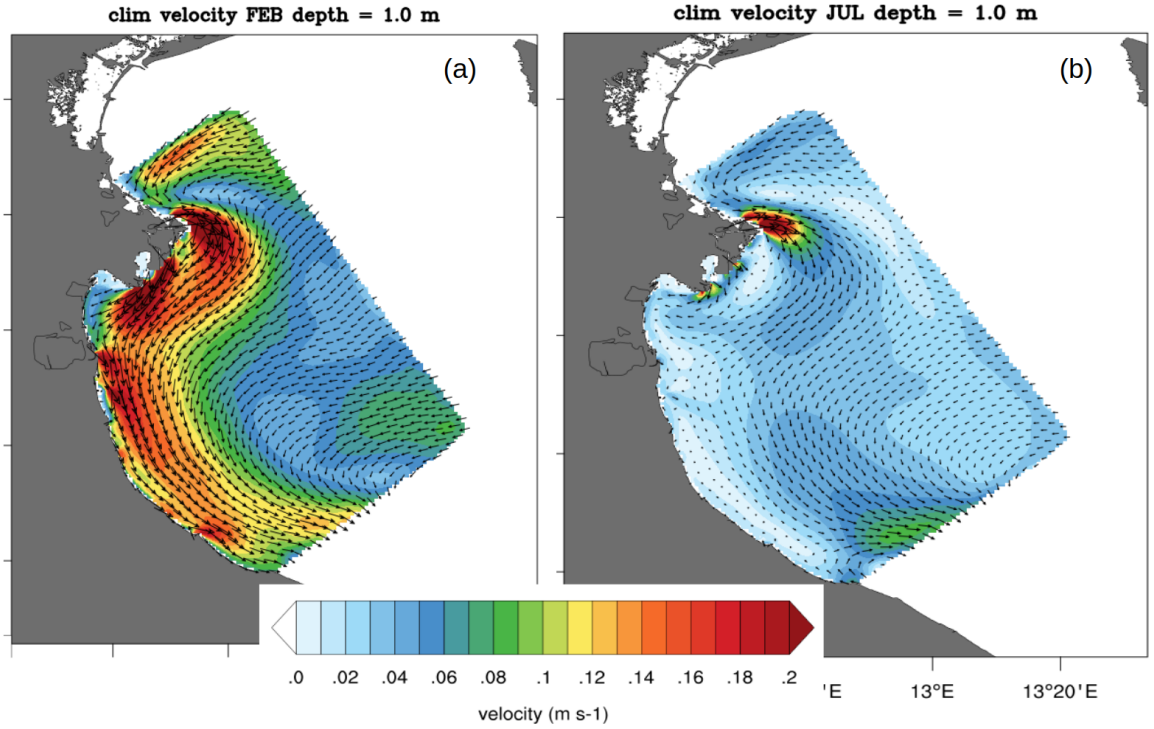

Figure 4.18: ERM-CNT surface current velocity for February (a) and July (b).

and b (for February and July, respectively) has a strong seasonal variability. In winter the WACC is stronger and closer to the coast due to the dominant north-westerly and north-easterly wind forcing. Ekman transport induces downwelling circulation which in turn retrieve seawater from the offshore generating strong horizontal salinity gradients (Fig. 4.19a) and the steepening of the isohalines (Fig. 4.19c). Very different conditions are generated in the summer. The WACC weakens and is shifted offshore (Fig. 4.18b) and fresher surface water spreads seaward (Fig. 4.19b and d). The buoyancy input from Po River is another important forcing for the WACC with the plume extending southward, spreading freshwater along the entire ER coast.

February is the coldest month (not shown) with surface temperatures ranging from $4-5\,°C$ inside the Goro and Scardovari lagoons, to $11\,°C$ offshore. August is the hottest month, with temperatures of about $26.5-27\,°C$ except at the Po River mouths where lower temperatures $(15-20\,°)$ are found.

The seagrass NBS for the present state was assessed analysing the ERM-SG simula-

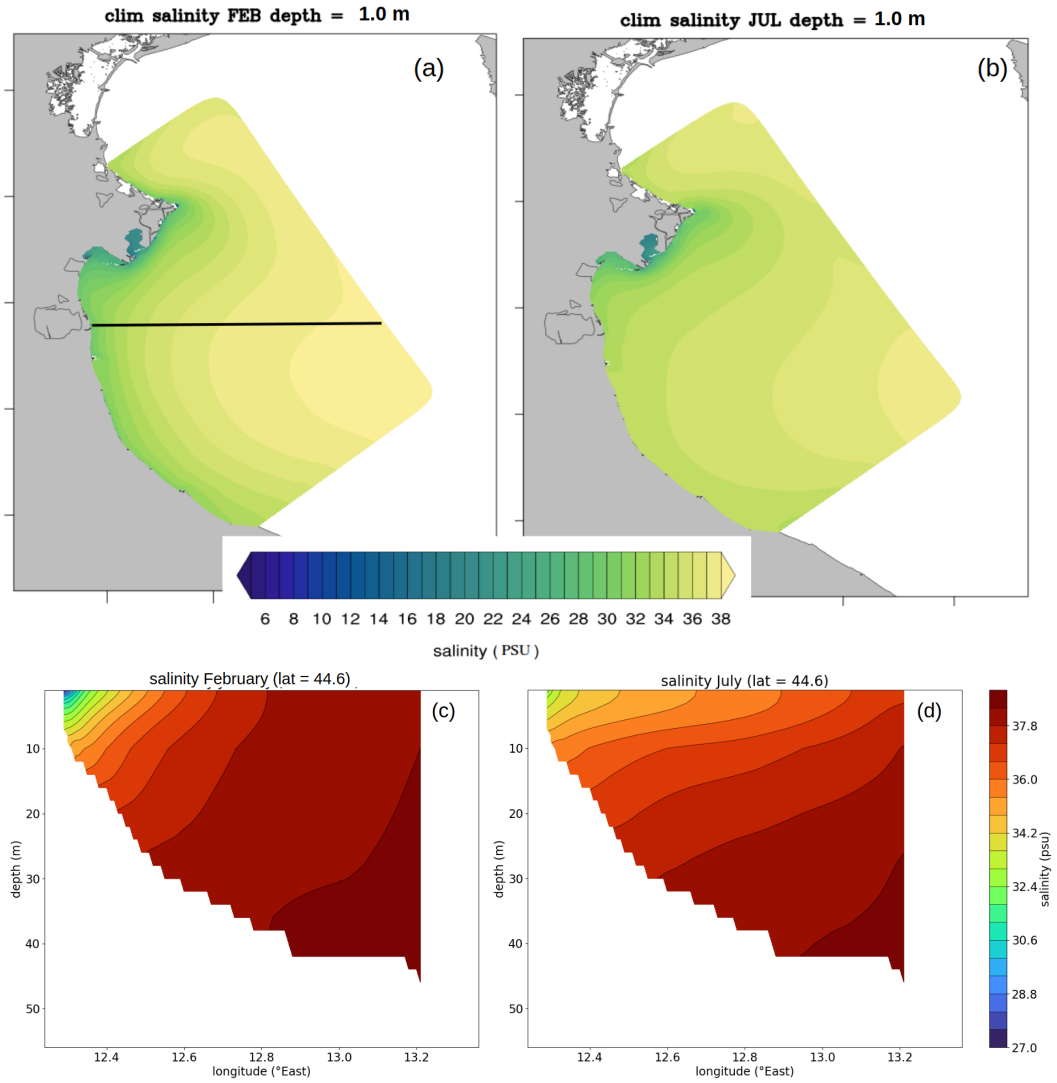

Figure 4.19: ERM-CNT surface salinity for January (a) and July (b). Cross section salinity along the black line in (a) is shown for January (c) and July (d).

tion and comparing it with the control simulation (ERM-CNT). Since the seagrass effects are very local, the focus is on the Bellocchio area (black rectangle in Fig. 4.6) where the vegetation was implemented. The presence of seagrass shows an extremely limited impact on SL. The February and July mean SL differences between ERM-SG and ERM-CNT are shown in Figure 4.21a and b. The effects of seagrass on the SL are as expected (Beudin et al., 2017). Since in the Bellocchio area the currents are S/SW, the northern area (NW of the vegetation) shows an increase in SL, while south of the seagrass zone, there is a decrease in SL. In July the difference shows a smaller amplitude since the currents are much weaker. However, the overall effect is negligible.

The SL differences are of the order of $10^{-4}/10^{-5}\,m$. This can be explained by the high H/l_v ratio (from a minimum of 10 to a maximum of 50). The length of the seagrass is too short compared to the water column thickness to have any real effect on the SL. The seagrass reduces the bottom velocity amplitude up to $1-2\,cm/s$ (Fig. 4.21c and d). In that area the current amplitude at the bottom is in the order of a few cm/s (2 to $5\,cm/s$), hence, the observed velocity reduction could have a considerable impact on the bottom dynamics of the area (*e.g.*, sediment transport, erosion, etc.). The surface currents are very weakly affected by the presence of vegetation, with a reduction in velocity of up to 3 mm/s in February in the area covered by the vegetation while a weak increase ($1-1.5\,mm/s$) can be seen east of the patch. The smaller velocity reduction in July is due to weaker currents during summer. Very small differences can be observed in the bottom temperature and salinity (not shown) due to a different tracer advection in the area of vegetation.

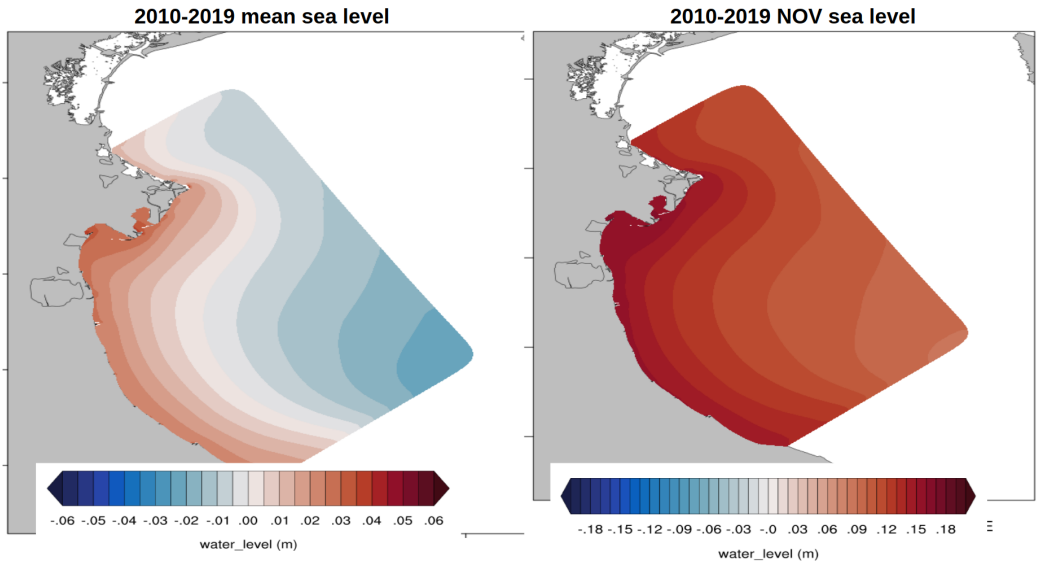

Figure 4.20: ERM-CNT mean SL for the 2010-2019 period (a) and the November monthly mean (b).

The effects of seagrass on small time scales are assessed considering an extreme storm surge event occurring on 5 and 6 February 2015. A strong Bora wind (with gusts stronger than $25\,m/s$) blew over the ER coast, causing damage to services and in-

frastructures, despite the early warning system working properly. Figure 4.22a shows the SL difference between ERM-SG and ERM-CNT for 6 February 2015, when the wind reached its maximum speed. The area upstream of the vegetation shows a slight increase in the SL, while a decrease is found downstream, with distortion due to both the coastal geometry and the slanted direction of the currents with respect to the vegetation patch.

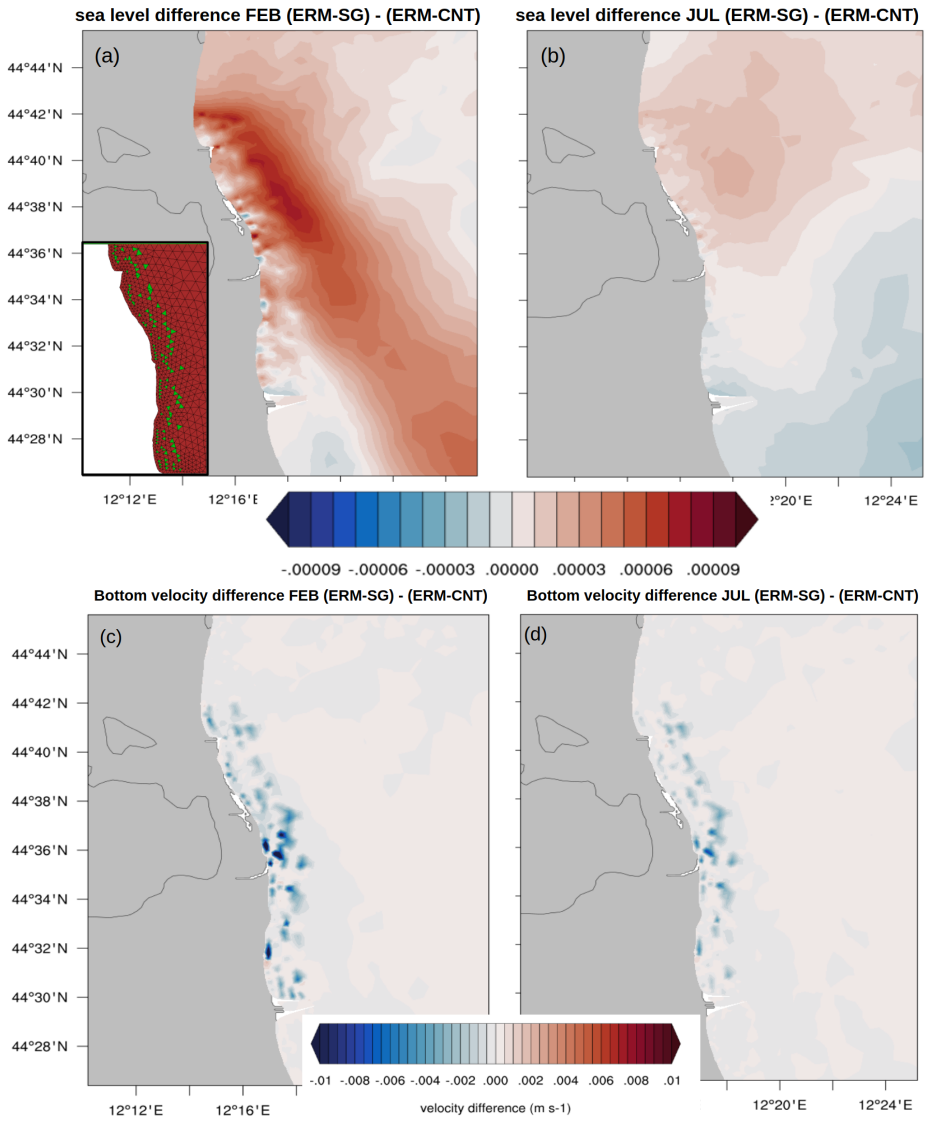

Figure 4.21: Sea level (top) and bottom velocity (bottom) difference between ERM-SG and ERM-CNT for the Bellocchio coastal area. February and July mean are shown on the left (a,c) and on the right (b,d) respectively. The position of seagrass is indicated on the bottom left of (a).

The mean SL for 2010-2019 (Fig. 4.20a) shows maximum values along the ER coast, south of the Po Delta. The maximum SL is observed in November (Fig. 4.20b), in agreement with historical observations of storm surges that usually occur during late autumn and winter along the ER coast.

However, even in this case, where the currents reach values of $0.25 - 0.3\,m/s$, the

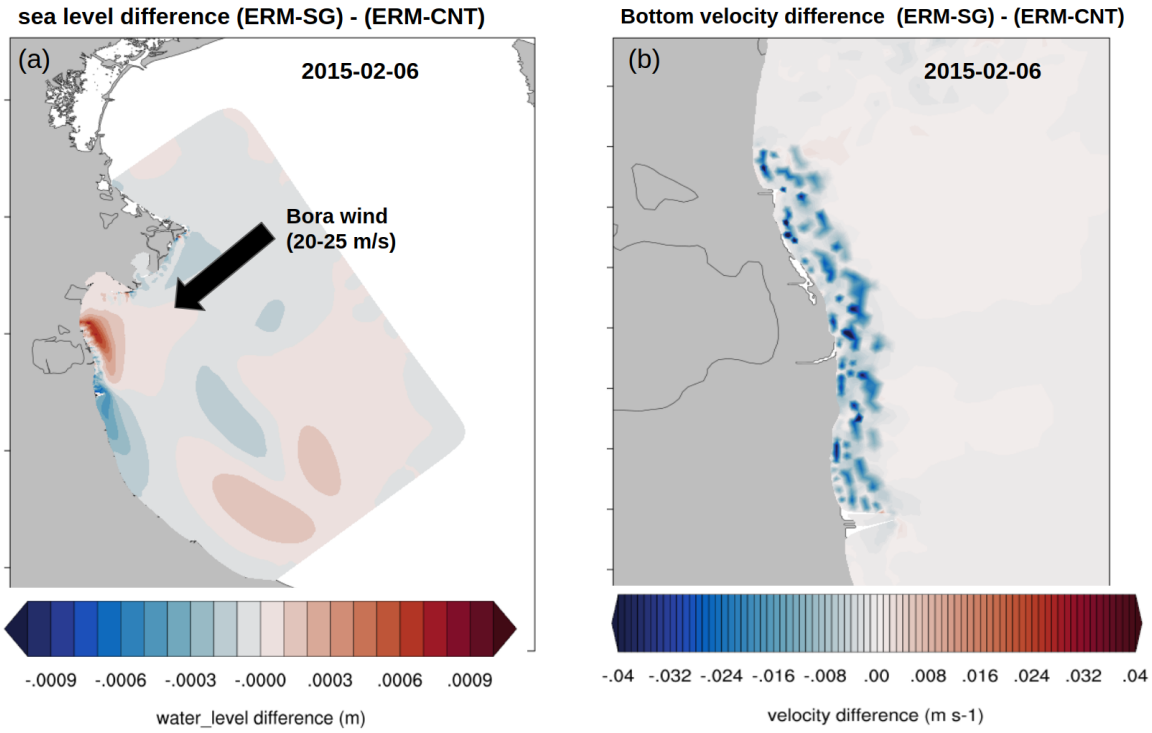

Figure 4.22: SL (a) and bottom velocity (b) difference between ERM-SG and ERM-CNT for 6 February 2015. Direction and maximum intensity of the wind is represented in (a).

changes in SL do not exceed $1\,mm$, both positive and negative. The bottom velocity (Fig. 4.22b) is reduced of up to $4 - 5\,cm/s$ (from 30 to 50 %). Note that the results obtained were found under the assumption of rigid vegetation. This can lead to an overestimation of the effects due to seagrass, especially in cases where the current velocities reach high values. The implementation of seagrass flexibility in SHYFEM is under development.

4.5.2 Future Climate Scenario Conditions

In this section the future scenario of the ERM-SC simulation is compared with ERM-CNT-SC to estimate changes that are likely to occur in ocean variables for 2040-2049. Monthly mean variables are computed for current velocity, salinity, temperature and SL.

Changes in the WACC dynamics along the ER coast are determined by the wind

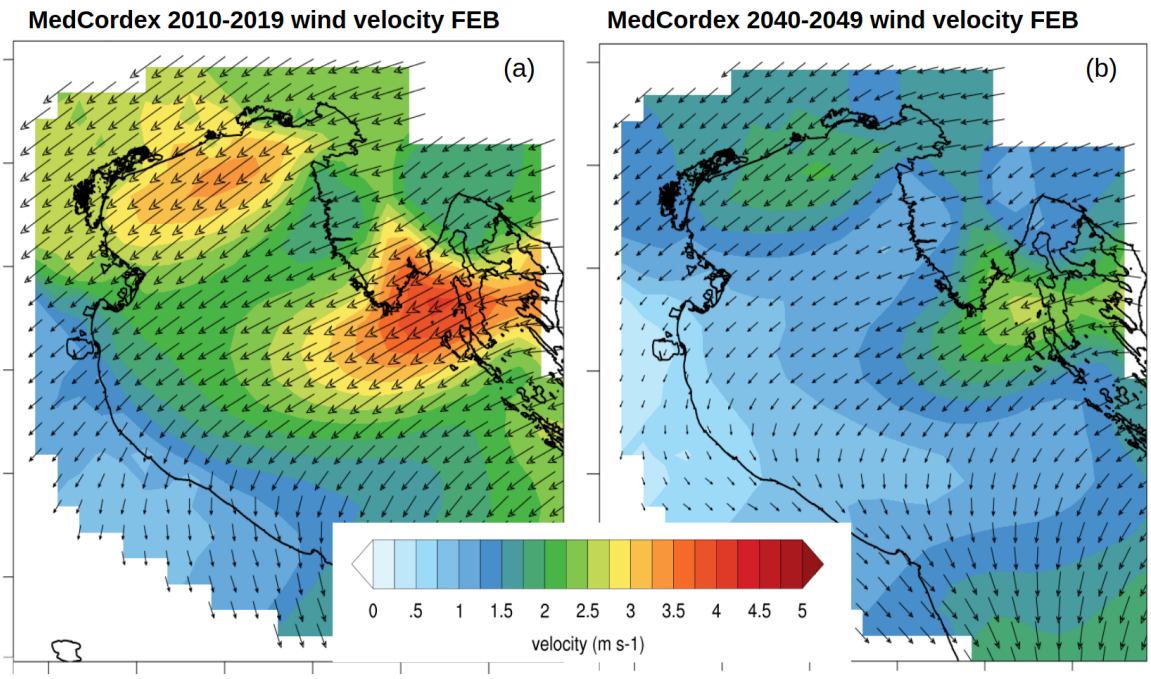

Figure 4.23: Mean February wind from MedCordex dataset for 2010-2019 (a) and 2040-2049 (b).

forcing and the buoyancy freshwater input of the Po. According to MedCordex data, the mean wind of the 2040-2049 late winter season, will be weaker than the 2010-2019 wind of the same period (Fig. 4.23a and b). In the summer, a very slight increase in wind from the east is expected on the east side of the Adriatic Sea (not shown), slightly affecting the current structure and intensity along the ER coast. When the wind does not play a key role in determining the sea dynamics, the Po discharge becomes fundamental in determining the WACC intensity and position. According to Vezzoli et al. (2015), the mean Po discharge will decrease from the current value of

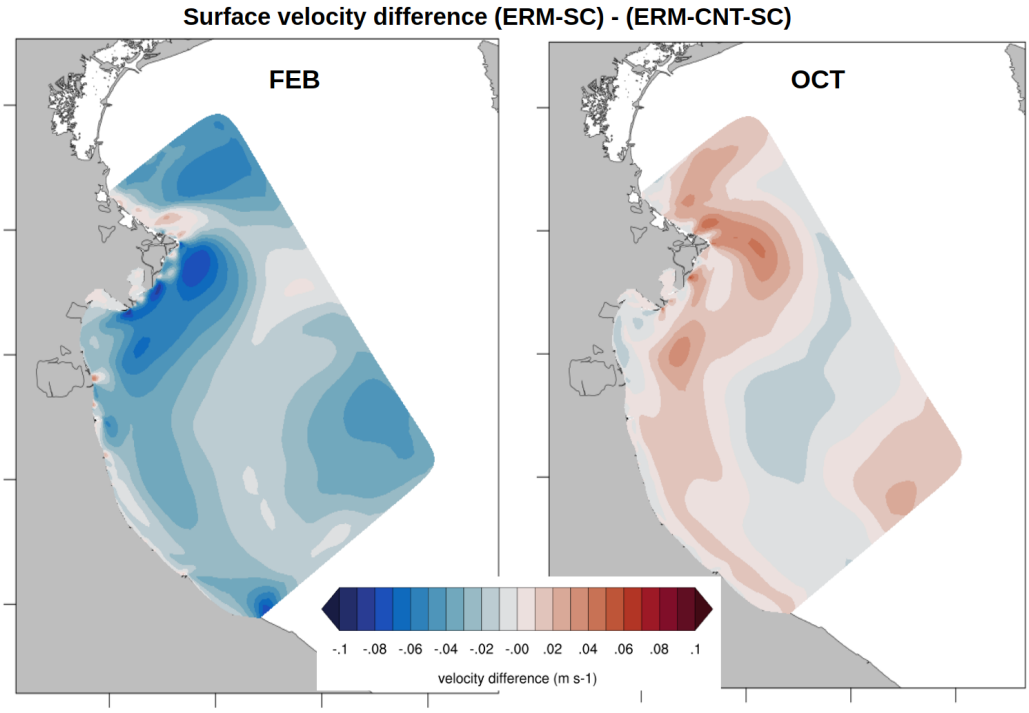

Figure 4.24: Mean current intensity difference between ERM-SC and ERM-CNT-SC for February (a) and October (b).

$1500\,m^3/s$ to $1200\,m^3/s$ with strong impacts on both dynamics and the salinity budget in the ER coastal area. Figure 4.24a shows the reduction in the intensity of the WACC for the February scenario by up to about 50 %, due to both a less intense wind (Fig. 4.23b) and a reduced Po discharge (Fig. 4.15). On the other hand, current intensity is expected to exceed the present values in October (Fig. 4.24b). The wind is not expected to change in terms of the ERM-SC October mean, however, the Po is likely to have greater discharge in the future for the month of October which in turn will feed the coastal currents. In general, a mean $0.01\,m/s$ ($\simeq 10\,\%$) decrease is expected in the current intensity along the ER coast (Fig. 4.25a).

The mean SL difference between ERM-SC and ERM-CNT-SC is shown in Figure 4.25b with positive values of about $1-1.2\,cm$. This denotes a maximum rate of $0.4\,mm/year$ along the ER coast. A similar rate was found by analysing the MedCordex dataset used to force the simulations in the same area. However, this is a strong underestimation compared to the expected SL rise trend, which from historical data (Copernicus climate

change service[1]) is known to be around 2.5 $mm/year$. Studying the rise in the SL is beyond the scope of this work.

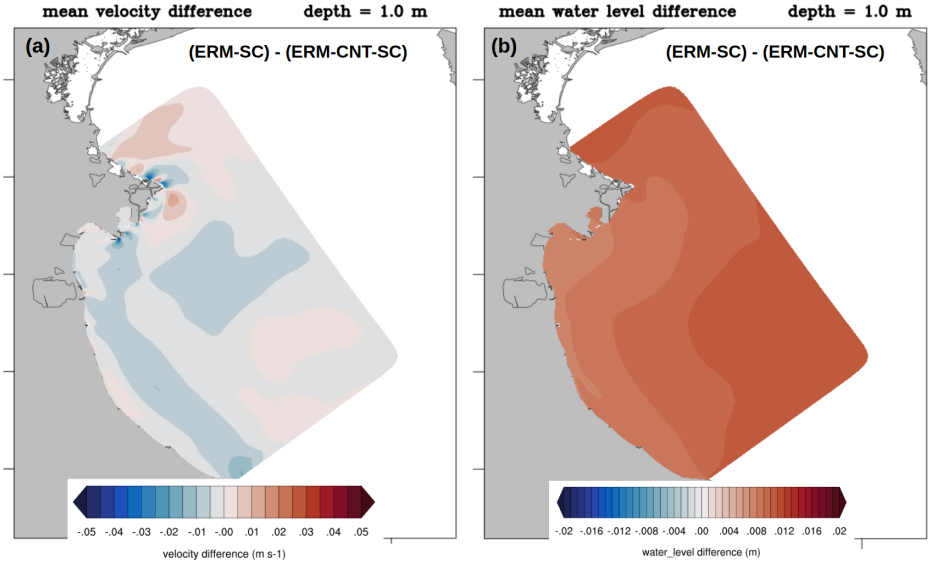

Figure 4.25: Mean current intensity (a) and SL (b) difference between ERM-SC and ERM-CNT-SC.

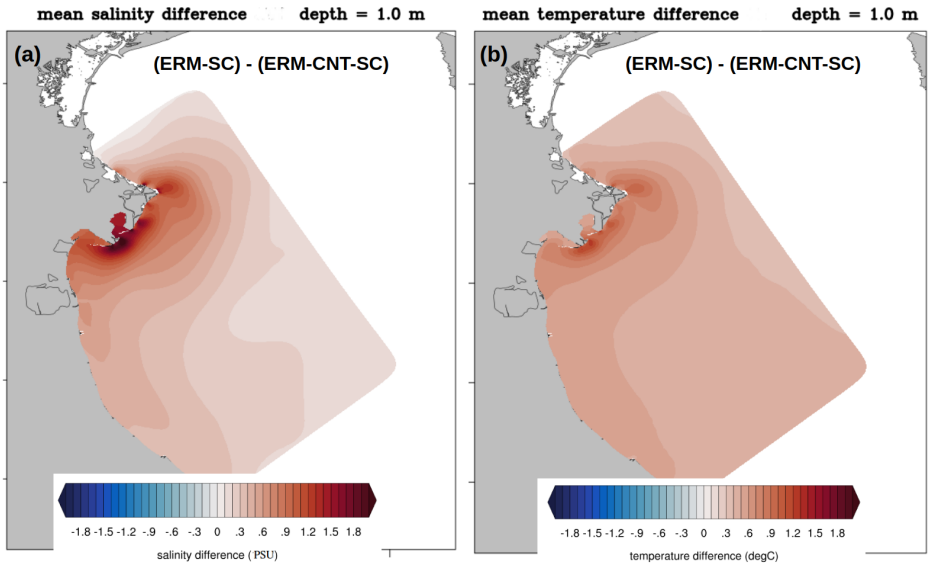

Figure 4.26: Mean salinity (a) and temperature (b) difference between ERM-SC and ERM-CNT-SC.

[1] https://climate.copernicus.eu/sea-level

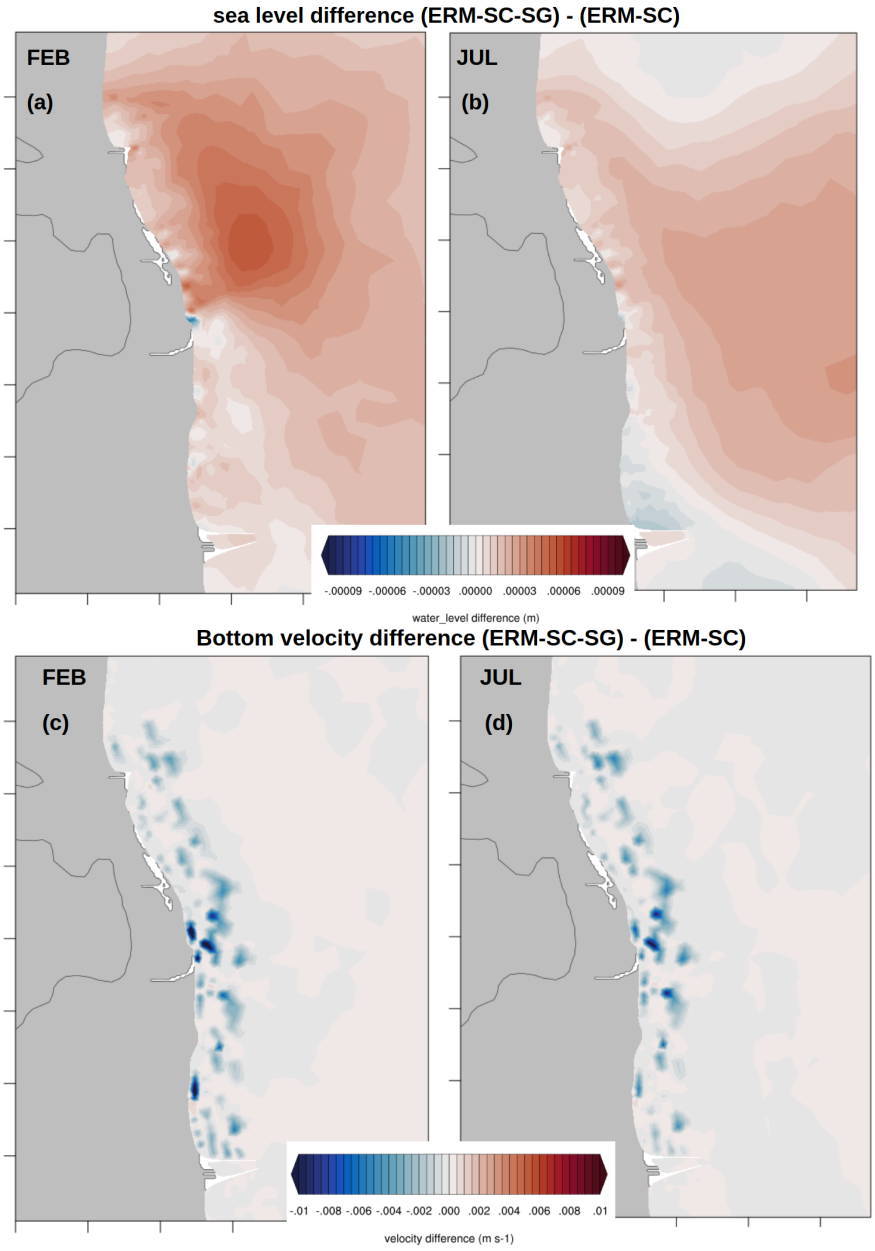

Figure 4.27: SL (top) and bottom velocity (bottom) difference between ERM-SC-SG and ERM-SC for the Bellocchio coastal area. February and July means are shown on the left (a,c) and on the right (b,d), respectively.

Since the difficulties in predicting the SL in the Mediterranean Sea are renowned (Adloff et al., 2017), no further verification was carried out.

The surface salinity (Fig. 4.26a) shows a mean increase of $0.2 - 0.3\,psu$ offshore that increases substantially up to $2.5 - 3\,psu$ close to the mouth of the Po due to future lower discharges. The seasonal variability is strictly connected to the future discharge.

The mean temperature is higher in ERM-SC of $0.5 - 0.6\,°C$ with a peak of $1 - 1.5\,°C$ at the mouth. However, the peak close to the river mouth is determined not by the different temperatures of the river, since no data were available for future river temperatures (the same Po temperature as in present conditions were used), but to a lower future discharge of the Po.

The role of seagrass was studied to predict the future climate, comparing the ERM-

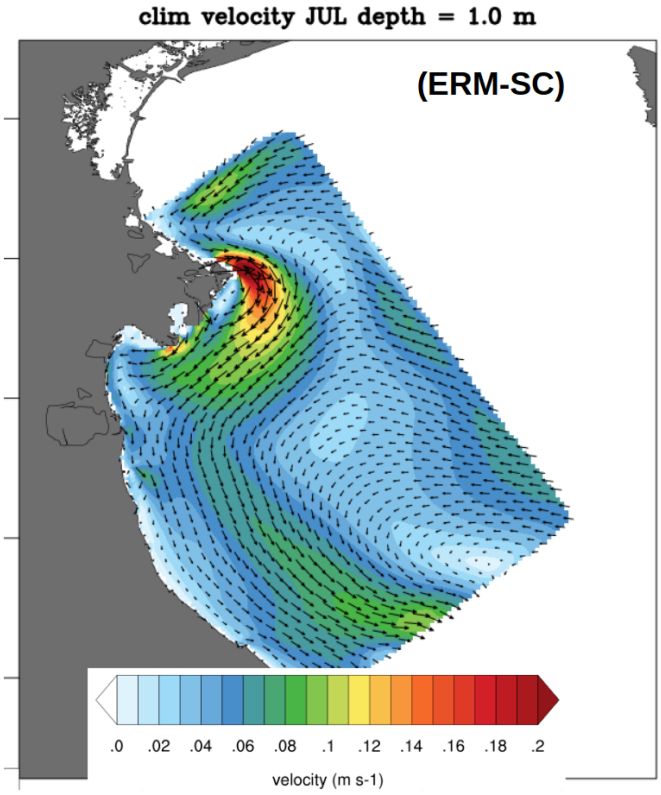

Figure 4.28: Mean July surface current intensity for ERM-SC simulation.

SC-SG simulation with ERM-SC. The changes occurring in the currents slightly impacts on the effects of seagrass on the flow. The mean February SL difference (Fig. 4.27a) is positive but lower than 2010-2019 (max $\simeq 6 \times 10^{-5}\,m$). This can be explained by a lower intensity of the currents in winter. The slightly stronger wind and the lower discharge of the Po in the summer lead to a position of WACC being closer to the coast (Fig. 4.28). Along with weaker currents in winter, this generates less variability in the currents along the ER coast, which in turn reflects a lower variability of seagrass consequences on the flow (Fig. 4.27). Despite the lower variability of the

future scenario, the bottom velocity is reduced in the same way as in present conditions.

4.6 Concluding Remarks

Seagrass was studied as a possible NBS to protect the ER coast from high SL storm surge events. The presence of seagrass was found to impact on the ocean state variables in complex ways. The SL was modified by the bottom vegetation. An increase and a decrease in the SL were observed upstream and downstream of the seagrass position, respectively. However, the seagrass effect decreased very rapidly with an increasing H/l_v ratio, leading to a low amplitude effect in controlling the SL during storm surge events if a realistic seagrass distribution is used. Despite this, the reduction in the bottom velocity induced by the seagrass is sensible and could play a role in reducing coastal erosion due to changes in the along-shore sediment transport. In addition, the root system of seagrass can trap sediments, however this is beyond the scope of this work. We also investigated investigated the effects of seagrass both in present and future climate conditions. For what we believe is the first time, a very high-resolution coastal model was nested into RCP8.5 climate scenario conditions, and the effects with and without seagrass were observed. The first result is that this downscaling is effective for studying the impacts after a good calibration of model parameters. A parallel study (Pillai et al., unpublished), using the same domain, investigated the role of seagrass in reducing wave energy with promising results. They can diminish storm surge impacts due to waves more than the SL directly, and could be playing a sensible role in the current velocity reduction, hence reducing coastal erosion. However, it is important to stress that neglecting vegetation flexibility can lead to an overestimation of seagrass effects on the flow. The addition of this feature and the coupling of SHYFEM with a wind wave model will add insights in the physics of flow-wave-vegetation interaction in a realistic environment. There are still important effects that have not yet been considered. Among others, the biological cycles of seagrass have not been considered, which will be the scope of future work.

Chapter 5

Conclusions and future perspectives

The Adriatic Sea, as a whole, is a complex system where many forcing act to influence ocean variables and increase coastal hazard. Tides have a significant amplitude ($\simeq 1\,m$ in northern Adriatic) and can give a fundamental contribution to flooding events (*e.g.*, "Acqua alta" events in Venice). Intense winds from north-eastern (Bora) and south-eastern (Scirocco) directions may generate strong storm surges with potentially disastrous consequences for human lives and infrastructures along the north Italian Adriatic coast, also contributing to amplify coastal erosion. Moreover, the peculiar shape of the Adriatic Sea contributes to the generation of wind induced seiches that may reach amplitudes of $50\,cm$ and, if in phase with tides, can be a dangerous threat. The major Italian river, the Po, discharges directly in the northern Adriatic Sea and it is a fundamental component of the WACC current, providing a buoyancy input and an high load of nutrients that impacts the surrounding areas and strongly influences the salinity budget of the Adriatic Sea.

Many modelling research works focused on the study of the Adriatic Sea at basin scale to understand the main large-scale dynamical and biogeochemical features as well as to forecast sea state and ocean variables to prevent or reduce the risk from inundation. However, much less efforts were spent for the ocean modelling at local scales to address small scale dynamical interactions that occur in coastal domains such lagoons or estuaries, where the coastal geometry and the influence of the bottom friction become particularly important for local circulation. Many human activities and infrastruc-

tures are located in coastal areas, suffering economical losses due to coastal erosion and life-threatening inundation. The sea level rise expected in the next decades will enhance even more the risks connected to flooding events, especially in a sensible area like the ER coast, already affected by subsidence.

The availability of powerful computational resources and unstructured grid models, allow to carry out limited area simulations with extremely high-resolutions never achieved before. Local modelling tools, connected to a robust observational network and validated boundary conditions, may provide reliable answers to the needs of local authorities, necessary for coastal and human activities protection.

In this work, the unstructured grid 3-D model SHYFEM is implemented on different domains (GOLFEM and ShyfER) along the ER coast, to develop useful tools for coastal management and to allow the evaluation of the efficiency of the seagrass as NBS for coastal protection. The variable resolution of the numerical grid, allow to describe at the same time large- and small- scale features of the circulation and to include feedback among different spatial scales. The grid can be extended into rivers to reproduce the mixing processes that occur in estuaries and control the salt wedge. The aims of the thesis are carried out through the development of three main activities:

- The GOLFEM model is the implementation of SHYFEM at local scale for the Goro Lagoon with a very high-resolution, not available in previous studies. The Goro Lagoon is a highly productive area (clams) that suffer every year of economical losses due to eutrophication and it is occasionally subjected to flooding events. The domain includes the Po River Delta, that represents an important forcing for the local dynamics and takes the boundary conditions from the operational meteorological and ocean models running at Arpae-SIMC. The results show in detail the estuarine lagoon circulation generated by the freshwater input of the lagoon and enhanced by the internal channels. The exchanges with the open sea occur through the two main inlets, located respectively at the extreme west and extreme east of the lagoon mouth, where velocities of $1\,m/s$ may be reached during spring tides. The connections of the lagoon with a branch of

the Po River (Po of Goro) and the Po of Volano is fundamental for the salinity budget. The high-resolution of GOLFEM allows to reproduce well the salinity variability, even if some discrepancies with observations appear due to the manual non-recorded closures of the river-lagoon connections during river floods. After the calibration and validation of the model with the observational network over one year of simulation, the model was used to evaluate potential positive effects of dredging works on the lagoon dynamics and salinity, fundamental parameters for clams farming. Two scenarios were evaluated in terms of current velocity and salinity to allow the computation of two fitness indices (FT1 for velocity and FT2 for salinity) for optimal clams growing conditions. The dredging of the eastern inlet channel (SC1) increases the saltwater flux in the eastern side of the lagoon where the FT2 increase of about +10 % while FT1 increase locally in the channel of about (+10 %) while decrease NW of the inlet channel of about −10 %. The dredging of new channels in the ex-nursery area between the spits (SC2) has a minimal impact on the dynamics of the area, where the FT1 increase is low and confined within the channels. The new channels connect the SE area of the lagoon, with the area between the spits. The FT2 index increases up to +15% in the SE area of the lagoon where salt water infiltrates from the ex-nursery area. On the other hand, fresher water from the eastern part of the lagoon infiltrates in the ex-nursery area where the FT2 decreases of about -5%. The dredging of new channels between the spits seems not to be sufficient to affects positively the area, since some benefits appear only in the SE area of the lagoon where no clams farms are present. However, even if SC1 shows benefits for the whole eastern portion of the lagoon, a negative impact is found for the dynamic index (FT1) NW of the eastern inlet that can not be neglected.

- GOLFEM model is used to develop an ensemble system (GOLFEM-EPS) for storm surge sea level forecast and for uncertainty evaluation. An ensemble of 45 members is made considering forcing from different ocean and meteorological models and perturbing the river discharge imposed as a lateral boundary con-

dition. Five storm surge events are considered and simulated. The EM is computed with a simple average and a weighting procedure is tested to compute an enhanced ensemble mean (WEM) based on the performance of each member during a training period. The EM and WEM are compared with two members of the ensemble: *exp-1* that uses the highest resolution forcing models (Cosmo-2I and Adriac) and *exp-13* that uses the operational models at Arpae-SIMC (Cosmo-5M and AdriaRoms). The results show that both EM and WEM perform much better than *exp-13* but that only WEM has a slightly better performance compared to *exp-1*. The final RMSE for the SL considering the forecast of all the events is respectively 22.9, 12, 11.5 and 11 cm for *exp-13*, EM, *exp-1* and WEM. A more robust probabilistic verification will be performed considering a larger number of events. The uncertainty analysis shows that boundary conditions, in terms of SR and tides, are the dominant forcing contributing to ensemble variability with values between 9 and 13 cm. Meteorological contribution to uncertainty is one order of magnitude lower with maximum values between 1 and 3 cm located in the southern coastal areas and lagoons. The lower impact to ensemble variability is given by rivers with maximum values between 3 and 4 mm confined along the coast. This work suggests that a storm surge EPS implemented on small domains should be based on a careful choice of the boundary conditions.

- The seagrass (*Zostera marina*) is evaluated as a possible NBS for coastal protection implementing SHYFEM along the ER coast (ShyfER domain). The physical effects of seagrass on the flow are studied with the 1-Dimensional GOTM turbulence model and then implemented and tested in the SHYFEM model. The NBS was assessed for present and future climate. After the calibration and validation of the model, the present state was simulated with a ten-year run from 2010 to 2019 using ECWMF analysis as meteorological forcing and CMEMS MFS reanalysis as initial and boundary conditions. The simulation was repeated adding the seagrass module and the results of both experiments were compared. It is found that the effects of seagrass on sea level are negligible (max $\pm 1\,mm$) and

greatly dependent from the depth of the water column and on current velocity. The bottom currents are reduced up to 50%, with possible influences in the bottom dynamics and coastal erosion. The future climate was simulated using MedCordex scenario data for the ten-year period 2040-2049. Scenario data were used also for the Po River. The results are similar to the one found for the present climate. The small differences in respect to the 2010-2019 period may be attributed to a different intensity and position of the WACC due to differences in the future wind and Po River discharge.

This is an overview of the possibilities of high-resolution modelling developed for coastal protection and management. The research work will continue in several ways and will focus on the coupling of SHYFEM with other numerical models. The coupling with a wind wave model (*e.g.*, WaveWatchIII) will allow to account for wave set-up in storm surge modelling, a contribution that is currently neglected but that can be important, especially during Bora events. A biogeochemistry model (*e.g.*, BFM) coupled with SHYFEM will be useful to evaluate the nutrients dynamics in the Goro Lagoon and along the ER coast, that is heavily influenced by the high nutrients load carried by the Po River. Eventually, the coupling with a sediment transport model will assess the sediment dynamics in the ER and will allow to estimate the potential benefits of the current reduction due to seagrass in preventing coastal erosion.

Appendix A

The Tidal Filter

The surge component (*i.e.*, SR) is computed using a frequency domain detiding procedure (Thomson and Emery, 2014; Forbes, 1988) based on the Fourier transform. If a continuous function $y(t)$ is defined on the entire domain of time t and the Fourier transform $Y(f)$ of $y(t)$ exists then the standard transform pair can be defined as

$$Y(f) = \int_{-\infty}^{+\infty} y(t) e^{-i2\pi ft} dt \tag{A.1}$$

$$y(t) = \int_{-\infty}^{+\infty} Y(f) e^{i2\pi ft} dt = \frac{1}{2\pi} \int_{-\infty}^{+\infty} Y(\omega) e^{i\omega t} dt \tag{A.2}$$

where f is the frequency and $\omega = 2\pi f$ is the angular frequency in radians per unit time. Since in the real world, time series have a limited extension (*e.g.*, sea level), the discrete Fourier transform must be used. If a time series $x(t)$ is considered, with a finite duration $T = N\Delta t$, then the discrete values are $x(n\Delta t) = x_n$ with $n = 1$ to N and the Discrete Fourier Transform (DFT) is

$$X_k = \Delta t \sum_{n=1}^{N} x_n e^{-i2\pi f_k n\Delta t} = \Delta t \sum_{n=1}^{N} x_n e^{-i2\pi kn/N} \tag{A.3}$$

$$f_k = k/N\Delta t, \qquad k = 0, ..., N \tag{A.4}$$

where f_N is the Nyquist frequency and frequencies f_k are confined to the f_N with positive frequencies $0 \leq f_k \leq f_N$ in the range $k = 0, ..., N/2$ and negative frequencies $-f_N \leq f_k \leq 0$ in the range $k = N/2, ..., N$. Since $f_{N-k} = f_k$ only the first $N/2$ values are unique and the focus will be only in the positive interval. The Inverse Fourier

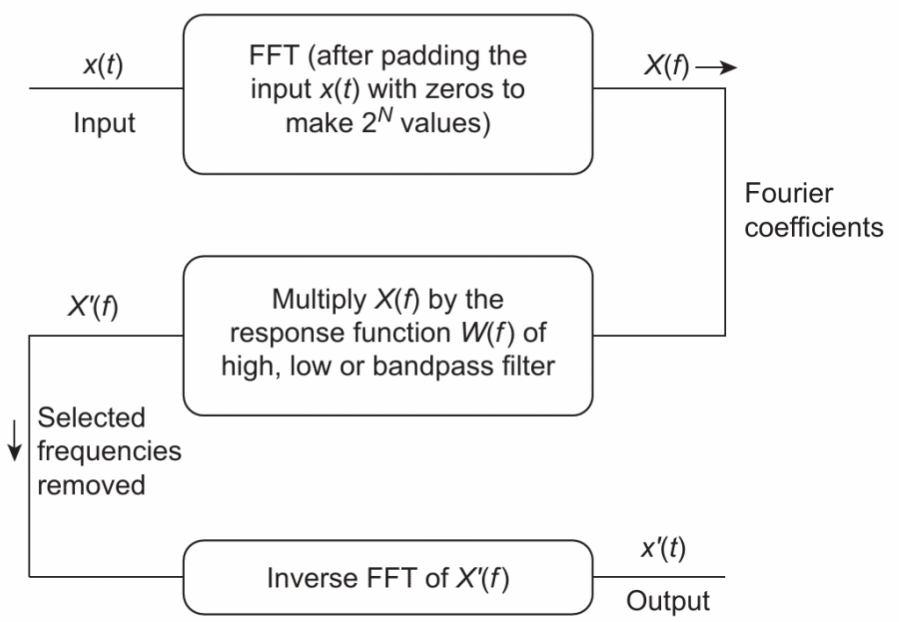

Figure A.1: A schematic representation of the Fourier transform filtering steps. Source: Thomson and Emery (2014).

Transform (IFT) can be written as

$$x_n = \frac{1}{N\Delta t} \sum_{k=0}^{N-1} X_k e^{i2\pi kn/N}, \qquad n = 1, ..., N \tag{A.5}$$

where the Fourier transform , X_k, are specified for the discretized frequencies f_k, and $f_k = kf_1$ with $f_1 = 1/(N\Delta t) = 1/T$ is the fundamental frequency and represents also the bandwidth Δf, for the time series.

The application of the Fourier transform filter can be resumed in the following three steps (Fig. A.1):

1. Take the DFT, $X(f)$ of the original dataset $x(t)$.

2. Multiply $X(f)$ by the appropriate Frequency Response Function (FRF), $W(f)$, of an high, low or bandpass filter.

3. Take the IFT of the results to obtain a filtered dataset in the time domain.

The power of this method is its simplicity. Unlike the filters in the time domain that require a convolution (*e.g.*, Doodson filter, see Eq. 2.2), in the frequency domain what

is required is a simple multiplication

$$X'(f) = W(f)X(f) \tag{A.6}$$

The filtered time series is then simply found applying the IFT to $X'(f)$. However, the form of $W(f)$ is extremely important to have a reliable filter. In the ideal case the FRF should be near unity in the frequency band to be passed and zero in the bands to be stopped, with a narrow transition band to avoid contamination by unwanted frequencies. Unfortunately, a very narrow and steep transition band is the main cause

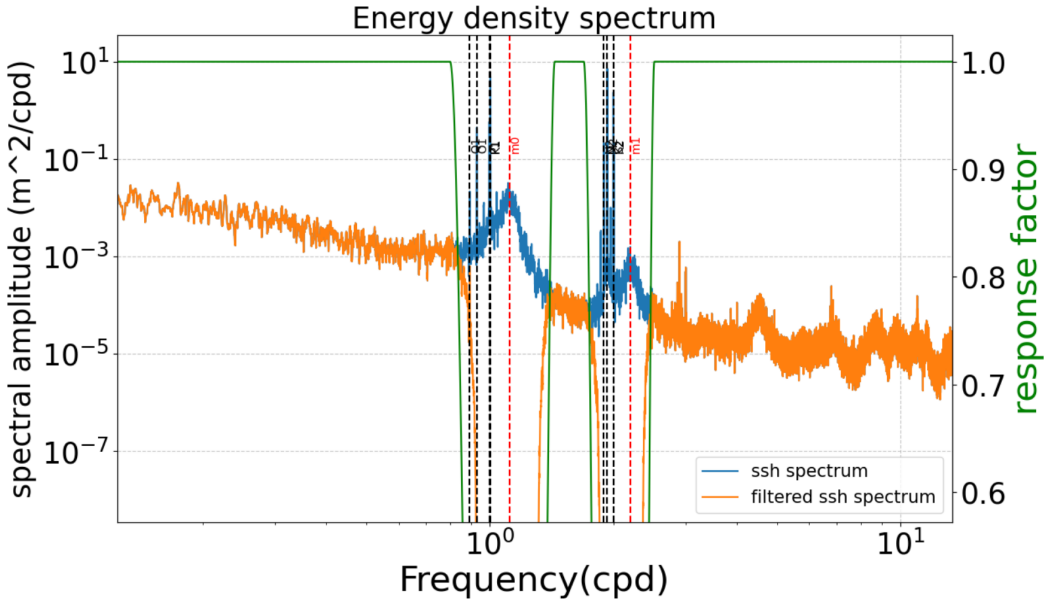

Figure A.2: Energy density spectrum for Faro sea level observations (blue). The filtered dataset is also shown (orange). The green line shows the frequency response function of the filter. Black vertical dashed lines indicate the frequency of major tides. Red dashed lines indicate the frequencies of the fundamental and first mode of the Adriatic sea (seiches).

of large Gibbs' phenomenon, affecting the time series obtained by IFT of $X'(f)$ that manifests itself as large side lobs in the initial and final part of the time series (ringing). The Gibb's phenomenon can be largely reduced by "tapering" the filter ($W(f)$) with a smooth function to ensure a smooth transition to non-zero Fourier coefficients. In this work the transition bands are tapered using a Tukey window (also called cosine-taper)

defined as

$$w(x) = \begin{cases} \frac{1}{2}\left\{1 + \cos\left(\frac{2\pi}{r}\left[x - r/2\right]\right)\right\}, & 0 \leq x < \frac{r}{2} \\ 1, & \frac{r}{2} \leq x < 1 - \frac{r}{2} \\ \frac{1}{2}\left\{1 + \cos\left(\frac{2\pi}{r}\left[x - 1 + r/2\right]\right)\right\}, & 1 - \frac{r}{2} \leq x < 1 \end{cases} \tag{A.7}$$

where x are the L point of the window and the parameter r is the ratio of cosine-tapered section length to the entire window length with $0 < r < 1$. A value $r = 0.5$ produces a Tukey window where half of the entire window length consists of segments of a phase shifted cosine with period $2r = 1$. If $r \leq 0$ a rectangular window is returned while for $r \geq 1$ a Von Hann window is generated (Bloomfield, 2000). The Energy Density Spectrum (EDS) of the observed sea level at Faro is shown in Fig. A.2 together with the EDS of the filtered signal using the Fourier transform filter. The green line is the FRF and was calibrated to exclude tidal and seiches signal from the time series in order to retain the surge component. The resultant time series after the application of the filter is the orange line in Fig. 3.4. The FRF can be easily inverted to isolate the tidal signal and the windows can be moved if there is the need to focus on some particular frequencies (*e.g.*, seiches). On the other side the initial and final part of the time series must be excluded because they are the most affected by the Gibbs' phenomenon. If in time domain filters the initial and final part of the time series are naturally excluded, in frequency domain filters there is no a clear threshold, and the part of time series to exclude is a subjective choice. However, Walters and Heston (1982) suggests that in both time domain and frequency domain filters the same amount of data are lost. The version of the tidal filter used for this work can be found at the Zenodo repository of the Oceanography group of the University of Bologna at the link: `https://doi.org/10.5281/zenodo.6478113`.

List of Acronyms

Arpae Agency for Prevention, Environment and Energy of Emilia-Romagna 21

BMA Bayesian Model Average 56

CMCC Euro-Mediterranean center for climate change 9

CMEMS Copernicus Marine Environment Monitoring Service 59

DFT Discrete Fourier Transform 123

ECMWF European Centre for Medium-range Weather Forecasting 55

EDS Energy Density Spectrum 126

EM Ensemble Mean 51

EMDW Eastern Mediterranean Deep Water 4

EMT Eastern Mediterranean Transient 3

KE Kinetic Energy 65

LHS Left Hand Side

MAd Middle Adriatic

MADW Middle Adriatic Dense Water 3

MAE Mean Absolute Error 29

MFS Mediterranean Forecasting System 59

MPI Message Passing Interface 90

MLIW Modified Levantine Intermediate Waters 3

NAd Northern Adriatic

NAdDW North Adriatic Dense Water 3

NBS Nature-Based Solution 15

NEMO Nucleus for European Modelling of the Ocean 59

NMC National Meteorological Centre 55

UN United Nations 14

UNESCO United Nations Educational, Scientific and Cultural Organization 11

WACC Western Adriatic Coastal Current 4

WEM Weighted Ensemble Mean 51

W-MAd Western Middle Adriatic

WRT Water Renewal Time 40

W-SAd Western Southern Adriatic

References

F. Adloff, G. Jordà, S. Somot, F. Sevault, T. Arsouze, B. Meyssignac, L. Li, and S. Planton. Improving sea level simulation in mediterranean regional climate models. *Climate Dynamics*, 51(3):1167–1178, Aug. 2017. doi:10.1007/s00382-017-3842-3. 113

C. Armaroli, P. Ciavola, M. Masina, and L. Perini. Run-up computation behind emerged breakwaters for marine storm risk assessment. *J. Coastal Res.*, SI 56:1612–1616, 2009. 53, 80

Arpa-Veneto. Agenzia regionale per la prevenzione e protezione ambientale del veneto, dipartimento regionale per la sicurezza del territorio. sulla ripartizione delle portate del po tra i vari rami e le bocche a mare del delta: esperienze storiche e nuove indagini all'anno 2011. relazione 02/2012, 2012. Vicenza: Arpa Veneto. 22, 99

Arpae. Agenzia regionale per la prevenzione, l'ambiente e l'energia dell'emilia romagna, struttura idro-meteo-clima, servizio idrografia e idrologia regionale e distretto po. annali idrologici 2018, parte seconda, 2018. Bologna: Arpae. 22

A. Artegiani, D. Bregant, E. Paschini, N. Pinardi, F. Raicich, and A. Russo. The adriatic sea general circulation. part i: air–sea interactions and water mass structure. *Journal of Physical Oceanography*, 27(8):1492–1514, aug 1997a. doi:10.1175/1520-0485(1997)027<1492:tasgcp>2.0.co;2. 1, 2, 3

A. Artegiani, D. Bregant, E. Paschini, N. Pinardi, F. Raicich, and A. Russo. The adriatic sea general circulation. part II: baroclinic circulation structure. *Journal of Physical Oceanography*, 27(8):1515–1532, aug 1997b. doi:10.1175/1520-0485(1997)027<1515:tasgcp>2.0.co;2. 1, 4, 5

M. Bajo, I. Međugorac, G. Umgiesser, and M. Orlić. Storm surge and seiche modelling

in the adriatic sea and the impact of data assimilation. *Quarterly Journal of the Royal Meteorological Society*, 145(722):2070–2084, May 2019. doi:10.1002/qj.3544. 54

J. V. L. Beckers, E. Sprokkereef, and K. L. Roscoe. Use of bayesian model averaging to determine uncertainties in river discharge and water level forecasts. 2008. In: proc. 4th International Symposium on Flood Defence: Managing Flood Risk, Reliability and Vulnerability, Toronto, Ontario, Canada. 56

D. Bellafiore and G. Umgiesser. Hydrodynamic coastal processes in the north adriatic investigated with a 3d finite element model. *Ocean Dynamics*, 60(2):255–273, Dec. 2009. doi:10.1007/s10236-009-0254-x. 8

D. Bellafiore, C. Ferrarin, F. Braga, L. Zaggia, F. Maicu, G. Lorenzetti, G. Manfè, V. Brando, and F. D. Pascalis. Coastal mixing in multiple-mouth deltas: a case study in the po delta, italy. *Estuar. Coast. Shelf Sci.*, 226:106254, Oct. 2019. doi:10.1016/j.ecss.2019.106254. 36

D. Bellafiore, C. Ferrarin, F. Maicu, G. Manfè, G. Lorenzetti, G. Umgiesser, L. Zaggia, and A. V. Levinson. Saltwater intrusion in a mediterranean delta under a changing climate. *Estuar. Coast. Shelf Sci.*, 126(2), Feb. 2021. doi:10.1029/2020jc016437. 25

A. Bergamasco and M. Gačić. Baroclinic response of the adriatic sea to an episode of bora wind. *Journal of Physical Oceanography*, 26(7):1354–1369, jul 1996. doi:10.1175/1520-0485(1996)026<1354:brotas>2.0.co;2. 6

A. Beudin, T. S. Kalra, N. K. Ganju, and J. C. Warner. Development of a coupled wave-flow-vegetation interaction model. *Computers & Geosciences*, 100:76–86, Mar. 2017. doi:10.1016/j.cageo.2016.12.010. 88, 89, 90, 95, 96, 97, 106

A. Bezzi, G. Casagrande, D. Martinucci, S. Pillon, C. D. Grande, and G. Fontolan. Modern sedimentary facies in a progradational barrier-spit system: Goro lagoon, po delta, italy. *Estuarine, Coastal and Shelf Science*, 227:106323, Oct. 2019. doi:10.1016/j.ecss.2019.106323. 19

P. Billi and M. Fazzini. Global change and river flow in italy. *Global and Planetary Change*, 155:234–246, Aug. 2017. doi:10.1016/j.gloplacha.2017.07.008. 82

G. Bitelli, F. Bonsignore, S. D. Conte, F. Franci, A. Lambertini, F. Novali, P. Severi, and L. Vittuari. Updating the subsidence map of emilia-romagna region (italy) by integration

of SAR interferometry and GNSS time series: the 2011–2016 period. *Proceedings of the International Association of Hydrological Sciences*, 382:39–44, Apr. 2020. doi:10.5194/piahs-382-39-2020. 81

P. Bloomfield. *Fourier analysis of time series.* John Wiley & Sons, Inc., Jan. 2000. doi:10.1002/0471722235. 126

A. F. Blumberg and G. L. Mellor. A description of a three-dimensional coastal ocean circulation model. In *Three-Dimensional Coastal Ocean Models*, pages 1–16. American Geophysical Union, 1987. doi:10.1029/co004p0001. 9

M. Bondesan, G. B. Castiglioni, C. Elmis, G. Gabbianellis, R. Marocco, P. A. Pirazzoli, and A. Tomasin. Coastal areas at risk from storm surges and sea-level rise in northeastern italy. *Journal of coastal research*, 11(4):1354–1379, 1995. 54

N. Booij, R. C. Ris, and L. H. Holthuijsen. A third-generation wave model for coastal regions: 1. model description and validation. *Journal of Geophysical Research: Oceans*, 104(C4): 7649–7666, Apr. 1999. doi:10.1029/98jc02622. 59

J. Borum, C. Duarte, and D. Krause-Jensen. *European seagrasses: an introduction to monitoring and management.* SEAGRASSES dot ORG, 2004. 86

F. Boscutti, I. Marcorin, M. Sigura, E. Bressan, F. Tamberlich, A. Vianello, and V. Casolo. Distribution modeling of seagrasses in brackish waters of grado-marano lagoon (northern adriatic sea). *Estuarine, Coastal and Shelf Science*, 164:183–193, Oct. 2015. doi:10.1016/j.ecss.2015.07.035. 85, 87, 100

M. C. Buia and M. Marzocchi. Dinamica dei sistemi a cymodocea nodosa, zostera marina e zostera noltii nel mediterraneo. *Giornale botanico italiano*, 129(1):319–336, Jan. 1995. doi:10.1080/11263509509436148. 86

H. Burchard and H. Baumert. The formation of estuarine turbidity maxima due to density effects in the salt wedge. a hydrodynamic process study. *J. Phys. Oceanogr.*, 28(2):309–321, Feb. 1998. doi:10.1175/1520-0485(1998)028<0309:tfoetm>2.0.co;2. 39, 93

H. Burchard, K. Bolding, and M. Villareal. Gotm - a general ocean turbulence model. theory, applications and test cases. Technical report, European Commission, 1999. European commission report EUR. 11, 91, 93

R. Carafa, D. Marinov, S. Dueri, J. Wollgast, J. Ligthart, E. Canuti, P. Viaroli, and J. Zaldívar. A 3d hydrodynamic fate and transport model for herbicides in sacca di goro coastal lagoon (northern adriatic). *Marine Pollution Bulletin*, 52(10):1231–1248, Oct. 2006. doi:10.1016/j.marpolbul.2006.02.025. 20

L. Carrere, F. Lyard, M. Cancet, and A. Guillot. Fes 2014, a new tidal model on the global ocean with enhanced accuracy in shallow seas and in the arctic region. In *EGU General Assembly Conference Abstracts*, EGU General Assembly Conference Abstracts, page 5481, Apr. 2015. 60

L. Cavaleri, A. Lavagnini, and S. Martorelli. The wind climatology of the adriatic sea deduced from coastal stations. *Nuovo Cimento*, 19:37–50, 1996. 6

L. Cavicchia, S. Gualdi, A. Sanna, and P. Oddo. The regional ocean-atmosphere coupled model cosmo-nemo_mfs. *CMCC Research Paper (RP0254)*, 44, Apr. 2015. 101

L. Cavicchia, E. Scoccimarro, S. Gualdi, P. Marson, B. Ahrens, S. Berthou, D. Conte, A. Dell'Aquila, P. Drobinski, V. Djurdjevic, C. Dubois, C. Gallardo, L. Li, P. Oddo, A. Sanna, and C. Torma. Mediterranean extreme precipitation: a multi-model assessment. *Climate Dynamics*, 51(3):901–913, June 2016. doi:10.1007/s00382-016-3245-x. 101

I. Cerovečki, M. Orlić, and M. C. Hendershott. Adriatic seiche decay and energy loss to the mediterranean. *Deep Sea Research Part I: Oceanographic Research Papers*, 44(12): 2007–2029, Dec. 1997. doi:10.1016/s0967-0637(97)00056-3. 54

E. Chaumillon, X. Bertin, A. B. Fortunato, M. Bajo, J.-L. Schneider, L. Dezileau, J. P. Walsh, A. Michelot, E. Chauveau, A. Créach, A. Hénaff, T. Sauzeau, B. Waeles, B. Gervais, G. Jan, J. Baumann, J.-F. Breilh, and R. Pedreros. Storm-induced marine flooding: Lessons from a multidisciplinary approach. *Earth-Science Reviews*, 165:151–184, Feb. 2017. doi:10.1016/j.earscirev.2016.12.005. 51

J. Chiggiato and P. Oddo. Operational ocean models in the adriatic sea: a skill assessment. *Ocean Sci.*, 4(1):61–71, Feb. 2008. doi:10.5194/os-4-61-2008. 26

J. Chiggiato, M. Zavatarelli, S. Castellari, and M. Deserti. Interannual variability of surface heat fluxes in the adriatic sea in the period 1998–2001 and comparison

with observations. *Science of The Total Environment*, 353(1-3):89–102, Dec. 2005. doi:10.1016/j.scitotenv.2005.09.031. 2

P. C. Chu. Fundamental problems in coastal ocean prediction. *Proceedings of Oceanology International 99*, pages 37–46, 1999. 55

P. Ciavola, C. Armaroli, J. Chiggiato, A. Valentini, M. Deserti, L. Perini, and P. Luciani. Impact of storms along the coastline of emilia-romagna: the morphological signature on the ravenna coastline (italy). *J. Coastal Res.*, SI 50:540–544, 2007. 54, 80

E. Clementi, P. Oddo, M. Drudi, N. Pinardi, G. Korres, and A. Grandi. Coupling hydrodynamic and wave models: first step and sensitivity experiments in the mediterranean sea. *Ocean Dynamics*, 67(10):1293–1312, July 2017. doi:10.1007/s10236-017-1087-7. 26, 59

E. Clementi, A. C. Goglio, A. Aydogdu, J. Pistoia, R. Escudier, M. Drudi, A. Grandi, A. Mariani, V. Lyubartsev, R. Lecci, S. Cretí, S. Masina, G. Coppini, and N. Pinardi. The new mediterranean sea analysis and forecasting system including tides: description and validation. Mar. 2021. doi:10.5194/egusphere-egu21-13531. 59

E. Cohen-Shacham, G. Walters, C. Janzen, and S. Maginnis. *Nature-based solutions to address global societal challenges*. IUCN International Union for Conservation of Nature, Aug. 2016. doi:10.2305/iucn.ch.2016.13.en. 83, 84

COSMO-newsletter. Operational applications - arpa-sim (bologna). Technical Report 25-26, Deutsch. WetterDienst (DWD) Offenbach 6, 2004. 26, 59

A. Cucco and G. Umgiesser. Modelling the venice lagoon residence time. *Ecol. Model.*, 193 (1-2):34–51, Mar. 2006. doi:10.1016/j.ecolmodel.2005.07.043. 40

D. Curiel, S. K. Pavelić, A. Kovačev, C. Miotti, and A. Rismondo. Marine seagrasses transplantation in confined and coastal adriatic environments: methods and results. *Water*, 13 (16):2289, Aug. 2021. doi:10.3390/w13162289. 87

B. Cushman-Roisin, V. Malačič, and M. Gačić. Tides, seiches and low-frequency oscillations. In *Physical Oceanography of the Adriatic Sea*, pages 217–240. Springer Netherlands, 2001. doi:10.1007/978-94-015-9819-4_7. 7

V. Damiani, C. Bianchi, O. Ferretti, D. Bedulli, C. Morri, M. Viel, and G. Zurlini. Risultati di una ricerca ecologica sul sistema marino costiero pugliese. *Thalassia Salentina*, 18:153–169, 1988. doi:10.1285/i15910725v18p153. 86

R. Danovaro, E. Nepote, M. L. Martire, L. Carugati, Z. D. Ros, F. Torsani, A. Dell'Anno, and C. Corinaldesi. Multiple declines and recoveries of adriatic seagrass meadows over forty years of investigation. *Marine Pollution Bulletin*, 161:111804, Dec. 2020. doi:10.1016/j.marpolbul.2020.111804. 87, 100

A. Defant. *Physical oceanography*. 1961. vol. 2, 729 pp., Pergamon, Tarrytown, N.Y. 7

J. T. Dijkstra and R. E. Uittenbogaard. Modeling the interaction between flow and highly flexible aquatic vegetation. *Water Resources Research*, 46(12), Dec. 2010. doi:10.1029/2010wr009246. 87

S. Dobricic and N. Pinardi. An oceanographic three-dimensional variational data assimilation scheme. *Ocean Modelling*, 22(3-4):89–105, Jan. 2008. doi:10.1016/j.ocemod.2008.01.004. 59

A. T. Doodson. The analysis of tidal observations. *Philosophical Transactions of the Royal Society of London. Series A*, 227(647-658):223–279, Jan. 1928. doi:10.1098/rsta.1928.0006. 27

N. Droste, C. Schröter-Schlaack, B. Hansjürgens, and H. Zimmermann. Implementing nature-based solutions in urban areas: financing and governance aspects. In *Theory and Practice of Urban Sustainability Transitions*, pages 307–321. Springer International Publishing, 2017. doi:10.1007/978-3-319-56091-5_18. 85

G. D. Egbert and S. Y. Erofeeva. Efficient inverse modelling of barotropic ocean tides. *J. Atmosph. Oceanic Technol.*, 19(2):183–204, Feb. 2002. doi:10.1175/1520-0426(2002)019<0183:eimobo>2.0.co;2. 28, 59, 99

K. Emanuel. Will global warming make hurricane forecasting more difficult? *Bulletin of the American Meteorological Society*, 98(3):495–501, Mar. 2017. doi:10.1175/bams-d-16-0134.1. 52

F. M. Falcieri, A. Benetazzo, M. Sclavo, A. Russo, and S. Carniel. Po river plume pattern variability investigated from model data. *Contin. Shelf Res.*, 87:84–95, Sept. 2014. doi:10.1016/j.csr.2013.11.001. 36

I. Federico, N. Pinardi, G. Coppini, P. Oddo, R. Lecci, and M. Mossa. Coastal ocean forecasting with an unstructured grid model in the southern adriatic and northern ionian seas. *Natural Hazards and Earth System Sciences*, 17(1):45–59, Jan. 2017. doi:10.5194/nhess-17-45-2017. 64

C. Ferrarin, A. Valentini, M. Vodopivec, D. Klaric, G. Massaro, M. Bajo, F. D. Pascalis, A. Fadini, M. Ghezzo, S. Menegon, L. Bressan, S. Unguendoli, A. Fettich, J. Jerman, M. Ličer, L. Fustar, A. Papa, and E. Carraro. Integrated sea storm management strategy: the 29 october 2018 event in the adriatic sea. *Natural Hazards and Earth System Sciences*, 20(1):73–93, Jan. 2020. doi:10.5194/nhess-20-73-2020. 56

C. Ferrarin, M. Bajo, A. Benetazzo, L. Cavaleri, J. Chiggiato, S. Davison, S. Davolio, P. Lionello, M. Orlić, and G. Umgiesser. Local and large-scale controls of the exceptional venice floods of november 2019. *Progress in Oceanography*, 197:102628, sep 2021. doi:10.1016/j.pocean.2021.102628. 7

E. Fischer-Piette, R. Heim, and R. Lami. Note preliminaire sur une maladie bacterienne des zosteres. *Comptes Rendus Hebdomadaires des Sciences de l'Academie des Sciences*, 195: 1420–1422, 1932. 85

J. Flowerdew, K. Horsburgh, and K. Mylne. Ensemble forecasting of storm surges. *Marine Geodesy*, 32(2):91–99, May 2009. doi:10.1080/01490410902869151. URL `https://doi.org/10.1080/01490410902869151`. 56

J. Flowerdew, K. Horsburgh, C. Wilson, and K. Mylne. Development and evaluation of an ensemble forecasting system for coastal storm surges. *Quarterly Journal of the Royal Meteorological Society*, 136(651):1444–1456, July 2010. doi:10.1002/qj.648. 56

N. Fofonoff and M. J. R.C. Algorithms for the computation of fundamental properties of seawater., 1983. 11

M. Fonseca, J. Fisher, J. Zieman, and G. Thayer. Influence of the seagrass, zostera ma-

rina l., on current flow. *Estuarine, Coastal and Shelf Science*, 15(4):351–364, Oct. 1982. doi:10.1016/0272-7714(82)90046-4. 87

M. S. Fonseca and J. A. Cahalan. A preliminary evaluation of wave attenuation by four species of seagrass. *Estuarine, Coastal and Shelf Science*, 35(6):565–576, Dec. 1992. doi:10.1016/s0272-7714(05)80039-3. 87

M. S. Fonseca, J. W. Fourqurean, and M. A. R. Koehl. Effect of seagrass on current speed: importance of flexibility vs. shoot density. *Frontiers in Marine Science*, 6, July 2019. doi:10.3389/fmars.2019.00376. 87

A. M. G. Forbes. Fourier transform filtering: a cautionary note. *Journal of Geophysical Research*, 93(C6):6958, 1988. doi:10.1029/jc093ic06p06958. 123

V. Fortin, M. Abaza, F. Anctil, and R. Turcotte. Why should ensemble spread match the RMSE of the ensemble mean? *Journal of Hydrometeorology*, 15(4):1708–1713, July 2014. doi:10.1175/jhm-d-14-0008.1. 68

G. Forzieri, L. Feyen, S. Russo, M. Vousdoukas, L. Alfieri, S. Outten, M. Migliavacca, A. Bianchi, R. Rojas, and A. Cid. Multi-hazard assessment in europe under climate change. *Climatic Change*, 137(1-2):105–119, Apr. 2016. doi:10.1007/s10584-016-1661-x. 51

M. G. Gaeta, A. G. Samaras, I. Federico, R. Archetti, F. Maicu, and G. Lorenzetti. A coupled wave 3-d hydrodynamics model of the taranto sea (italy): a multiple-nesting approach. *Natural Hazards and Earth System Sciences*, 16(9):2071–2083, Sept. 2016. doi:10.5194/nhess-16-2071-2016. 65

G. Galassi and G. Spada. Linear and non-linear sea-level variations in the adriatic sea from tide gauge records (1872-2012). *Annals of Geophysics*, 57(6), Mar. 2015. doi:10.4401/ag-6536. 81

V. Gallina, S. Torresan, A. Zabeo, J. Rizzi, S. Carniel, M. Sclavo, L. Pizzol, A. Marcomini, and A. Critto. Assessment of climate change impacts in the north adriatic coastal area. part II: consequences for coastal erosion impacts at the regional scale. *Water*, 11(6):1300, June 2019. doi:10.3390/w11061300. 79

G. Gambolati and P. Teatini. Numerical analysis of land subsidence due to natural compaction of the upper adriatic sea basin. In *CENAS*, pages 103–131. Springer Netherlands, 1998. doi:10.1007/978-94-011-5147-4_5. 80

F. Ganthy, R. Verney, and A. Sottolichio. A numerical investigation on the effects of small and flexible seagrass zostera noltii on water flow. *Proc Coast Dyn*, 2013:705–716, 2013. 88

E. Garnier, P. Ciavola, T. Spencer, O. Ferreira, C. Armaroli, and A. McIvor. Historical analysis of storm events: case studies in france, england, portugal and italy. *Coastal Engineering*, 134:10–23, Apr. 2018. doi:10.1016/j.coastaleng.2017.06.014. 54

G. Godin and L. Trotti. *Trieste, water levels 1952-1971: a study of the tide, mean level and seiche activity*, volume 28. Miscellaneous Special Publcation, 1975. Ottawa. 54

E. Grottoli, S. Cilli, P. Ciavola, and C. Armaroli. Sedimentation at river mouths bounded by coastal structures: a case study along the emilia-romagna coastline, italy. *Journal of Coastal Research*, 95(sp1):505, May 2020. doi:10.2112/si95-098.1. 79

M. D. Harley, A. Valentini, C. Armaroli, P. Ciavola, L. Perini, L. Calabrese, and F. Marucci. An early warning system for the on-line prediction of coastal storm risk on the italian coastline. *Coastal Engineering Proceedings*, 1(33):77, Dec. 2012. doi:10.9753/icce.v33.management.77. 80

S. Hellerman and M. Rosenstein. Normal monthly wind stress over the world ocean with error estimates. *Journal of Physical Oceanography*, 13(7):1093–1104, July 1983. doi:10.1175/1520-0485(1983)013<1093:nmwsot>2.0.co;2. 12

D. Idier, X. Bertin, P. Thompson, and M. D. Pickering. Interactions between mean sea level, tide, surge, waves and flooding: mechanisms and contributions to sea level variations at the coast. *Surveys in Geophysics*, 40(6):1603–1630, June 2019. doi:10.1007/s10712-019-09549-5. 53

IPCC. Climate change 2013: the physical science basis. contribution of working group i to the fifth assessment report of the intergovernmental panel on climate change, 2013. Cambridge: Cambridge University Press. 19, 81, 100

IPCC. Climate change 2021: the physical science basis. contribution of working group i to the sixth assessment report of the intergovernmental panel on climate change, 2021. Cambridge: Cambridge University Press. 81

Istituto-Delta-Ecologia-Applicata. Relazione finale-studio delle potenzialità produttive della sacca di goro, 2004. Ferrara: Istituto Delta Ecologia Applicata. 46

D. A. Jay and J. D. Musiak. *Internal tidal asymmetry in channel flows: origins and consequences*, chapter 13, pages 211–249. American Geophysical Union (AGU), 1996. ISBN 9781118665220. doi:https://doi.org/10.1029/CE050p0211. 38, 40

M. A. Jeffries and C. M. Lee. A climatology of the northern adriatic sea's response to bora and river forcing. *J. Geophys. Res. Oceans.*, 112(C3), Mar. 2007. doi:10.1029/2006jc003664. 36

N. G. Jerlov. *Marine Optics*. Copenhagen: Elsevier oceanography series, 1976. 28

E. Kirezci, I. R. Young, R. Ranasinghe, S. Muis, R. J. Nicholls, D. Lincke, and J. Hinkel. Projections of global-scale extreme sea levels and resulting episodic coastal flooding over the 21st century. *Scientific Reports*, 10(1), July 2020. doi:10.1038/s41598-020-67736-6. 62

A. Kolmogorov. The local structure of turbulence in incompressible viscous fluid for very large reynolds numbers. *Akademiia Nauk SSSR Doklady*, 30:301–305, Jan. 1941. 11

T. N. Krishnamurti, C. M. Kishtawal, Z. Zhang, T. LaRow, D. Bachiochi, E. Williford, S. Gadgil, and S. Surendran. Multimodel ensemble forecasts for weather and seasonal climate. *Journal of Climate*, 13(23):4196–4216, Dec. 2000. doi:10.1175/1520-0442(2000)013<4196:meffwa>2.0.co;2. 55

J. R. Lacy and S. Wyllie-Echeverria. The influence of current speed and vegetation density on flow structure in two macrotidal eelgrass canopies. *Limnology and Oceanography: Fluids and Environments*, 1(1):38–55, Feb. 2011. doi:10.1215/21573698-1152489. 87

S. Lange, B. Rockel, J. Volkholz, and B. Bookhagen. Regional climate model sensitivities to parametrizations of convection and non-precipitating subgrid-scale clouds over south america. *Climate Dynamics*, 44(9-10):2839–2857, June 2014. doi:10.1007/s00382-014-2199-0. 101

J.-M. Lellouche, E. Greiner, O. L. Galloudec, G. Garric, C. Regnier, M. Drevillon, M. Benkiran, C.-E. Testut, R. Bourdalle-Badie, F. Gasparin, O. Hernandez, B. Levier, Y. Drillet, E. Remy, and P.-Y. L. Traon. Recent updates to the copernicus marine service global ocean monitoring and forecasting real-time 1â12 high-resolution system. *Ocean Science*, 14(5):1093–1126, Sept. 2018. doi:10.5194/os-14-1093-2018. 60

T. D. Liberto, B. A. Colle, N. Georgas, A. F. Blumberg, and A. A. Taylor. Verification of a multimodel storm surge ensemble around new york city and long island for the cool season. *Weather and Forecasting*, 26(6):922–939, Dec. 2011. doi:10.1175/waf-d-10-05055.1. 56

P. Lionello, D. Barriopedro, C. Ferrarin, R. J. Nicholls, M. Orlić, F. Raicich, M. Reale, G. Umgiesser, M. Vousdoukas, and D. Zanchettin. Extreme floods of venice: characteristics, dynamics, past and future evolution (review article). *Natural Hazards and Earth System Sciences*, 21(8):2705–2731, Sept. 2021. doi:10.5194/nhess-21-2705-2021. 53, 54

M. Longuet-Higgins and R. Stewart. Radiation stresses in water waves; a physical discussion, with applications. *Deep Sea Research and Oceanographic Abstracts*, 11(4):529–562, Aug. 1964. doi:10.1016/0011-7471(64)90001-4. 53

E. N. Lorenz. Deterministic nonperiodic flow. *Journal of the Atmospheric Sciences*, 20(2): 130–141, Mar. 1963. doi:10.1175/1520-0469(1963)020<0130:dnf>2.0.co;2. 55

S. Lorito, L. Calabrese, L. Perini, and U. Cibin. *Uso del suolo della costa, Il sistema mare-costa dell'Emilia-Romagna*. 2010. 81

W. Ludwig, E. Dumont, M. Meybeck, and S. Heussner. River discharges of water and nutrients to the mediterranean and black sea: Major drivers for ecosystem changes during past and future decades? *Progr. Oceanogr.*, 80(3-4):199–217, Mar. 2009. doi:10.1016/j.pocean.2009.02.001. 25

M. Luhar and H. M. Nepf. Flow-induced reconfiguration of buoyant and flexible aquatic vegetation. *Limnology and Oceanography*, 56(6):2003–2017, Sept. 2011. doi:10.4319/lo.2011.56.6.2003. 88, 90

G. Madec. *NEMO ocean engine*. 2008. Note du Pôle de modélisation, Institut Pierre-Simon Laplace (IPSL), France, No 27, ISSN No 1288-1619. 59

A. Maggiore, M. Zavatarelli, M. Angelucci, and N. Pinardi. Surface heat and water fluxes in the adriatic sea: seasonal and internanual variability. *Physics and Chemistry of the Earth*, 23(5-6):561–567, Jan. 1998. doi:10.1016/s0079-1946(98)00070-6. 2

F. Maicu, F. D. Pascalis, C. Ferrarin, and G. Umgiesser. Hydrodynamics of the po river-delta-sea system. *J. Geophys. Res. Oceans.*, 123(9):6349–6372, Sept. 2018. doi:10.1029/2017jc013601. 21, 30, 36

F. Maicu, J. Alessandri, N. Pinardi, G. Verri, G. Umgiesser, S. Lovo, S. Turolla, T. Paccagnella, and A. Valentini. Downscaling with an unstructured coastal-ocean model to the goro lagoon and the po river delta branches. *Front. Mar. Sci.*, 8:647781, 2021. doi:10.3389/fmars.2021.647781. 17, 18, 23, 30, 34, 36, 37, 41, 42, 43, 44, 47, 48, 56

V. Malačič, D. Viezzoli, and B. Cushman-Roisin. Tidal dynamics in the northern adriatic sea. *J. Geophys. Res. Oceans*, 105(C11):26265–26280, Nov. 2000. doi:10.1029/2000jc900123. 8, 52

P. Malanotte-Rizzoli. The northern adriatic sea as a prototype of convection and water mass formation on the continental shelf. In *Elsevier Oceanography Series*, pages 229–239. Elsevier, 1991. doi:10.1016/s0422-9894(08)70070-9. 3

B. Manca, V. Kovaĉević, M. Gaĉić, and D. Viezzoli. Dense water formation in the southern adriatic sea and spreading into the ionian sea in the period 1997–1999. *Journal of Marine Systems*, 33-34:133–154, June 2002. doi:10.1016/s0924-7963(02)00056-8. 3

D. Marinov, A. Norro, and J.-M. Zaldívar. Application of COHERENS model for hydrodynamic investigation of sacca di goro coastal lagoon (italian adriatic sea shore). *Ecological Modelling*, 193(1-2):52–68, Mar. 2006. doi:10.1016/j.ecolmodel.2005.07.042. 20

D. Marinov, J. M. Zaldívar, A. Norro, G. Giordani, and P. Viaroli. Integrated modelling in coastal lagoons: Sacca di goro case study. *Hydrobiologia*, 611(1):147–165, July 2008. doi:10.1007/s10750-008-9451-8. 20, 23

M. Maza, J. L. Lara, and I. J. Losada. A coupled model of submerged vegetation under oscillatory flow using navier–stokes equations. *Coastal Engineering*, 80:16–34, Oct. 2013. doi:10.1016/j.coastaleng.2013.04.009. 83

L. Mazzella, P. Guidetti, M. Lorenti, M. Buia, V. Zupo, M. Scipione, A. Rismondo, and D. Curiel. Biomass partitioning in adriatic seagrass ecosystems (posidonia oceanica, cymodocea nodosa, zostera marina). *Rapp. Comm. Int. Mer Mediterr.*, 35:562–563, 1998. 90

I. P. Medvedev, I. Vilibić, and A. B. Rabinovich. Tidal esonance in the adriatic sea: observational evidence. *Journal of Geophysical Research: Oceans*, 125(8), Aug. 2020. doi:10.1029/2020jc016168. 8

G. Micaletto, I. Barletta, S. Mocavero, I. Federico, I. Epicoco, G. Verri, G. Coppini, P. Schiano, G. Aloisio, and N. Pinardi. Parallel implementation of the SHYFEM model. Nov. 2021. doi:10.5194/gmd-2021-319. submitted. 8, 90

R. F. Milliff, A. Bonazzi, C. K. Wikle, N. Pinardi, and L. M. Berliner. Ocean ensemble forecasting. part i: ensemble mediterranean winds from a bayesian hierarchical model. *Quarterly Journal of the Royal Meteorological Society*, 137(657):858–878, Apr. 2011. doi:10.1002/qj.767. 55

J. D. Milliman, D. Bonaldo, and S. Carniel. Flux and fate of river-discharged sediments to the adriatic sea. *Advances in Oceanography and Limnology*, 1(1S), Nov. 2016. doi:10.4081/aiol.2016.5899. 79

F. Molteni, R. Buizza, T. N. Palmer, and T. Petroliagis. The ECMWF ensemble prediction system: methodology and validation. *Quarterly Journal of the Royal Meteorological Society*, 122(529):73–119, Jan. 1996. doi:10.1002/qj.49712252905. 55

J. Morin, M. Leclerc, Y. Secretan, and P. Boudreau. Integrated two-dimensional macrophytes-hydrodynamic modeling. *Journal of Hydraulic Research*, 38(3):163–172, May 2000. doi:10.1080/00221680009498334. 88

H. M. Nepf. Flow and transport in regions with aquatic vegetation. *Annual Review of Fluid Mechanics*, 44(1):123–142, Jan. 2012. doi:10.1146/annurev-fluid-120710-101048. 88

H. M. Nepf and E. R. Vivoni. Flow structure in depth-limited, vegetated flow. *Journal of Geophysical Research: Oceans*, 105(C12):28547–28557, Dec. 2000. doi:10.1029/2000jc900145. 87, 88, 89

C. Nesshöver, T. Assmuth, K. N. Irvine, G. M. Rusch, K. A. Waylen, B. Delbaere, D. Haase, L. Jones-Walters, H. Keune, E. Kovacs, K. Krauze, M. Külvik, F. Rey, J. van Dijk, O. I. Vistad, M. E. Wilkinson, and H. Wittmer. The science, policy and practice of nature-based solutions: an interdisciplinary perspective. *Science of The Total Environment*, 579: 1215–1227, Feb. 2017. doi:10.1016/j.scitotenv.2016.11.106. 84

F. Nevens, N. Frantzeskaki, L. Gorissen, and D. Loorbach. Urban transition labs: co-creating transformative action for sustainable cities. *Journal of Cleaner Production*, 50:111–122, July 2013. doi:10.1016/j.jclepro.2012.12.001. 84

P. Oddo and A. Guarnieri. A study of the hydrographic conditions in the adriatic sea from numerical modelling and direct observations (2000–2008). *Ocean Science*, 7(5):549–567, Sept. 2011. doi:10.5194/os-7-549-2011. 2, 3

P. Oddo, N. Pinardi, and M. Zavatarelli. A numerical study of the interannual variability of the adriatic sea (2000–2002). *Science of The Total Environment*, 353(1-3):39–56, dec 2005. doi:10.1016/j.scitotenv.2005.09.061. 2, 4

P. Oddo, M. Adani, N. Pinardi, C. Fratianni, M. Tonani, and D. Pettenuzzo. A nested atlantic-mediterranean sea general circulation model for operational forecasting. *Ocean Science*, 5(4):461–473, Oct. 2009. doi:10.5194/os-5-461-2009. 101

OECD. *Responding to rising seas*. 2019. doi:10.1787/9789264312487-en. 52

J. O'Kane, M. Suppo, E. Todini, and J. Turner. Physical intervention in the lagoon of sacca di goro. an examination using a 3-d numerical model. In *Marine Coastal Eutrophication*, pages 489–510. Elsevier, 1992. doi:10.1016/b978-0-444-89990-3.50046-8. 20

B. Ondiviela, I. J. Losada, J. L. Lara, M. Maza, C. Galván, T. J. Bouma, and J. van Belzen. The role of seagrasses in coastal protection in a changing climate. *Coastal Engineering*, 87: 158–168, May 2014. doi:10.1016/j.coastaleng.2013.11.005. 85, 86, 88

M. Orlić. About a possible occurrence of the proudman resonance in the adriatic. *Thalassia Jugoslavica*, 16:79–88, 1980. 54

M. Orlić, M. Kuzmić, and Z. Pasarić. Response of the adriatic sea to the bora and sirocco forcing. *Contin. Shelf Res.*, 14(1):91–116, Jan. 1994. doi:10.1016/0278-4343(94)90007-8. 6, 36, 53

I. Ovchinnikov, V. Zats, V. Krvosheia, and A. Udodov. Formation of deep eastern mediterranean waters in the adriatic sea. *Oceanology*, 25(6):704–707, 1985. 3

R. Owens and T. Hewson. Ecmwf forecast user guide. 2018. doi:10.21957/M1CS7H. 61

T. Palmer. The ECMWF ensemble prediction system: Looking back (more than) 25 years and projecting forward 25 years. *Quarterly Journal of the Royal Meteorological Society*, 145(S1):12–24, Sept. 2018. doi:10.1002/qj.3383. 55

T. Palmer, F. Molteni, R. Mureau, R. Buizza, P. Chapelet, and J. Tribbia. Ensemble prediction. (188):43, 07 1992. doi:10.21957/igxccor4n. 55

M. Pasarić and M. Orlić. Long-term meteorological preconditioning of the north adriatic coastal floods. *Continental Shelf Research*, 21(3):263–278, Feb. 2001. doi:10.1016/s0278-4343(00)00078-9. 54

C. A. Paulson and J. J. Simpson. Irradiance measurements in the upper ocean. *J. Physical Oceanography*, 7(6):952–956, Nov. 1977. doi:10.1175/1520-0485(1977)007<0952:imituo>2.0.co;2. 10, 28

R. Pawlowicz, B. Beardsley, and S. Lentz. Classical tidal harmonic analysis including error estimates in MATLAB using T_TIDE. *Comput. Geosci.*, 28(8):929–937, Oct. 2002. doi:10.1016/s0098-3004(02)00013-4. 34

M. Pellizzari, M. Naldi, G. Castaldelli, F. Ghion, E. Manfredini, F. Piccoli, and P. Viaroli. *Flora and vegetation of the Italian transitional water systems*, chapter Salt and brackish lagoons of the southern Po Delta, pages 81–102. CoRiLa, Multigraf, Spinea (Italy), 2009. 87

B. Pérez, R. Brouwer, J. Beckers, D. Paradis, C. Balseiro, K. Lyons, M. Cure, M. G. Sotillo, B. Hackett, M. Verlaan, and E. A. Fanjul. ENSURF: multi-model sea level forecast – implementation and validation results for the IBIROOS and western mediterranean regions. *Ocean Science*, 8(2):211–226, Mar. 2012. doi:10.5194/os-8-211-2012. 56

L. Perini and L. Calabrese. *Il sistema mare-costa dell'Emilia-Romagna*. 2010. 82

L. Perini, L. Calabrese, G. Salerno, P. Ciavola, and C. Armaroli. Evaluation of coastal vulnerability to flooding: comparison of two different methodologies adopted by the

emilia-romagna region (italy). *Nat. Hazards Earth Syst. Sci.*, 16:181–194, July 2015. doi:10.5194/nhessd-3-4315-2015. 80

L. Perini, L. Calabrese, P. Luciani, M. Olivieri, G. Galassi, and G. Spada. Sea-level rise along the emilia-romagna coast (northern italy) in 2100: scenarios and impacts. *Natural Hazards and Earth System Sciences*, 17(12):2271–2287, Dec. 2017. doi:10.5194/nhess-17-2271-2017. 80, 81

L. Perini, L. Calabrese, and P. Luciani. Mareggiate: analisi dati del 2019 e aggiornamento della sintesi 1946-2019, 2019. Bologna: Regione Emilia-Romagna. 57

L. Perini, L. Calabrese, and P. Luciani. Mareggiate e impatti sulla costa: aggiornamento dei dati al 2020, degli indicatori e analisi delle tendenze, 2020. Bologna: Regione Emilia-Romagna. 57, 82, 83, 84

D. Pettenuzzo, W. G. Large, and N. Pinardi. On the corrections of ERA-40 surface flux products consistent with the mediterranean heat and water budgets and the connection between basin surface total heat flux and NAO. *J. Geophys. Res. Oceans*, 115(C6), June 2010. doi:10.1029/2009jc005631. 12, 13, 28

F. Piccoli, N. Merloni, and E. Godini. *Studio integrato sull'ecologia della Sacca di Goro*, chapter Carta della vegetazione della sacca di Goro, pages 173–204. Franco Angeli, Milano (Italy), 1991. 87

N. Pinardi, E. Arneri, A. Crise, R. M., and M. Zavatarelli. *The physical, sedimentary and ecological structure and variability of shelf areas in the Mediterranean Sea*. 2006. the Sea, vol. 14. Harvard University Press, Cambridge, USA, pp. 1243e1330. 3

N. Pinardi, A. Bonazzi, E. Scoccimarro, S. Dobricic, A. Navarra, A. Ghiselli, and P. Veronesi. Very large ensemble ocean forecasting experiment using the grid computing infrastructure. *Bulletin of the American Meteorological Society*, 89(6):799–804, June 2008. doi:10.1175/2008bams2511.1. 55

N. Pinardi, A. Bonazzi, S. Dobricic, R. F. Milliff, C. K. Wikle, and L. M. Berliner. Ocean ensemble forecasting. part II: Mediterranean forecast system response. *Quarterly Journal of the Royal Meteorological Society*, 137(657):879–893, Apr. 2011. doi:10.1002/qj.816. 55

N. Pinardi, L. Cavaleri, G. Coppini, P. D. Mey, C. Fratianni, J. Huthnance, P. F. J. Lermusiaux, A. Navarra, R. Preller, and S. Tibaldi. From weather to ocean predictions: an historical viewpoint. *Journal of Marine Research*, 75(3):103–159, May 2017. doi:10.1357/002224017821836789. 55

P. Pirazzoli. Bora e acqua alta. *Acqua-Aria*, 10:1115–1118, 1981. 82

J. Pistoia, N. Pinardi, P. Oddo, M. Collins, G. Korres, and Y. Drillet. Development of super-ensemble techniques for ocean analyses: the mediterranean sea case. *Natural Hazards and Earth System Sciences*, 16(8):1807–1819, Aug. 2016. doi:10.5194/nhess-16-1807-2016. 55

M. I. Pollak. The sources of the deep water in the eastern mediterranean. *Journal of Marine Research*, 10(2):128–152, 1951. 3

S. Polli. La propagazione delle maree nell'adriatico. In *Atti del 9. convegno dell'associazione geofisica italiana, Rome, 20-21 Novembre*, 1959. 7, 8, 26

P.-M. Poulain and F. Raicich. Forcings. In *Physical oceanography of the Adriatic Sea*, pages 45–65. Springer Netherlands, 2001. doi:10.1007/978-94-015-9819-4_2. 4

L. Prandtl. über ein neues formelsystem für die ausgebildete turbulenz. *Nachr. Akad. Wiss. Göttingen, Mathphys*, 6, 1945. 11

J. Proudman. The effects on the sea of changes in atmospheric pressure. *Geophysical Journal International*, 2:197–209, Oct. 1929. doi:10.1111/j.1365-246x.1929.tb05408.x. 54

F. Raicich. Note on the flow rates of the adriatic rivers. Tech. Rep.RF 02/94 8 pp., CNR Ist. Sperimentale Talassografico, Trieste, 1994. 99, 100, 102

F. Raicich. On the fresh balance of the adriatic sea. *Journal of Marine Systems*, 9(3-4): 305–319, dec 1996. doi:10.1016/s0924-7963(96)00042-5. 1

F. F. Raicich. A case study of the adriatic seiches (december 1997). *Nuovo Cimento della Societa Italiana di Fisica C*, 22(5):715–726, 1999. 54

R. K. Reed. On estimating insolation over the ocean. *Journal of Physical Oceanography*, 7 (3):482–485, May 1977. doi:10.1175/1520-0485(1977)007<0482:oeioto>2.0.co;2. 10

H. Rennau, S. Schimmels, and H. Burchard. On the effect of structure-induced resistance and mixing on inflows into the baltic sea: A numerical model study. *Coastal Engineering*, 60:53–68, Feb. 2012. doi:10.1016/j.coastaleng.2011.08.002. 89, 93

P. M. Rizzoli and A. Bergamasco. The dynamics of the coastal region of the northern adriatic sea. *Journal of Physical Oceanography*, 13(7):1105–1130, jul 1983. doi:10.1175/1520-0485(1983)013<1105:tdotcr>2.0.co;2. 6

W. Rodi. *Turbulence models and their application in hydraulics: A state of the art review.* IAHR monograph, 1980. 88

W. Roether, B. B. Manca, B. Klein, D. Bregant, D. Georgopoulos, V. Beitzel, V. Kovačević, and A. Luchetta. Recent changes in eastern mediterranean deep waters. *Science*, 271 (5247):333–335, Jan. 1996. doi:10.1126/science.271.5247.333. 4

Z. D. Ros, C. Corinaldesi, A. Dell'Anno, C. Gambi, F. Torsani, and R. Danovaro. Restoration of cymodocea nodosa seagrass meadows: efficiency and ecological implications. *Restoration Ecology*, 29(S2), Dec. 2020. doi:10.1111/rec.13313. 87

A. Russo, A. Coluccelli, S. Carniel, A. Benetazzo, A. Valentini, T. Paccagnella, M. Ravaioli, and G. Bortoluzzi. Operational models hierarchy for short term marine predictions: The adriatic sea example. IEEE, June 2013. doi:10.1109/oceans-bergen.2013.6608139. 26

P. M. Ruti, S. Somot, F. Giorgi, C. Dubois, E. Flaounas, A. Obermann, A. Dell'Aquila, G. Pisacane, A. Harzallah, E. Lombardi, B. Ahrens, N. Akhtar, A. Alias, T. Arsouze, R. Aznar, S. Bastin, J. Bartholy, K. Béranger, J. Beuvier, S. Bouffies-Cloché, J. Brauch, W. Cabos, S. Calmanti, J.-C. Calvet, A. Carillo, D. Conte, E. Coppola, V. Djurdjevic, P. Drobinski, A. Elizalde-Arellano, M. Gaertner, P. Galàn, C. Gallardo, S. Gualdi, M. Goncalves, O. Jorba, G. Jordà, B. L'Heveder, C. Lebeaupin-Brossier, L. Li, G. Liguori, P. Lionello, D. Maciàs, P. Nabat, B. Önol, B. Raikovic, K. Ramage, F. Sevault, G. Sannino, M. V. Struglia, A. Sanna, C. Torma, and V. Vervatis. Med-CORDEX initiative for mediterranean climate studies. *Bulletin of the American Meteorological Society*, 97(7): 1187–1208, July 2016. doi:10.1175/bams-d-14-00176.1. 100

A. Salighehdar, Z. Ye, M. Liu, I. Florescu, and A. F. Blumberg. Ensemble-based storm surge forecasting models. *Weather and Forecasting*, 32(5):1921–1936, Oct. 2017. doi:10.1175/waf-d-17-0017.1. 56, 67

C. Schraff, H. Reich, A. Rhodin, A. Schomburg, K. Stephan, A. Periáñez, and R. Potthast. Kilometre-scale ensemble data assimilation for the COSMO model (KENDA). *Quarterly Journal of the Royal Meteorological Society*, 142(696):1453–1472, Mar. 2016. doi:10.1002/qj.2748. 62

M. E. Scully, C. Friedrichs, and J. Brubaker. Control of estuarine stratification and mixing by wind-induced straining of the estuarine density field. *Estuaries*, 28(3):321–326, June 2005. doi:10.1007/bf02693915. 38

J. Sellschopp. Dense low-salinity outflow from the adriatic sea under mild (2001) and strong (1999) winter conditions. *Journal of Geophysical Research*, 108(C9), 2003. doi:10.1029/2002jc001562. 4

A. Sfriso, C. Facca, D. Bon, and A. Buosi. Macrophytes and ecological status assessment in the po delta transitional systems, adriatic sea (italy). application of macrophyte quality index (maqi). *Acta Adriatica*, 57(2):209–216, 2016. 87

A. F. Shchepetkin and J. C. McWilliams. The regional oceanic modeling system (ROMS): a split-explicit, free-surface, topography-following-coordinate oceanic model. *Ocean Modelling*, 9(4):347–404, Jan. 2005. doi:10.1016/j.ocemod.2004.08.002. 59

F. Short, T. Carruthers, W. Dennison, and M. Waycott. Global seagrass distribution and diversity: A bioregional model. *Journal of Experimental Marine Biology and Ecology*, 350 (1-2):3–20, Nov. 2007. doi:10.1016/j.jembe.2007.06.012. 85

U. Simeoni, G. Fontolan, U. Tessari, and C. Corbau. Domains of spit evolution in the goro area, po delta, italy. *Geomorphology*, 86(3-4):332–348, May 2007. doi:10.1016/j.geomorph.2006.09.006. 19

J. H. Simpson, J. Brown, J. Matthews, and G. Allen. Tidal straining, density currents, and stirring in the control of estuarine stratification. *Estuaries*, 13(2):125, June 1990. doi:10.2307/1351581. 39

J. Smagorinsky. General circulation experiment with the primitive equations. *Monthly Weather Review*, 91(3):99–164, Mar. 1963. doi:10.1175/1520-0493(1963)091<0099:gcewtp>2.3.co;2. 9, 25

R. B. Smith. Aerial observations of the yugoslavian bora. *Journal of the Atmospheric Sciences*, 44(2):269–297, jan 1987. doi:10.1175/1520-0469(1987)044<0269:aootyb>2.0.co;2. 6

P. Speer and D. Aubrey. A study of non-linear tidal propagation in shallow inlet/estuarine systems part II: Theory. *Estuarine, Coastal and Shelf Science*, 21(2):207–224, Aug. 1985. doi:10.1016/0272-7714(85)90097-6. 52

J. Staneva, K. Wahle, W. Koch, A. Behrens, L. Fenoglio-Marc, and E. V. Stanev. Coastal flooding: impact of waves on storm surge during extremes – a case study for the german bight. *Natural Hazards and Earth System Sciences*, 16(11):2373–2389, Nov. 2016. doi:10.5194/nhess-16-2373-2016. 66

R. Steinfeldt. Ages and age spectra of eastern mediterranean deep water. *Journal of Marine Systems*, 48(1-4):67–81, July 2004. doi:10.1016/j.jmarsys.2003.03.002. 3

J. Steppeler, G. Doms, U. Schättler, H. W. Bitzer, A. Gassmann, U. Damrath, and G. Gregoric. Meso-gamma scale forecasts using the nonhydrostatic model LM. *Meteorog. Atmos. Phys.*, 82(1-4):75–96, Jan. 2003. doi:10.1007/s00703-001-0592-9. 28, 59, 61, 101

N. Supić, M. Orlić, and D. Degobbis. Istrian coastal countercurrent and its year-to-year variability. *Estuarine, Coastal and Shelf Science*, 51(3):385–397, Sept. 2000. doi:10.1006/ecss.2000.0681. 4

Y. Tanino and H. M. Nepf. Laboratory investigation of mean drag in a random array of rigid, emergent cylinders. *Journal of Hydraulic Engineering*, 134(1):34–41, Jan. 2008. doi:10.1061/(asce)0733-9429(2008)134:1(34). 89

G. I. Taylor. Tidal oscillations in gulfs and rectangular basins. *Proceedings of the London Mathematical Society*, s2-20(1):148–181, 1922. doi:10.1112/plms/s2-20.1.148. 7

K. E. Taylor. Summarizing multiple aspects of model performance in a single diagram. *Journal of Geophysical Research: Atmospheres*, 106(D7):7183–7192, Apr. 2001. doi:10.1029/2000jd900719. 68

P. Teatini, M. Ferronato, G. Gambolati, W. Bertoni, and M. Gonella. A century of land subsidence in ravenna, italy. *Environmental Geology*, 47(6):831–846, Mar. 2005. doi:10.1007/s00254-004-1215-9. 81

R. E. Thomson and W. J. Emery. Chapter 6 - digital filters. In R. E. Thomson and W. J. Emery, editors, *Data Analysis Methods in Physical Oceanography (Third Edition)*, pages 593–637. Elsevier, Boston, third edition edition, 2014. ISBN 978-0-12-387782-6. doi:https://doi.org/10.1016/B978-0-12-387782-6.00006-5. 123, 124

H. L. Tolman. *User manual and system documentation of WAVEWATCH III version 3.14*. 2009. NOAA/NWS/NCEP/MMAB Tech. Note 276, pp 194. 59

L. Tosi, C. D. Lio, T. Strozzi, and P. Teatini. Combining l- and x-band SAR interferometry to assess ground displacements in heterogeneous coastal environments: the po river delta and venice lagoon, italy. *Remote Sensing*, 8(4):308, Apr. 2016. doi:10.3390/rs8040308. 19

Z. Toth and E. Kalnay. Ensemble forecasting at NMC: the generation of perturbations. *Bulletin of the American Meteorological Society*, 74(12):2317–2330, Dec. 1993. doi:10.1175/1520-0477(1993)074<2317:efantg>2.0.co;2. 55

M. N. Tsimplis, R. Proctor, and R. A. Flather. A two-dimensional tidal model for the mediterranean sea. *Journal of Geophysical Research*, 100(C8):16223, 1995. doi:10.1029/95jc01671. 7

M. N. Tsimplis, F. M. Calafat, M. Marcos, G. Jordà, D. Gomis, L. Fenoglio-Marc, M. V. Struglia, S. A. Josey, and D. Chambers. The effect of the NAO on sea level and on mass changes in the mediterranean sea. *Journal of Geophysical Research: Oceans*, 118(2): 944–952, Feb. 2013. doi:10.1002/jgrc.20078. 81

R. Uittenbogaard. Modelling turbulence in vegetated aquatic flows. 2003. International workshop on riparian forest vegetated channels: hydraulic, morphological and ecological aspects, RIPFOR, Trento, Italy. 88

G. Umgiesser, D. M. Canu, A. Cucco, and C. Solidoro. A finite element model for the venice lagoon. development, set up, calibration and validation. *Journal of Marine Systems*, 51 (1-4):123–145, Nov. 2004. doi:10.1016/j.jmarsys.2004.05.009. 8

G. Umgiesser, M. Bajo, C. Ferrarin, A. Cucco, P. Lionello, D. Zanchettin, A. Papa, A. Tosoni, M. Ferla, E. Coraci, S. Morucci, F. Crosato, A. Bonometto, A. Valentini, M. Orlić, I. D. Haigh, J. W. Nielsen, X. Bertin, A. B. Fortunato, B. P. Gómez, E. A. Fanjul, D. Paradis, D. Jourdan, A. Pasquet, B. Mourre, J. Tintoré, and R. J. Nicholls. The prediction of floods

in venice: methods, models and uncertainty (review article). *Natural Hazards and Earth System Sciences*, 21(8):2679–2704, Sept. 2021. doi:10.5194/nhess-21-2679-2021. 56, 82

L. Umlauf and H. Burchard. A generic length-scale equation for geophysical turbulence models. *Journal of Marine Research*, 61(2):235–265, Mar. 2003. doi:10.1357/002224003322005087. 89, 93

L. Ursella, P.-M. Poulain, and R. P. Signell. Surface drifter derived circulation in the northern and middle adriatic sea: Response to wind regime and season. *J. Geophys. Res. Oceans.*, 112(C3), Dec. 2006. doi:10.1029/2005jc003177. 36

A. Valle-Levinson. Definition and classification of estuaries. pages 1–11. Cambridge University Press, 2010. doi:10.1017/cbo9780511676567.002. 36

A. Valle-Levinson, K. Huguenard, L. Ross, J. Branyon, J. MacMahan, and A. Reniers. Tidal and nontidal exchange at a subtropical inlet: destin inlet, northwest florida. *Estuar. Coast. Shelf Sci.*, 155:137–147, Mar. 2015. doi:10.1016/j.ecss.2015.01.020. 36

J. Verduin and J. Backhaus. Dynamics of plant–flow interactions for the seagrass amphibolis antarctica: field observations and model simulations. *Estuarine, Coastal and Shelf Science*, 50(2):185–204, Feb. 2000. doi:10.1006/ecss.1999.0567. 87

R. Vezzoli, P. Mercogliano, S. Pecora, A. Zollo, and C. Cacciamani. Hydrological simulation of po river (north italy) discharge under climate change scenarios using the RCM COSMO-CLM. *Science of The Total Environment*, 521-522:346–358, July 2015. doi:10.1016/j.scitotenv.2015.03.096. 100, 101, 102, 110

I. Vilibić. The role of the fundamental seiche in the adriatic coastal floods. *Continental Shelf Research*, 26(2):206–216, Feb. 2006. doi:10.1016/j.csr.2005.11.001. 8, 54

I. Vilibić and N. Supić. Dense water generation on a shelf: the case of the adriatic sea. *Ocean Dynamics*, 55(5-6):403–415, Nov. 2005. doi:10.1007/s10236-005-0030-5. 3

T. Wahl, I. D. Haigh, R. J. Nicholls, A. Arns, S. Dangendorf, J. Hinkel, and A. B. A. Slangen. Understanding extreme sea levels for broad-scale coastal impact and adaptation analysis. *Nature Communications*, 8(1), July 2017. doi:10.1038/ncomms16075. 62

R. A. Walters and C. Heston. Removing tidal-period variations from time-series data using low-pass digital filters. *Journal of Physical Oceanography*, 12(1):112–115, Jan. 1982. doi:10.1175/1520-0485(1982)012<0112:rtpvft>2.0.co;2. 126

J. C. Warner, B. Armstrong, R. He, and J. B. Zambon. Development of a coupled ocean–atmosphere–wave–sediment transport (COAWST) modeling system. *Ocean Modelling*, 35(3):230–244, Jan. 2010. doi:10.1016/j.ocemod.2010.07.010. 58, 90

M. Waycott, C. M. Duarte, T. J. B. Carruthers, R. J. Orth, W. C. Dennison, S. Olyarnik, A. Calladine, J. W. Fourqurean, K. L. Heck, A. R. Hughes, G. A. Kendrick, W. J. Kenworthy, F. T. Short, and S. L. Williams. Accelerating loss of seagrasses across the globe threatens coastal ecosystems. *Proceedings of the National Academy of Sciences*, 106(30): 12377–12381, July 2009. doi:10.1073/pnas.0905620106. 85

J. Zaldivar, E. Cattaneo, M. Plus, C. Murray, G. Giordani, and P. Viaroli. Long-term simulation of main biogeochemical events in a coastal lagoon: Sacca di goro (northern adriatic coast, italy). *Continental Shelf Research*, 23(17-19):1847–1875, Nov. 2003. doi:10.1016/j.csr.2003.01.001. 20

M. Zavatarelli. Diagnostic and prognostic model studies of the adriatic sea general circulation: seasonal variability. *Journal of Geophysical Research*, 107(C1), 2002. doi:10.1029/2000jc000210. 4

M. Zavatarelli and N. Pinardi. The adriatic sea modelling system: a nested approach. *Annales Geophysicae*, 21(1):345–364, Jan. 2003. doi:10.5194/angeo-21-345-2003. 4, 6

Y. J. Zhang, N. Gerdts, E. Ateljevich, and K. Nam. Simulating vegetation effects on flows in 3d using an unstructured grid model: model development and validation. *Ocean Dynamics*, 70(2):213–230, Dec. 2019. doi:10.1007/s10236-019-01333-8. 88, 89, 91

Acknowledgements

Among the many people that accompanied me in my work, I am most grateful to my supervisor, Dr. Andrea Valentini. His advise has been precious and guided me through the many difficulties and satisfactions encountered along the way, sharing ideas, projects and also pleasant conversations. My permanence in Arpae was delighted by the fine colleagues I found there. I am really thankful to Lidia and Silvia with whom I shared successful discussion. They show and explained me many things about the Arpae modelling infrastructures and we shared good moments.
I am deeply thankful to Prof. Nadia Pinardi for her fundamental supervision and foresight that encouraged me in these years and helped me to add great value to my work.
I want to genuinely thank the colleagues from University of Bologna, Francesco and Umesh, that shared with me time, papers and enjoyable moments. I am very grateful to all the colleagues I met at SINCEM lab in Ravenna, where we shared working discussion and pleasant moment as well. Especially I want to thank Veronica, Leonardo and Ozlem for the time spent together.
Along the path I had the chance to work with many people from the OPA division of CMCC in Lecce, and we had great time together, both from the working and personal point of view. Among them I want to personally thank Ivan, Ivano and Giorgia that sustained and helped me in many ways during my work.
My sincere gratitude goes to Prof. Hans Burchard for the profitable scientific discussion and for the good time that i spent in Warnemünde at the IOW. I am also very grateful to all IOW PhD students I met there that shared with me very nice moments.
Voglio ringraziare tutta la mia famiglia che mi ha costantemente supportato in questi anni. Un saluto speciale al mio nonno Aride che sarebbe stato felice di vedermi rag-

giungere questo traguardo.

My last acknowledgement is dedicated to the daughter of Zeus and Mnemosyne to which i am most grateful, Euterpe, the Muse of music and poetry. Music is part of my life and always sustained me in good and bad situations. As long as I could play some good music and share it with good friends, there will be nothing impossible to deal with.